REPETITIVELY Q-SWITCHED Nd:BeL LASERS

Prepared for

Goddard Space Flight Center
Greenbelt Road
Greenbelt, Maryland 20771

THE AEROSPACE CORPORATION

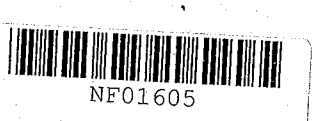

Final Report
1 February 1979 - 30 April 1979

REPETITIVELY Q-SWITCHED Nd:BeL LASERS

Prepared for

Goddard Space Flight Center
Greenbelt Road
Greenbelt, Maryland 20771

NASA Project Officer: Dr. J. Degnan

May 2, 1979

Prepared by

THE AEROSPACE CORPORATION

Electronics Research Laboratory
The Ivan A. Getting Laboratories
P.O. Box 92957
Los Angeles, California 90009

Contract Number NAS 5-25098
Sponsored by National Aeronautics and Space Administration

Contributors to this report:

Dr. M. Birnbaum, Principal Investigator
The Aerospace Corporation
P.O. Box 92957
Los Angeles, California 90009

Dr. L. G. DeShazer, Principal Investigator
University of Southern California
Los Angeles, California 90009

Research Performed at Aerospace Corporation:

Dr. M. Birnbaum, A. W. Tucker (Members of the Technical Staff)
C. L. Fincher (Assistant to the Technical Staff)

Research Performed at University of Southern California by:

L. G. DeShazer, Senior Staff Scientist
Hughes Research Labs., Malibu, Calif.
K. Wilson, Research Assistant
Carolyn Sauer, Research Assistant

TABLE OF CONTENTS

LIST OF FIGURES

LIST OF TABLES

I. PROJECT DESCRIPTION

The goals of this contract effort are to determine the thermal and mechanical characteristics of Nd:BeL which will ultimately limit its performance at high average power levels.

In the prior effort, we demonstrated that X-axis Nd:BeL could deliver output pulses almost a factor of three greater than that of Nd:YAG. The experimental arrangement used in each case was almost the same and the rods were of identical size: 5 x 50 mm. This is consistent with the lower stimulated emission cross section which was determined for Nd:BeL.

The output beam characteristics (pulse width, peak power, beam dimensions and collimation) will be determined at high repetition rates for both Nd:BeL and Nd:YAG. This will show directly the potential advantage of Nd:BeL at high average power levels. In addition, the fundamental thermal and mechanical constants of the material relevant to high average power will be measured.

II. REPETITIVE Q-SWITCHED LASER PERFORMANCE*

A. Q-Switched Laser Description

A block diagram of the repetitive Q-switched laser which was used to obtain comparative performance of the different laser rods under repetitive Q-switched operation is shown in Fig. II-1. This is the same laser used in the previous contract effort.[1] Since a variety of tests, using different flashlamps and pulse forming networks, were performed in the previous effort, the laser configuration used in the present study is summarized below.

The cavity which encloses the laser rod consists of the familiar single elliptical reflecting enclosure with the lamp and rod at the respective foci.

The pump cavity, including the end plates, was polished to a mirror finish and gold plated. The dimensions of the cavity are:

*by M. Birnbaum, A. Tucker, C. Fincher

Repetitively Q-Switched Laser

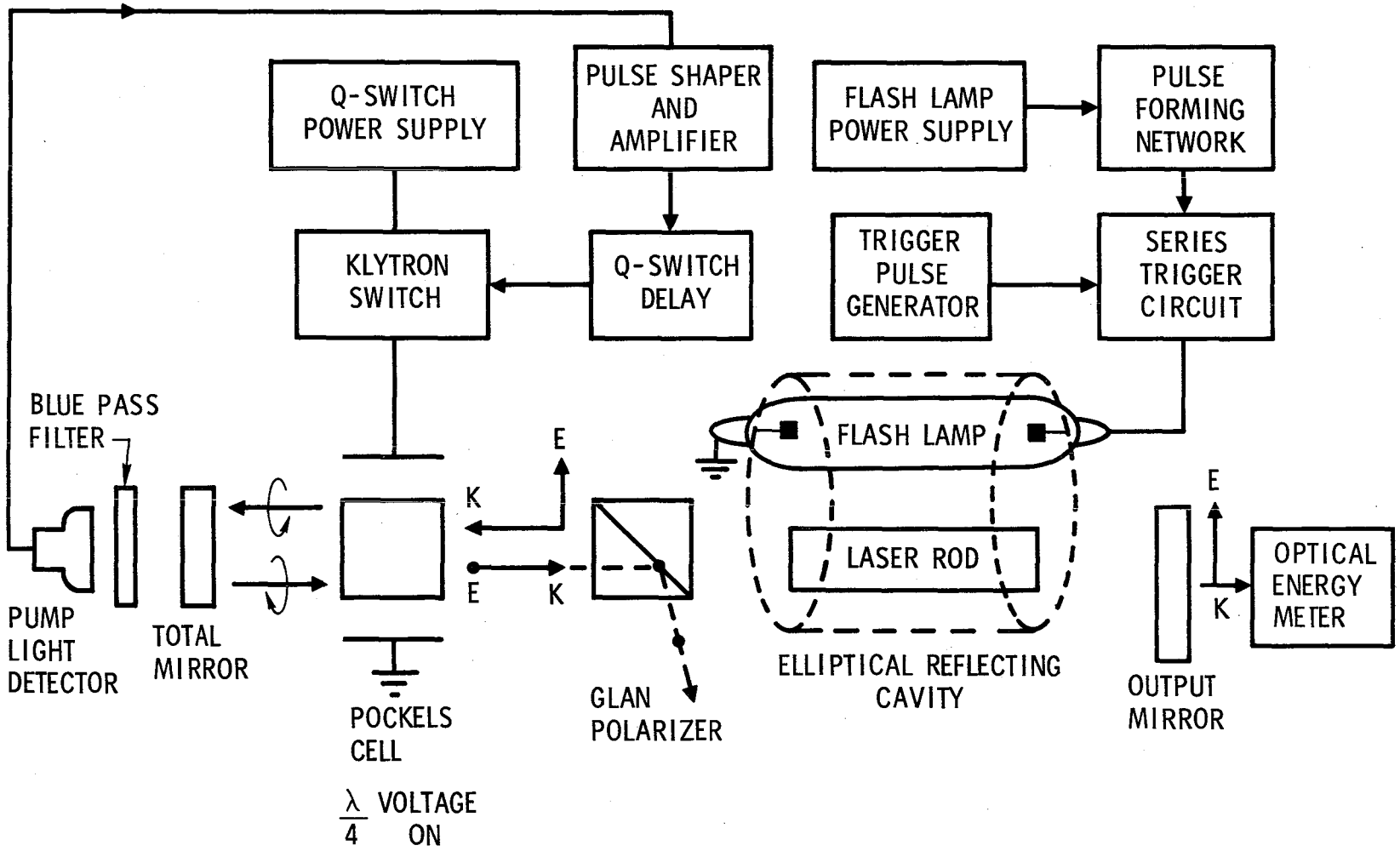

II-1 Block Diagram of Repetitively Q-Switched Laser

Minor axis	39.0 mm
Major axis	43.6 mm
Foci separation	19.0 mm
Length	45.2 mm

The actual length of rod which is pumped is 41.1 mm although the rods are 50 mm long. Allowance for the O-ring seals in the rod holders for water cooling has necessitated this reduction in the effective length of the rod. The laser will operate at 10 PPS and consequently water cooling is required. Water cooling jackets are provided for the cavity, the rod, and the flashlamp.

The flashlamp is an ILC-6F2G lamp which has a 6 mm bore diameter and a 50 mm discharge length. The lamp is filled with Xenon to a pressure of 450 torr. The lamp envelope was made of UV absorbing quartz with an UV cutoff of 240 nm. Relevant lamp characteristics are: lamp impedance parameter, 11 ohm amp$^{\frac{1}{2}}$; maximum peak current, 1100 amps; a single shot explosion energy constant of 7.5×10^4 watt-sec$^{\frac{1}{2}}$; and a maximum average power of 1900 watts.

Pulse circuit parameters for the lamp giving pulse shape and energy coupling to the lamp was calculated using the theory of Markiewicz and Emmett.[2] The pulse forming network, shown in figure II-2, consisted of two stages of 50 μF capacitance and 20 μH inductance connected in parallel. This network was designed to provide a critically damped pulse (damping factor ~0.8) of 190 μsec duration (full width to 10% points) when 28 joules was delivered to a lamp having an impedance parameter of 16.3 Ω-amp$^{\frac{1}{2}}$. For the ILC 6F2G lamp used in the present laser, however, the calculated damping factor is ~0.5 with a 28 joule input providing a theoretically slightly under damped pulse. The actual pulse shape with a 60 joule input for Nd:BeL and a 40 joule input for Nd:YAG is shown in Figure II-6. The full width to the 10% points is 240 μsec and the full width at half maximum amplitude (FWHM) is 150 μsec. Using this pulse forming network a maximum of 50 joules can be applied to this lamp without exceeding the maximum peak current.

Since a wide range of capacitor charging voltages will be encountered and absolute triggering reliability must be achieved at low charging voltages, series triggering was selected. The secondary of the trigger transformer is

Flash lamp Trigger and Discharge Circuit

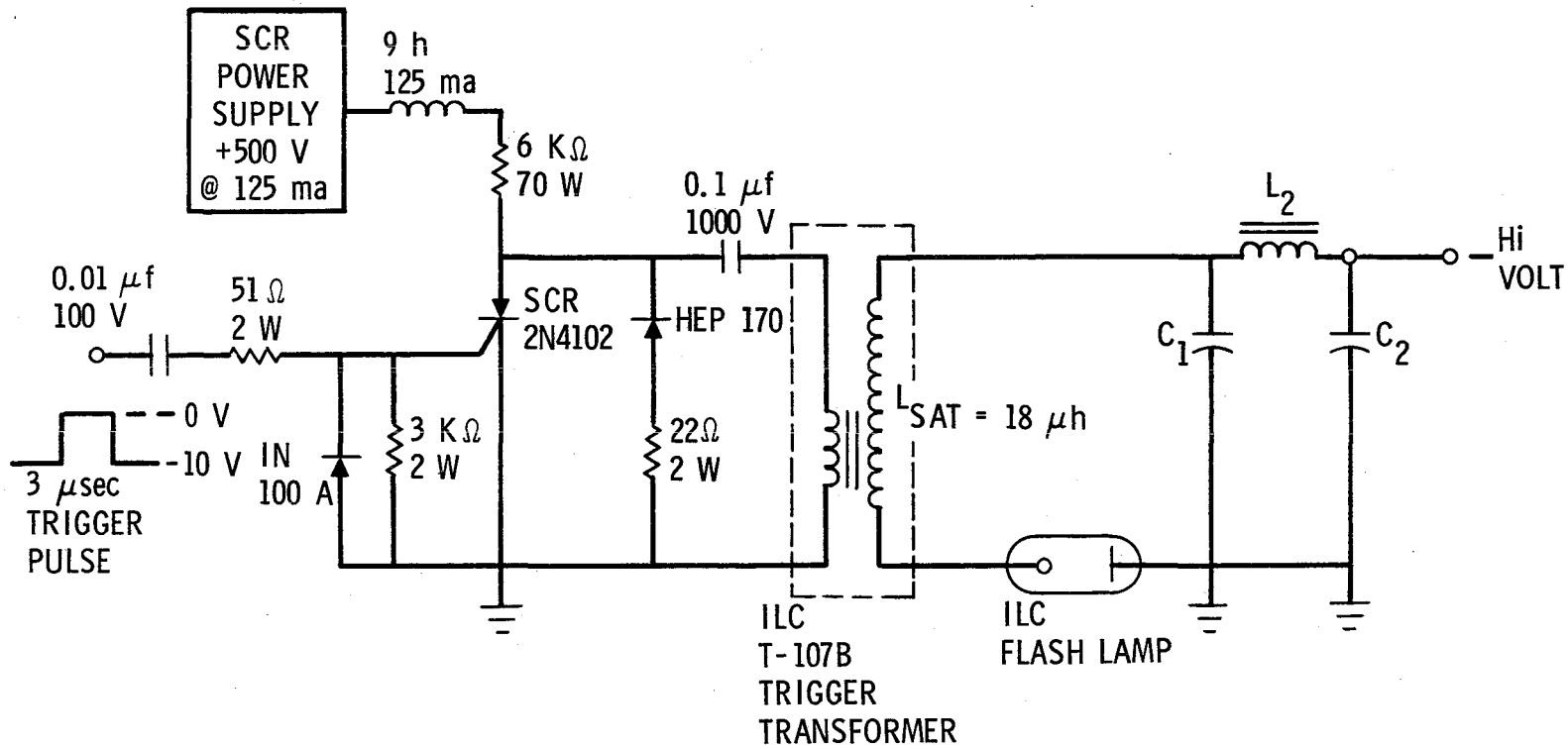

II-2 Circuit Diagram of Trigger and Discharge Circuit

in series with the energy storage capacitor and its saturated secondary inductance (19 μH) serves as one of the pulse forming inductors. A ILC T-107B trigger transformer was utilized which provides a 15 KV, 2 μsec ionization pulse.

Q-switching is accomplished with a Pockels cell and a Glan calcite Polarizer. The Pockels cell is a Lasermetrics EOM 812FV-106 with a 10 mm aperture and can withstand an optical peak power density of 300 MW/cm^2. The Pockels cell has a capacitance of 8 pf and a risetime of less than 1 nsec. The crystal material is KD*P mounted in a cell containing an index matching fluid which reduces the reflectance of each internal optical surface to approximately 0.5%. High efficiency "V" type AR coatings at 1064 nm are applied to the external surfaces of the windows. These coatings can withstand a power density of 1 gigawatt/cm^2. The quarter-wave voltage required at 1064 nm is 4.5 KV.

The polarizer is a Lasermetrics Q-switch type Glan air spaced prism with side exit windows. "V" type AR coatings at 1064 nm are applied on entrance and exit windows. Maximum power density is 150 Mw/cm^2. It has a 10 x 10 mm aperture and a contrast ratio of greater than 3000:1 at 633 nm.

The total mirror, M1, is 99.7% reflecting at 1064 nm. This reflector had a durable, dielectric, low absorbing coating designed to withstand power densities up to 500 MW/cm^2 in a 55 nanosec pulse and meet all requirements of MIL-C675A. The coating is applied to a BK-7 substrate which is 25.4 mm in diameter and 9.5 mm thick. The substrate is flat to $\lambda/10$ with a 30 arc-minute wedge. This mirror was AR coated for 0.25% reflectivity at 1060 nm on the back surface. The mirror was purchased from the Perkin-Elmer Corporation. The output reflector was a double stacked resonant reflector assembled at The Aerospace Corporation and had 40% reflectivity at 1064 nm.

A block diagram of the Q-switch laser resonator showing the location of the optical components is shown in Figure II-3. The 41 cm long cavity was necessary due to the length of the flashlamp and proximity of the flashlamp to the laser rod. Mounting of components also prevented shortening of the laser cavity.

Q-Switch Laser Resonator

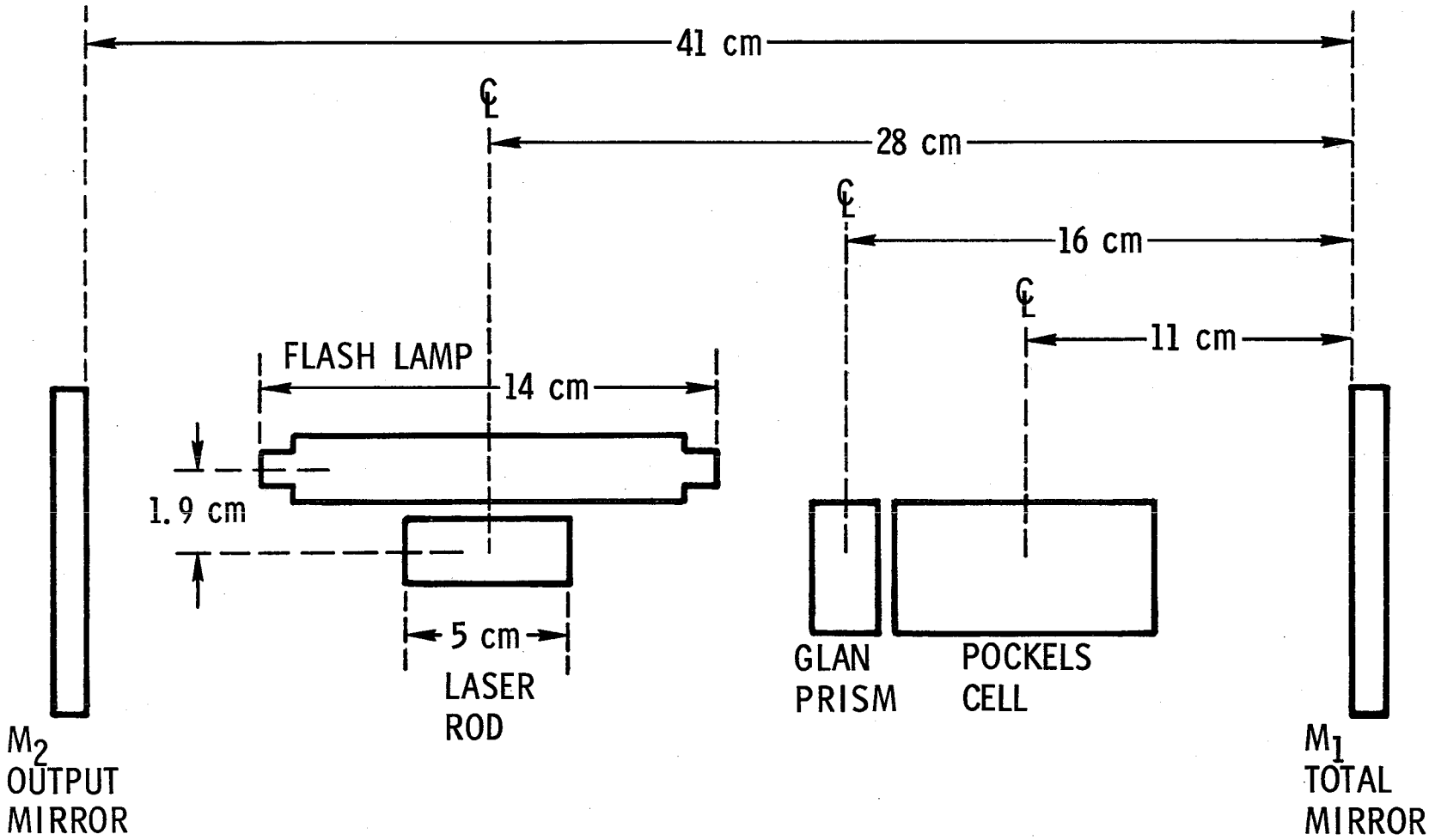

II-3 Block Diagram of Q-Switched Laser Resonator

The laser is operated in the quarterwave mode in which 4.5 KV is applied to the Pockels cell when the flashlamp pump source is fired (Figure II-4). Under these conditions, the linearly polarized radiation (provided by the Glan polarizer in the case of Nd:YAG) passes through the Pockels cell and becomes circularly polarized. After being reflected from the laser mirror, the radiation again passes through the Pockels cell and undergoes another $\lambda/4$ retardation, becoming linearly polarized but at 90^{o} to its original direction. The radiation is then deflected out of the laser cavity by the polarizer, preventing optical feedback in the cavity and subsequent laser emission. Near the end of the flashlamp pulse, the voltage is switched off the Pockels cell by a Lasermetrics switch, model GS-8, which has a rise time of less than 5 nanosecs, permitting the modulator to pass the beam without retardation. Oscillations within the cavity buildup and the "Q-switched" pulse is emitted through the output mirror. In the case of Nd:BeL, which is optically aniosotropic and will produce a laser output which is completely plane polarized, the Glan polarizer may not be necessary.

The Q-switch is delayed from the start of the flashlamp pulse in the following manner (Figure II-1). When the trigger pulse generator fires the flashlamp, the pump light detector (PIN 10D-diode) monitors the flashlamp light through the total 1060 nm mirror which passes some of the visible fluorescence. The blue pass filter is used to reject the 1060 nm laser light and prevent damage to the detector. (The signal from the detector is connected to the pulse shaping and amplifier circuit which amplifies and sharpens the leading edge of the flashlamp pulse.) The leading edge of the flashlamp pulse is then used to drive a delay generator which produces a trigger pulse for the Klytron switch. The Q-switch delay pulse from the delay generator may be delayed from the start of the flashlamp at any desired time.

B. Crystals Samples

A brief description of the Nd:BeL and Nd:YAG rods used in the Q-switch test arrangement is given below.

The Nd:BeL rod was purchased from Allied Chemical Corporation

Element Orientation for Q Switching

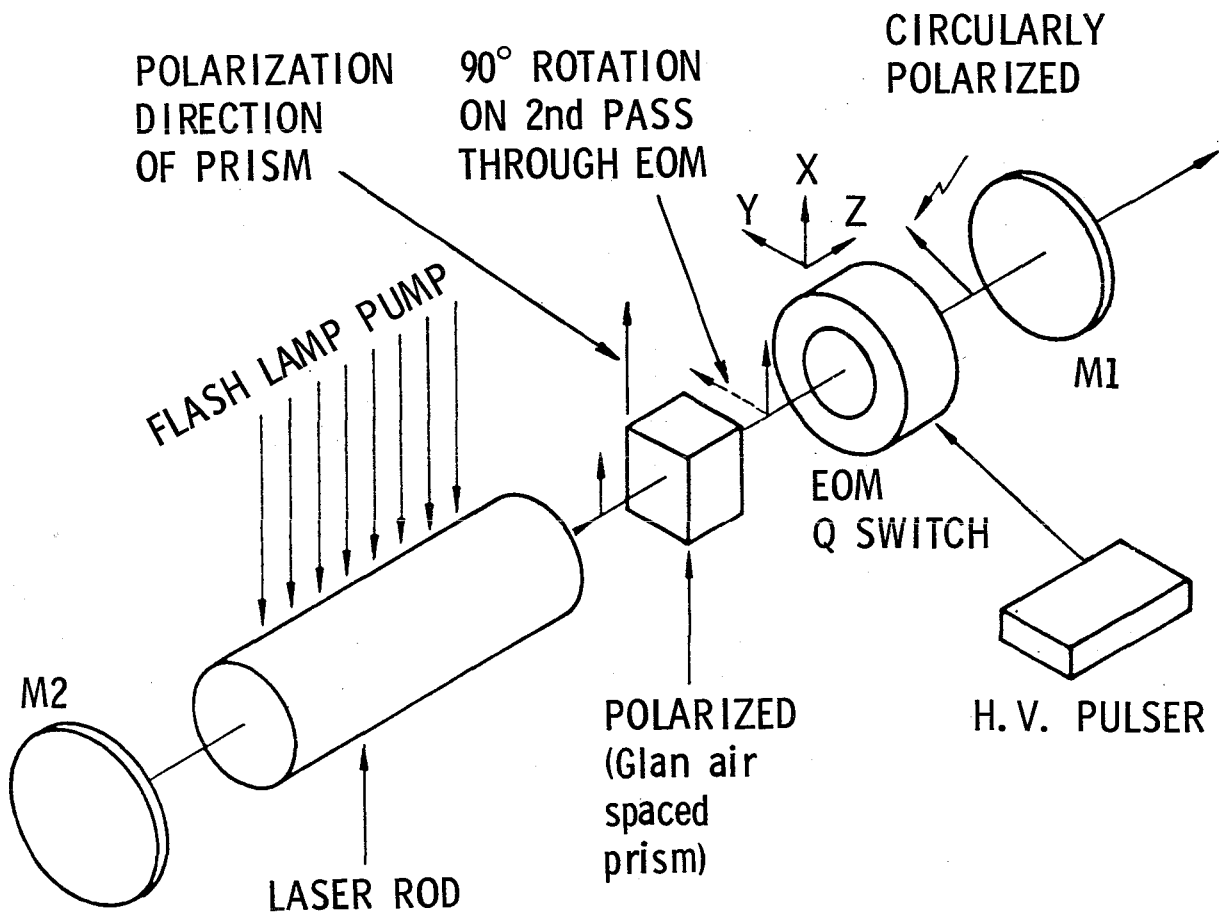

FIG. II-4 Diagram of Optical Arrangement for Q-Switching

(at present the only known supplier of this material). An x-axis rod (5 x 50 mm) having a 1.2% $\pm$ 0.15% (atomic percent) Neodymium concentration was obtained. End surfaces were polished flat to 1/10 wavelength, parallel to within 5 arc seconds, perpendicular to rod axis to within 2 arc minutes, have 0-0 finish and are anti-reflection coated for 1070 nm.

The Nd:YAG rod (5 x 50 mm) was purchased from Union Carbide Corporation (Linde Division) and has the following specifications. The rod has a 1% (atomic percent) Neodymium concentration. End surfaces are polished flat to 1/10 wavelength, parallel to within 10 arc seconds, with 0-0 surface finish, perpendicular to the rod axis to within 5 arc minutes, and are anti-reflection coated at 1060 nm. Both rods have fine ground barrel finish.

C. Experimental Arrangement

The experimental arrangement for measuring the output beam characteristics (pulse energy, peak power, pulse width, beam divergence and mode patterns) is shown in Figure II-5.

The output pulse energy is monitored with a Laser Precision Corporation, model RK3230, pyroelectric radiometer. The radiometer head is connected to an energy readout which contains a pulse averager which averages the energy of 1, 10 or 100 pulses which can be selected as desired. A 100 point average was selected for our experiments. Simultaneously, the peak power, pulse width and pulse shape is monitored with a ITT F4018 bi-planar photodiode which has an S-1 surface and a 0.5 nanosec risetime. This photodiode was calibrated against the pyroelectric radiometer. The output of the photodiode is connected to the 50 ohm input of a 7A19 preamplifier and displayed on the lower trace of a Textronix 7844 dual beam 400 MHz oscilloscope. This preamplifier has a rise time of less than 1 nanosec.

In order to observe the Q-switch time and long pulse threshold relative to the flashlamp pulse, the flashlamp light was monitored with a PIN-10 D diode through the total mirror M1 and displayed on the upper trace of the oscilloscope.

Experimental Arrangement

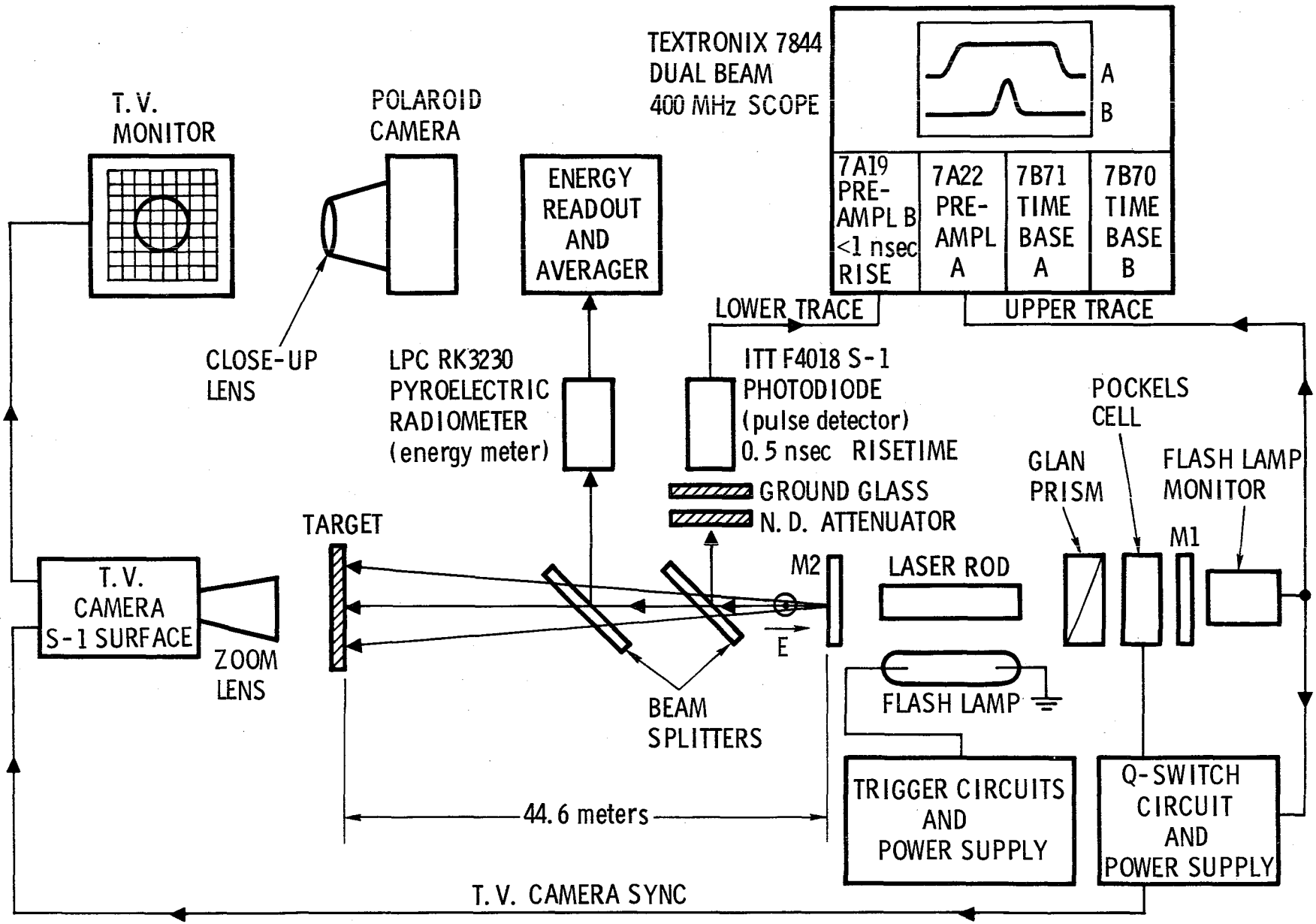

II-5 Experimental Arrangement for Measuring Pulse Energy, Pulse Width, Peak Power, and Beam Divergence

In Figure II-6, the upper left photo shows the Nd:BeL long pulse output and threshold (lower trace) relative to the flashlamp output (upper trace). The upper right photo shows the Nd:BeL Q-switch pulse (lower trace) and the time at which the Q-switch occurs relative to the start of the flashlamp pulse (upper trace). The lower photo provides this same information for Nd:YAG.

In order to measure the beam divergence we had first considered using a focusing element (lens) in a typical experimental arrangement. Day and Stubenrauch [3] at the National Bureau of Standards point out that several types of error sources may be encountered when using this technique. These are (1) use of the Fresnel approximation in the derivation of the focal plane/far-field equivalence, (2) spherical aberration of the lens, (3) establishing an accurate focal length, and (4) location of the observation plane. Perhaps the largest quantitative errors result from an improper determination of the focal length and errors in the location of the observation plane. For a 1% misplacement in the location of the observation plane, an increase in the error in beam divergence by a factor of 5 can occur. Day and Stubenrauch also point out that (quoted from Ref. 3) "many lasers do not emit in a single transverse mode but rather in a combination of modes often distorted by non-uniform thermal effects. It is for this class of lasers that the specification of beam characteristics by a single parameter becomes difficult if not inappropriate and also for which transformation procedures are most important.

Two principal problems arise with this form of measurement.

1. The output of a Q-switched solid-state laser is often grossly asymmetric. It is frequently elliptical and may have multiple maxima, well displaced from the centroid.
2. Both the propagation direction (of, say, the centroid) and/or the profile may vary from pulse to pulse.

If problem 1 is severe, any form of envelope measurements may yield little information of use to the designer, the manufacturer, or the user. In this case it is probable that one should proceed to use a means of obtaining

Output Pulses from Nd:BeL and Nd:YAG Q-Switch Laser

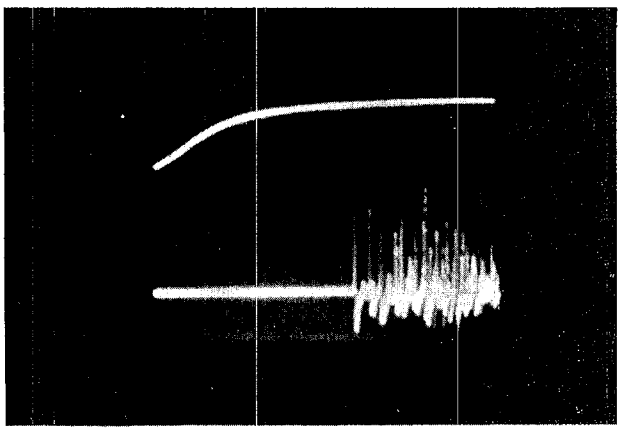

Nd:BeL

LOWER TRACE: LONG PULSE OUTPUT, 10 μsec / DIV
UPPER TRACE: FLASHLAMP PULSE, 10 μsec / DIV

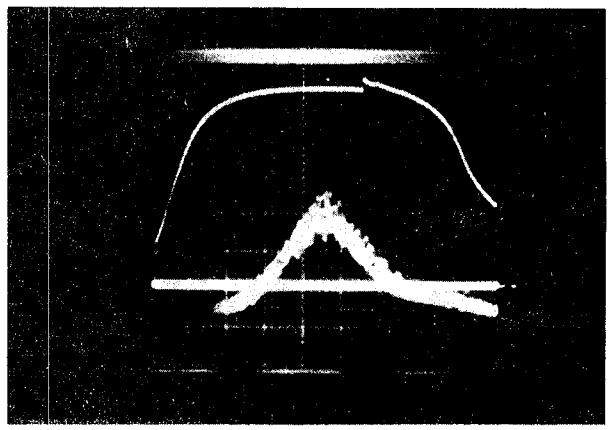

Nd:BeL

LOWER TRACE: Q-SWITCH OUTPUT, 10 nanosec / DIV
UPPER TRACE: FLASHLAMP OUTPUT, 20 μsec / DIV

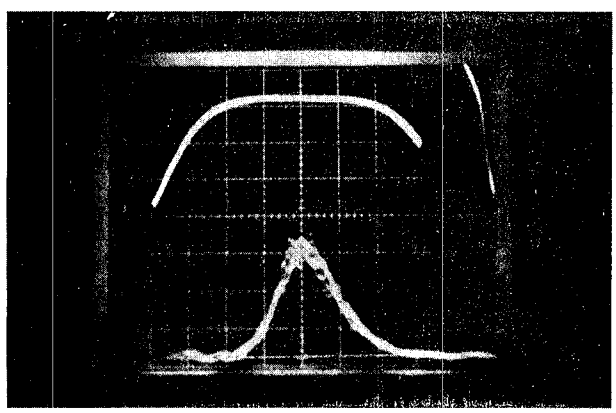

Nd:YAG

LOWER TRACE: Q-SWITCH OUTPUT, 5 nanosec / DIV
UPPER TRACE: FLASHLAMP OUTPUT, 20 μsec / DIV

II-6 Output Pulses from Nd:BeL and Nd:YAG Q-Switch Laser

spatially resolved measurements.

If problem 2 is severe, a relatively crude solution is to define an average divergence

$$\theta_{1/2,\ ave}(f)$$

where the conditions of the average (e.g., first 10 pulses, 50th to 100th pulses, etc.) should be clearly specified, (f = focal length).

A greatly superior solution to both problems 1 and 2 is to replace the focal plane aperture with an imaging device such as a videcon, CCD, or detector array, possibly with some additional optics for magnification. This has the advantage of providing information on both complex beam profiles and beam wander."

We chose to observe the beam profile in the far-field by means of a closed circuit television system and specify the beam divergence of Nd:BeL relative to Nd:YAG rather than specify absolute values. The transition between the near field region and far field region is generally taken to be $d = D^2/\lambda$ where D is the near field beam diameter over which the amplitude is non-zero, λ is the laser wavelength and d is distance of the observation plane from the source. At this distance, d, the maximum on axis phase error from neglecting the near field contribution is $\lambda/8$. For our laser, D = 5mm and λ = 1064 nm so that d = 23.5 meters.

In our measurements, the observation plane was located 44.6 meters from the laser (see Figure II-5). The target consisted of a sheet of manila paper on which a grid with a 1 mm resolution was affixed. The area of the manila card which was illuminated by the beam was clearly visible on the back side of the card. The spot was then observed by means of a television camera with a zoom lens located behind the card. The zoom lens was necessary to provide magnification for adequate resolution. The T.V. camera was an RCA model TC-1005/501 with an RCA 4532 silicon vidicon which is sensitive to 1064 nm radiation. The vertical sweep of the T. V. camera was synchronized to the laser frequency so that the T.V. camera would start its

sweep at the instant the beam arrived on target. Since the Q-switch pulse is only 10 nanosecs long but the vertical sweep takes about 17 millisecs, the laser is off by the time the T. V. camera completes its sweep. However, since the fluorescence decay time of the vidicon is much greater than 17 millisecs, the intensity distribution can be retrieved. The output of the T. V. camera was connected to a Setchell Carlson 10-inch monitor (model 10 M 915) on which the beam profile can be displayed and photographed with a polaroid camera.

D. Q-Switch Operation of Nd:BeL and Nd:YAG

1. Nd:YAG

The first tests were performed with the Nd:YAG rod installed. In long pulse operation (non-Q-switched) at 1 PPS, 70 mJ was obtained with an electrical energy input of 41 joules. At this input, long pulse threshold was 49 μsec. This threshold corresponds to 17% of the total electrical energy input to the lamp which means that long pulse threshold is approximately 7 joules.

In Q-switch operation, the optimum Q-switch time was found to be 151 μsec. This means that at the time the Q-switch pulse occurs, 81% of the total light energy emitted by the lamp pumps the Nd:YAG rod.

The Q-switch output energy of the Nd:YAG rod as a function of input energy up to Q-switch time was measured for several repetition rates between 1 pulse/15 secs and 10 pulses per sec (10 PPS). This data is plotted in Figure II-7. Prelasing occurred at about 31 joule input. We noted a slight decrease in output energy with increasing repetition rate. The Q-switch pulse width as a function of input energy (up to Q-switch time) at different repetition rates is plotted in Figure II-8. As expected the pulse width narrows with increasing energy input. However, we noted about a 4 nanosec $\pm$ 2 nsec increase in pulse width as the pulse repetition rate was increased from 1 pulse/15 sec to 10 PPS. This is shown in Figure II-9 for Nd:YAG at a 35 joule input up to Q-switch time (43 joules total electrical energy into the lamp).

Input/Output Curves vs Pulse Repetition Rate

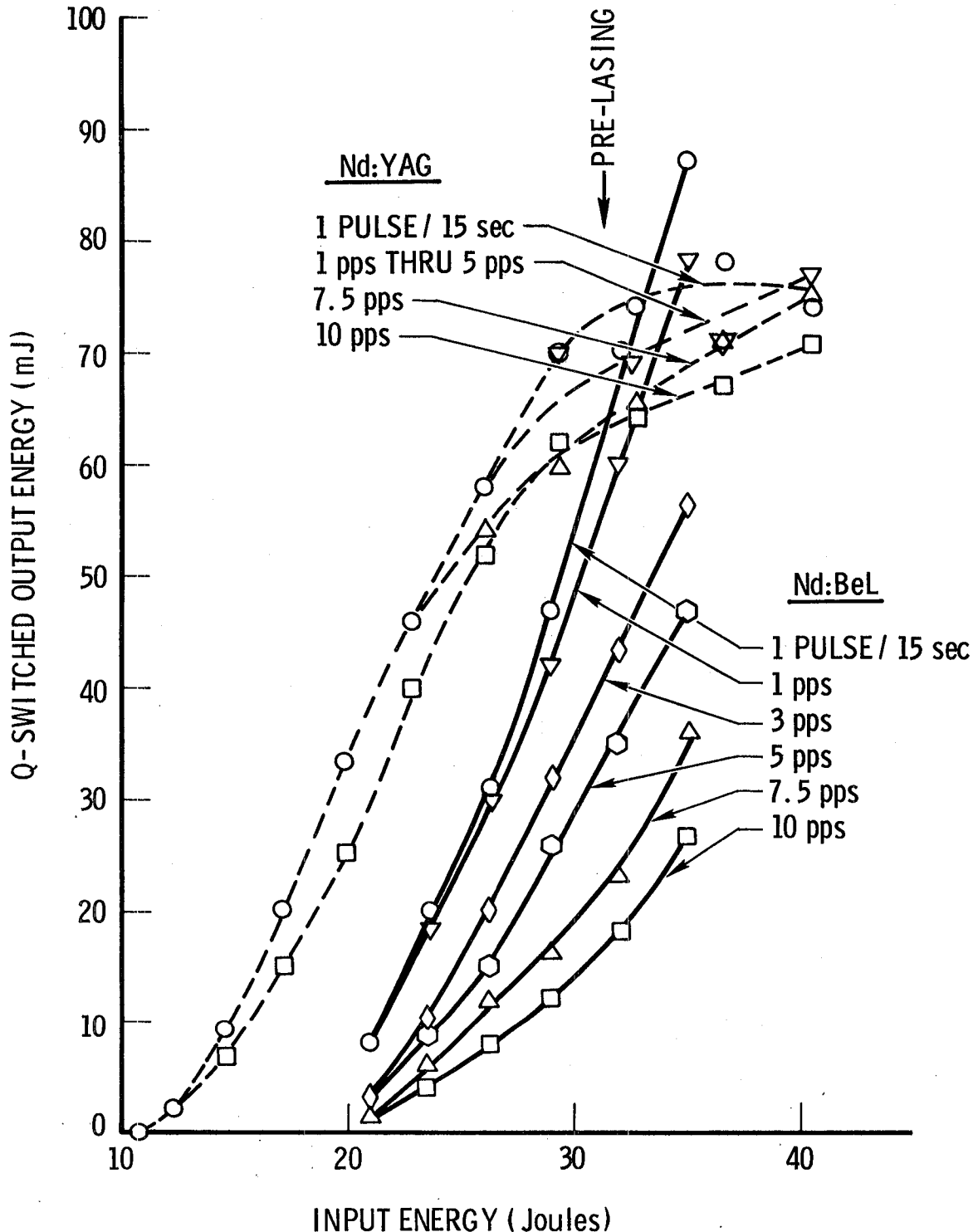

II-7 Q-Switch Energy Output Vs. Energy Input Up to Q-Switch Time as a Function of Pulse Repetition Rate for Nd:YAG and Nd:BeL

Q-Switch Pulse Width/Input Energy Curves
vs
Pulse Repetition Rate

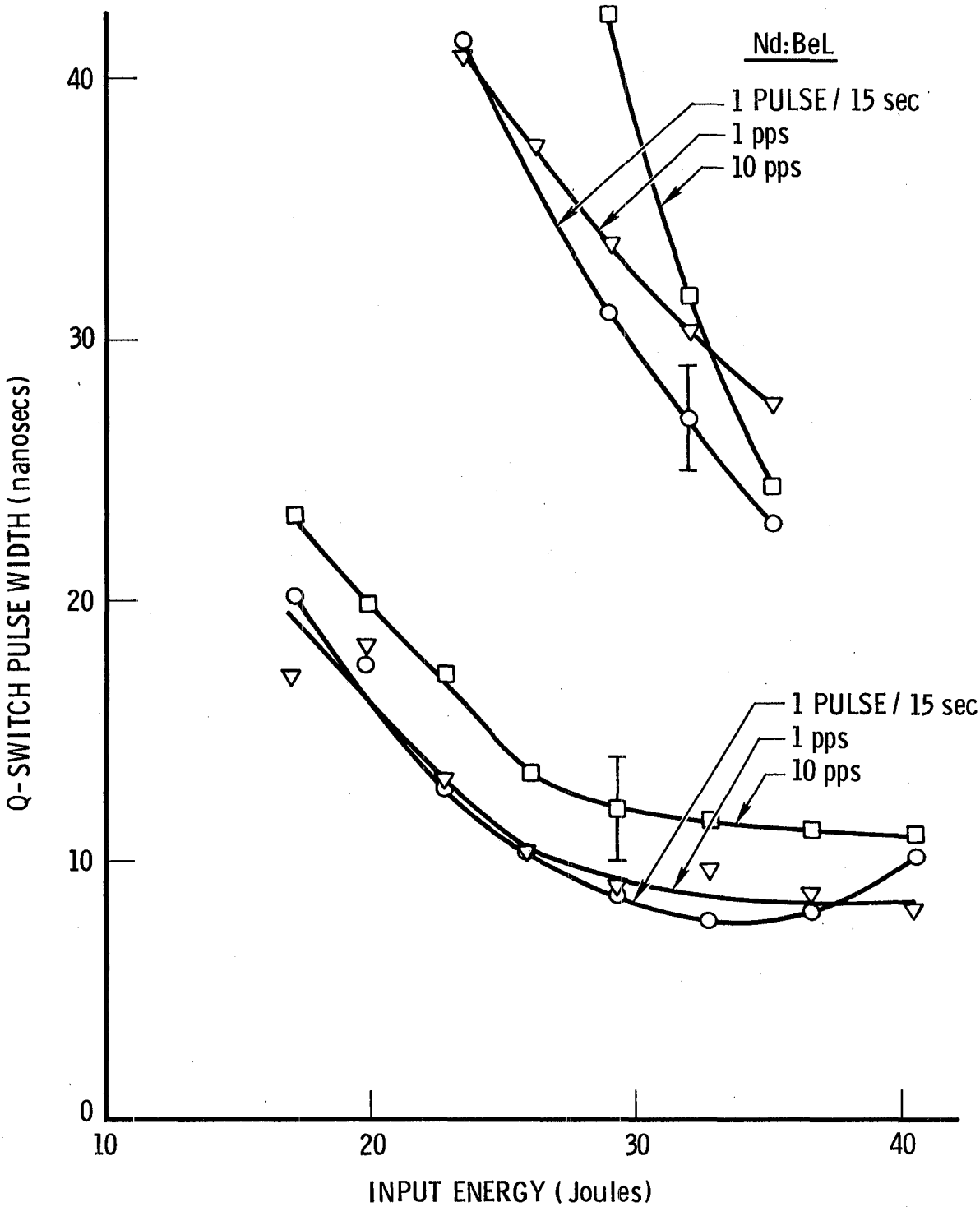

II-8 Q-Switch Pulse Width Vs. Energy Input Up to Q-Switch Time as a Function of Pulse Repetition Rate for Nd:YAG and Nd:BeL

Q-Switch Pulse Width
vs
Pulse Repetition Rate
EIN=35 Joules (up to Q-Switch Time)

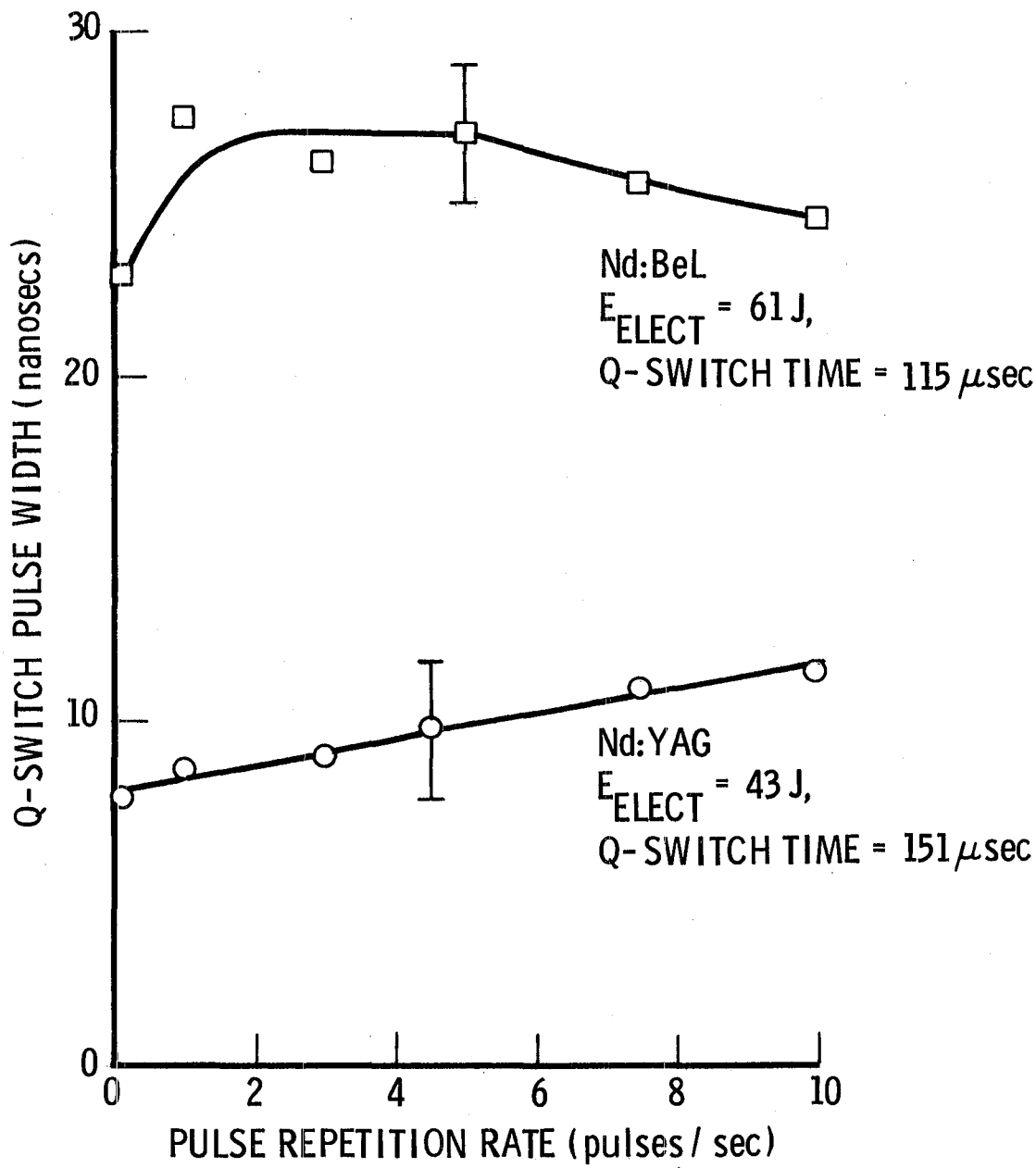

II-9 Q-Switch Pulse Width Vs. Pulse Repetition Rate at 35 Joule Input Up to Q-Switch Time for Nd:YAG and Nd:BeL

Using the technique described previously, beam profile measurements on Nd:YAG were performed. At an energy input (up to Q-switch time) of 31 joules (38 joules total electrical energy input) and at a distance of 44.6 meters from the laser, the far field spot size as a function of repetition rate (1 PPS to 10 PPS) was photographed. This data is shown in Figure II-10. At 1 PPS the spot size at 44.6 meters was 7.5 cm in diameter giving a full width beam divergence of 1.6 milliradians. The meaning of this is as follows. Because of the photographic method used to record the spot size, $1/e^2$ intensity points cannot be determined. The spot size is taken to be the full diameter of the image on the photograph. At each repetition rate the same number of shots (5 shots) was recorded. The "beam divergence" as a function of repetition rate for Nd:YAG is plotted in Figure II-13. We see that for a 31 joule input (up to Q-switch time) the beam divergence increases only slightly from 1.6 mrad at 1 PPS to 2 mrad at 10 PPS.

2. Nd:BeL (X-Axis)

After completion of the above tests, the Nd:BeL rod was installed in the cavity.

During the prior contract effort[1] we discovered 2 regions of bulk damage in the interior of another Nd:BeL rod directly under the O-ring seals which held the rod in its water cooling jacket. It was speculated that this damage was caused by stress in the rod due to exposure at the higher input energies (100 joules). These tests were performed at a repetition rate of 1 PPS. To avoid damage that might occur at 10 PPS with 100 joule input, the first tests (described below) were performed only up to a 60 joule electrical energy input to the lamp.

Prior to installation of the Nd:BeL rod in the Q-switch laser cavity, the rod was made to lase CW by end pumping with the 5145 Å output of an argon ion laser[1] in order to establish the direction of the 1079 nm output polarization and hence the Y-axis of the rod. When the X-axis Nd:BeL rod was installed in the Q-switch laser cavity, care was taken to align the Y-axis of the rod with

Nd:YAG

FAR FIELD SPOT SIZE vs REPETITION RATE

DISTANCE = 44.6 meters,

ENERGY INPUT = 31 Joules

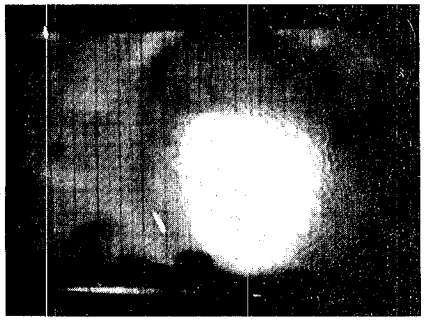

1 pps
E_{OUT} = 70 mJ

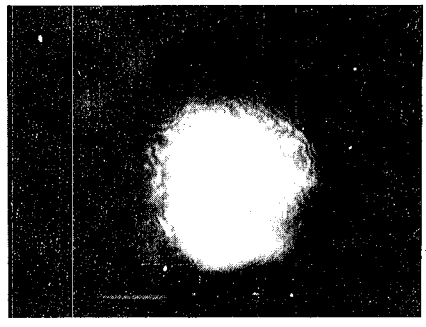

5 pps
E_{OUT} = 68 mJ

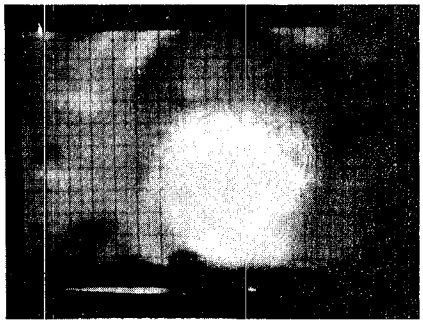

3 pps
E_{OUT} = 69 mJ

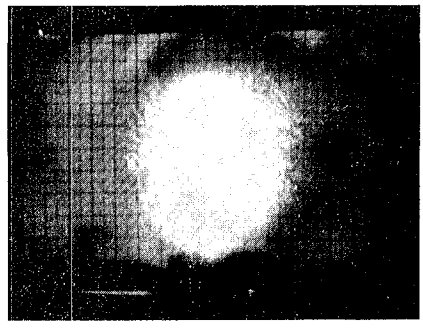

7.5 pps
E_{OUT} = 65 mJ

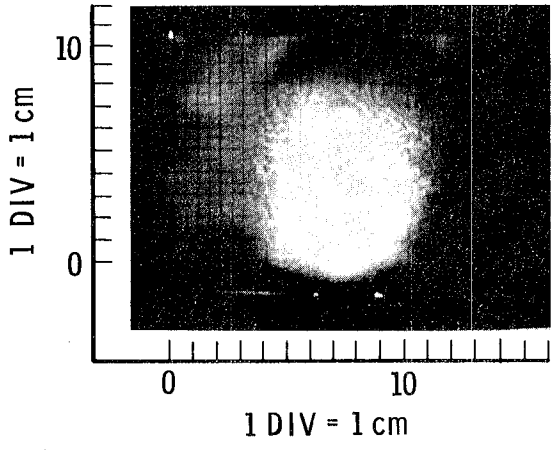

10 pps
E_{OUT} = 63 mJ

II-10 Nd:YAG Far Field Spot Size Vs. Repetition Rate

the axis of the Glan-prism intracavity polarizer. Then while the laser was running in the long pulse mode, the polarizer-Pockel's cell combination was rotated with respect to the Y-axis of the rod for lowest laser threshold.

After completing the alignment and tuning the laser for lowest long pulse threshold and highest output energy at 1 PPS, a long pulse output (non-Q-switched) at 1079 nm of 80 mJ was obtained with an electrical energy input of 61 joules. At this input, long pulse threshold was 55 μsec. This threshold corresponds to 21% of the total electrical energy input to the lamp which means that long pulse threshold at 1 PPS is approximately 13 joules. This should be compared to the 7 joule threshold obtained for Nd:YAG.

In Q-switch operation of Nd:BeL, the optimum Q-switch time was found to be 115 μsec (compare to 151 μsec for Nd:YAG). This means that at the time the Q-switch pulse occurs, only 58% of the lamp output is used for pumping the Nd:BeL rod.

The Q-switched output energy of the Nd:BeL rod as a function of input energy up to Q-switch time was measured for several repetition rates between 1 pulse/15 secs and 10 pulses per sec (10 PPS). This data is plotted in Figure II-7 for comparison to Nd:YAG. The Q-switch pulse width as a function of input energy (up to Q-switch time) at different repetition rates is plotted in Figure II-8. As expected the pulse width narrows with increasing energy input. At 35 joules and 1 PPS the pulse width from Nd:BeL is approximately 28 nanosec compared to 9 nanosec from Nd:YAG. However, as shown in Figure II-9, at a 35 joule input up to Q-switch time (61 joule electrical energy input to lamp), the pulse width appears to be larger at 1 PPS than at 1 pulse/15 secs and then narrows by 3 nanosec when the repetition rate increases from 1 PPS to 10 PPS. This is the opposite of the behavior in Nd:YAG. The precision of the pulse width measurements is $\pm$ 2 nanosecs and clearly further work is required to verify this type of response.

The decrease in output energy with increasing repetition rate will be examined in more detail on the following pages.

Using the technique described previously, beam profile measurements on Nd:BeL were performed. At an energy input (up to Q-switch time) of 35 joules (61 joules total electrical energy input to lamp) and at a distance of 44.6 meters from the laser, the far field spot size as a function of repetition rate (1 PPS to 10 PPS) was photographed.

The first attempt to measure the far field spot size was accomplished by first tuning the output mirror for lowest threshold and highest output energy at a pulse repetition rate of 1 PPS and then recording the spot pattern as the repetition rate was increased from 1 PPS to 10 PPS without retuning the mirror at each repetition rate. The results of this test are shown in Figure II-11 where the far field spot pattern is grossly asymmetric with multiple maximums.

Further testing showed that the output beam profile was very sensitive to output mirror adjustment. The output energy is less sensitive to mirror adjustment while the threshold is least sensitive to mirror adjustment. By adjusting the output mirror while observing the far field pattern one can obtain a circular pattern with the highest energy output and lowest threshold (see Figure II-12).

It was further discovered that if the output mirror was adjusted for a circular pattern and highest output energy at 1 PPS (upper left photo of Figure 12), then when the pulse repetition rate was increased to 10 PPS, the far field spot pattern becomes distorted as shown in the lower photo of Figure 11. Then by adjusting the output mirror at 10 PPS, the output energy would increase and the far field pattern would again become symmetric as shown in the lower photo of Figure 12. Simularly, if now the repetition rate was reduced back to 1 PPS, the far field pattern would again become distorted as shown in the upper left photo of Figure 11 and the output energy would be lower.

With this in mind, we re-measured the far field spot size as a function of repetition rate by adjusting the output mirror at each repetition rate for a symmetrical spot pattern, highest energy and lowest threshold. This data is shown in Figure II-12. The number of shots on each photograph was varied in accordance with the amount of energy per pulse so as to obtain equivalent

Nd:BeL

FAR FIELD SPOT PATTERN vs REPETITION RATE
EFFECT OF IMPROPER MIRROR ALIGNMENT
DISTANCE = 44.6 meters,
ENERGY INPUT = 35 Joules

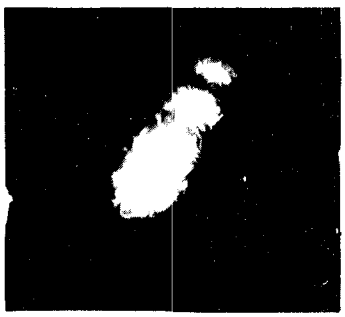

1 pps
E_{OUT} = 81 mJ

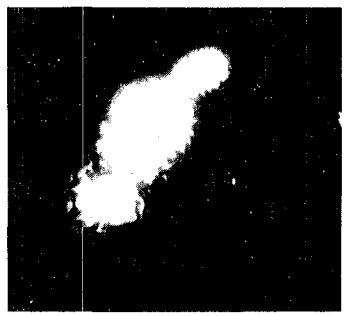

5 pps
E_{OUT} = 47 mJ

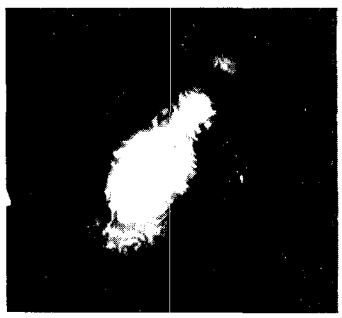

3 pps
E_{OUT} = 56 mJ

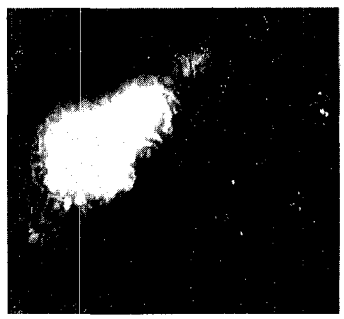

7.5 pps
E_{OUT} = 36 mJ

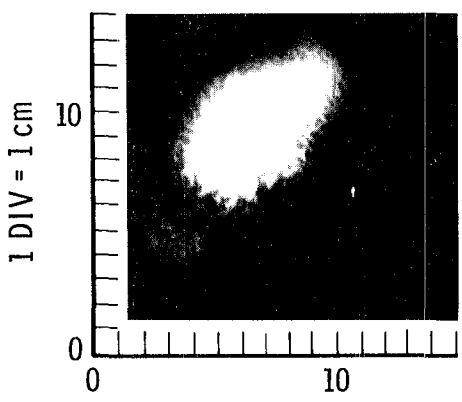

10 pps
E_{OUT} = 28 mJ

II-11 Nd:BeL Far Field Spot Pattern Vs. Repetition Rate With Improper Mirror Alignment

Nd:BeL

FAR FIELD SPOT SIZE vs REPETITION RATE

DISTANCE = 44.6 meters,

ENERGY INPUT = 35 Joules

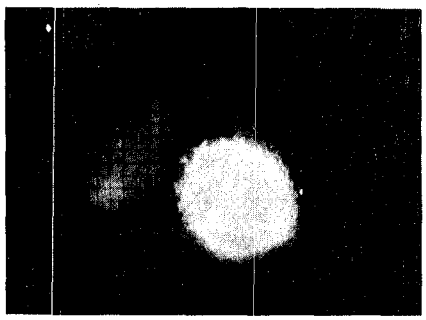

1 pps

E_{OUT} = 89 mJ

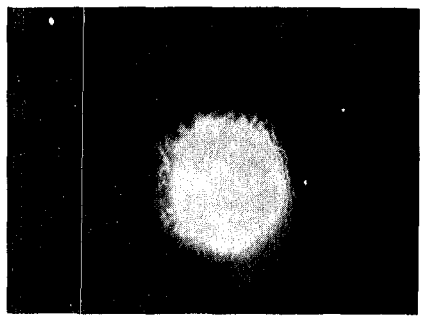

5 pps

E_{OUT} = 50 mJ

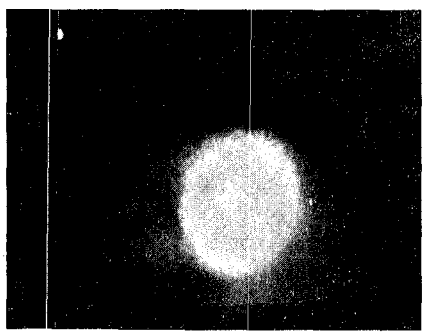

3 pps

E_{OUT} = 61 mJ

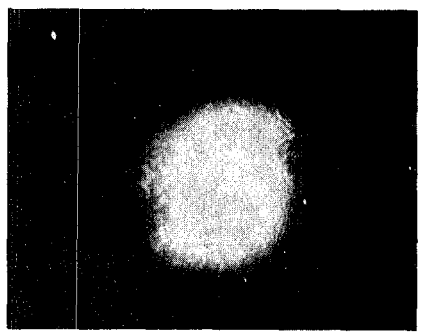

7.5 pps

E_{OUT} = 37 mJ

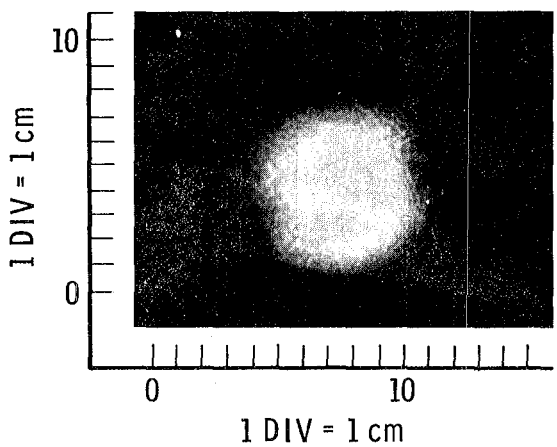

10 pps

E_{OUT} = 30 mJ

II-12 Nd:BeL Far Field Spot Pattern Vs. Repetition Rate With Output Mirror Adjusted at Each Repetition Rate

Beam Divergence vs Pulse Repetition Rate

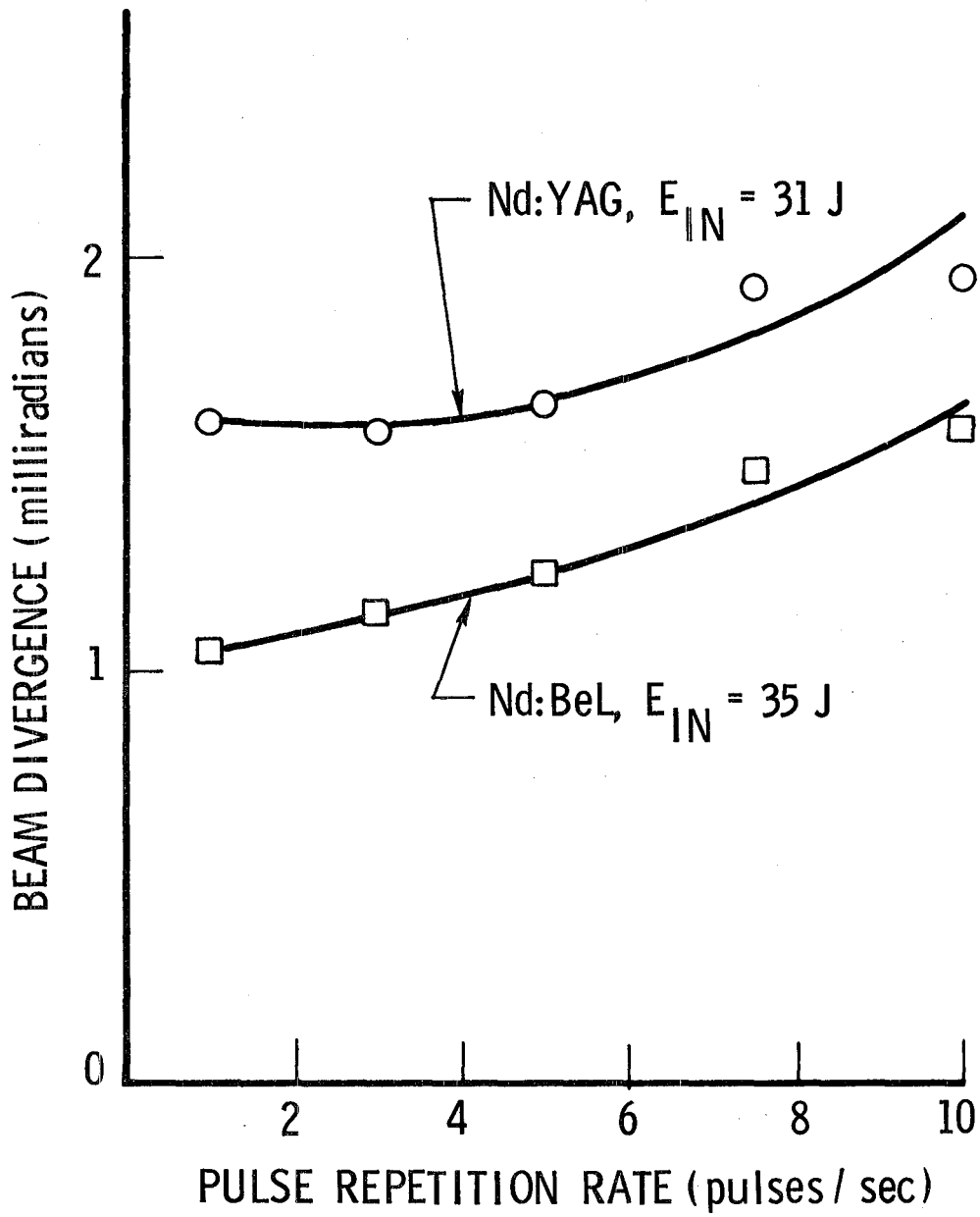

II-13 Beam Divergence as a Function of Pulse Repetition Rate for Nd:YAG and Nd:BeL

exposures. Thus the number of shots at 10 PPS was three times that at 1 PPS since the energy per pulse at 10 PPS was 1/3 the energy per pulse at 1 PPS.

At 1 PPS the spot size at 44.6 meters was 5.1 cm in diameter giving a full width beam divergence of 1.04 milliradians. The beam divergence as a function of repetition rate for Nd:BeL is plotted in Figure II-13. We see that for a 35 joule input up to Q-switch time (61 joules total electrical energy input to lamp) the beam divergence increased only slightly from 1.04 mrad at 1 PPS to 1.58 mrad at 10 PPS. This is a 50% smaller beam divergence than Nd:YAG. However, the Nd:BeL is operating at less than twice threshold while the Nd:YAG is very close to saturation.

Since the data of Figure II-7 (Q-switch energy out vs energy in as a function of repetition rate) was taken without readjustment of the output mirror at each repetition rate, it was necessary to repeat a portion of this test. The test for Nd:BeL was performed at the highest input energy of 35 joules up to Q-switch time which corresponds to 61 joules electrical energy input to the lamp. Q-switch output energy was measured as a function of pulse repetition rate from 1 PPS to 10 PPS. First a run was made without any mirror adjustment at each repetition rate and then a second run was made where the output mirror was adjusted at each repetition rate. This data is plotted in Figure II-14 and compared to Nd:YAG. At 10 PPS a 25% increase in output energy was obtained when the output mirror was adjusted. However, at 10 PPS, the energy output from Nd:BeL was 1.6 times less than Nd:YAG for the same energy input (35 joules up to Q-switch time) whereas Nd:BeL and Nd:YAG both yielded nearly the same output at 1 PPS.

In an attempt to understand this decrease in Q-switch output energy with increasing repetition rate in Nd:BeL, the long pulse output was examined with and without the Glan-prism polarizer in the cavity. The long pulse energy output as a function of repetition rate with and without the intracavity polarizer is compared in Figure II-15 to the Q-switch output energy.

And the long pulse threshold as a function of repetition rate with and without the intracavity polarizer is compared in Figure II-16.

Q-Switched Output Energy
vs
Pulse Repetition Rate
E_{IN}=35 Joules (up to Q-Switch Time)

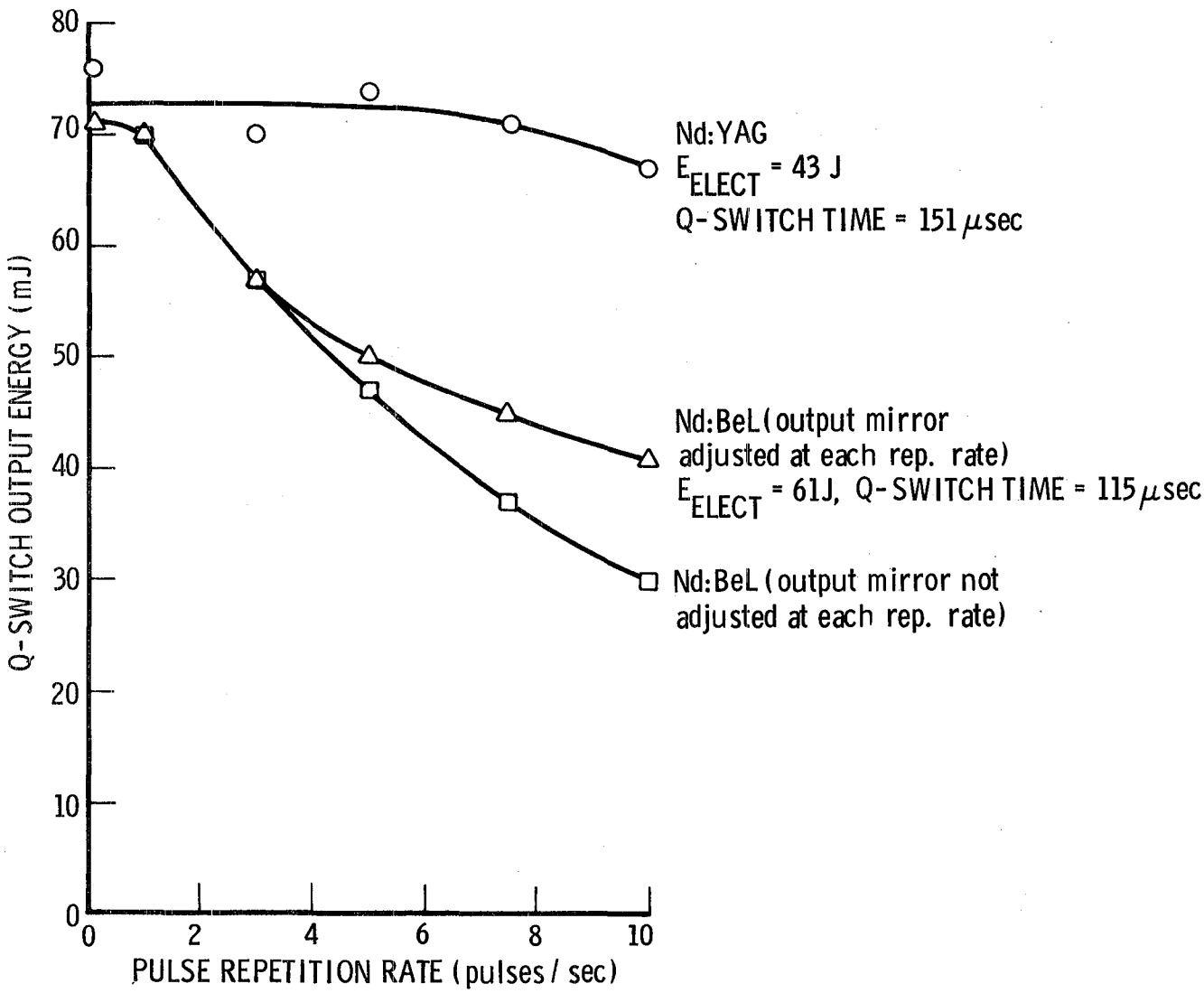

II-14 Q-Switched Output Energy Vs. Repetition Rate With and Without Mirror Adjustment at Each Repetition Rate, Nd:BeL Compared to Nd:YAG

Nd:BeL Output Energy
vs
Pulse Repetition Rate

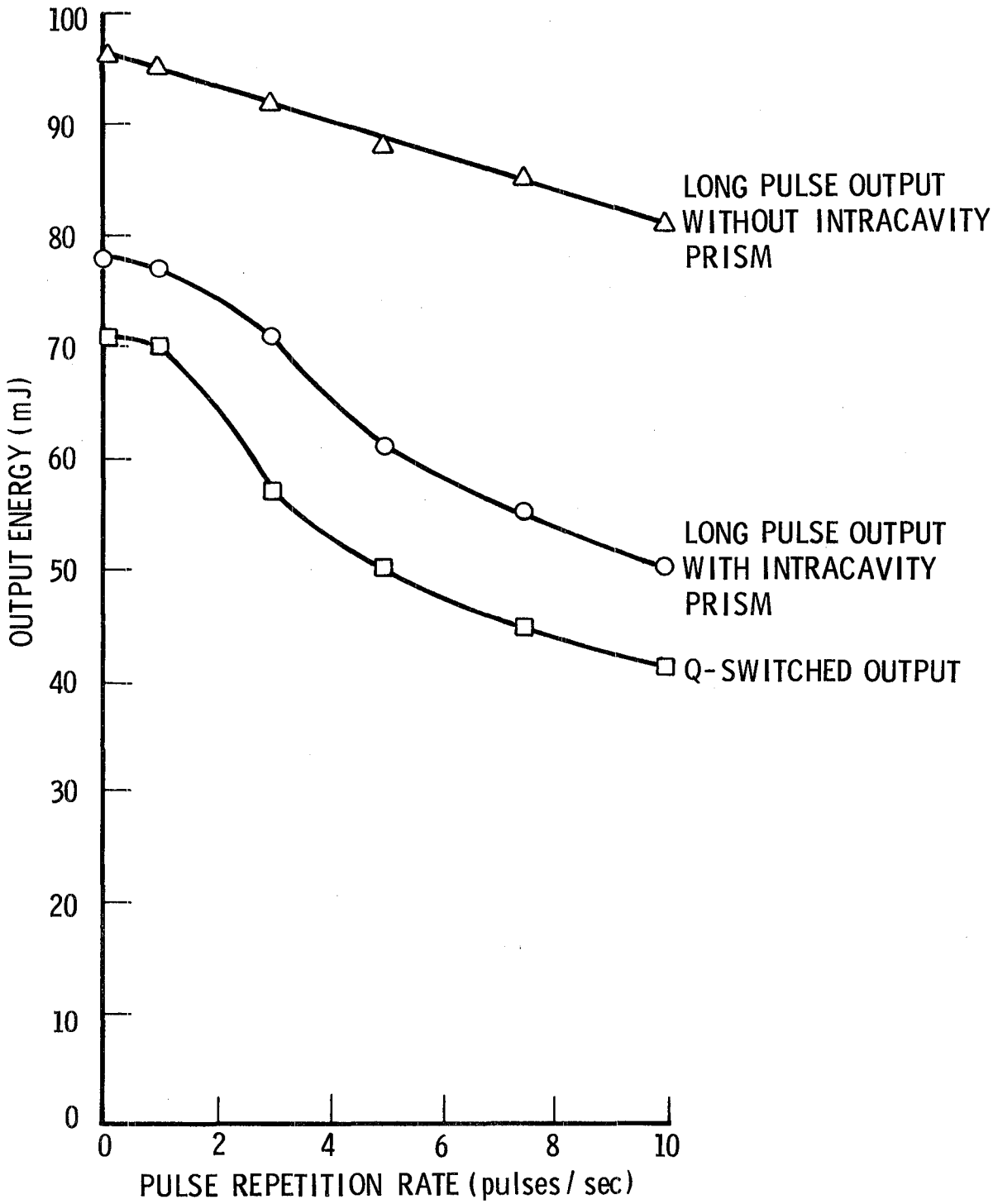

II-15 Nd:BeL Comparison of Long Pulse Output Energy, With and Without Intracavity Prism, to Q-Switch Output Energy as a Function of Repetition Rate

Nd:BeL Long Pulse Threshold vs Pulse Repetition Rate

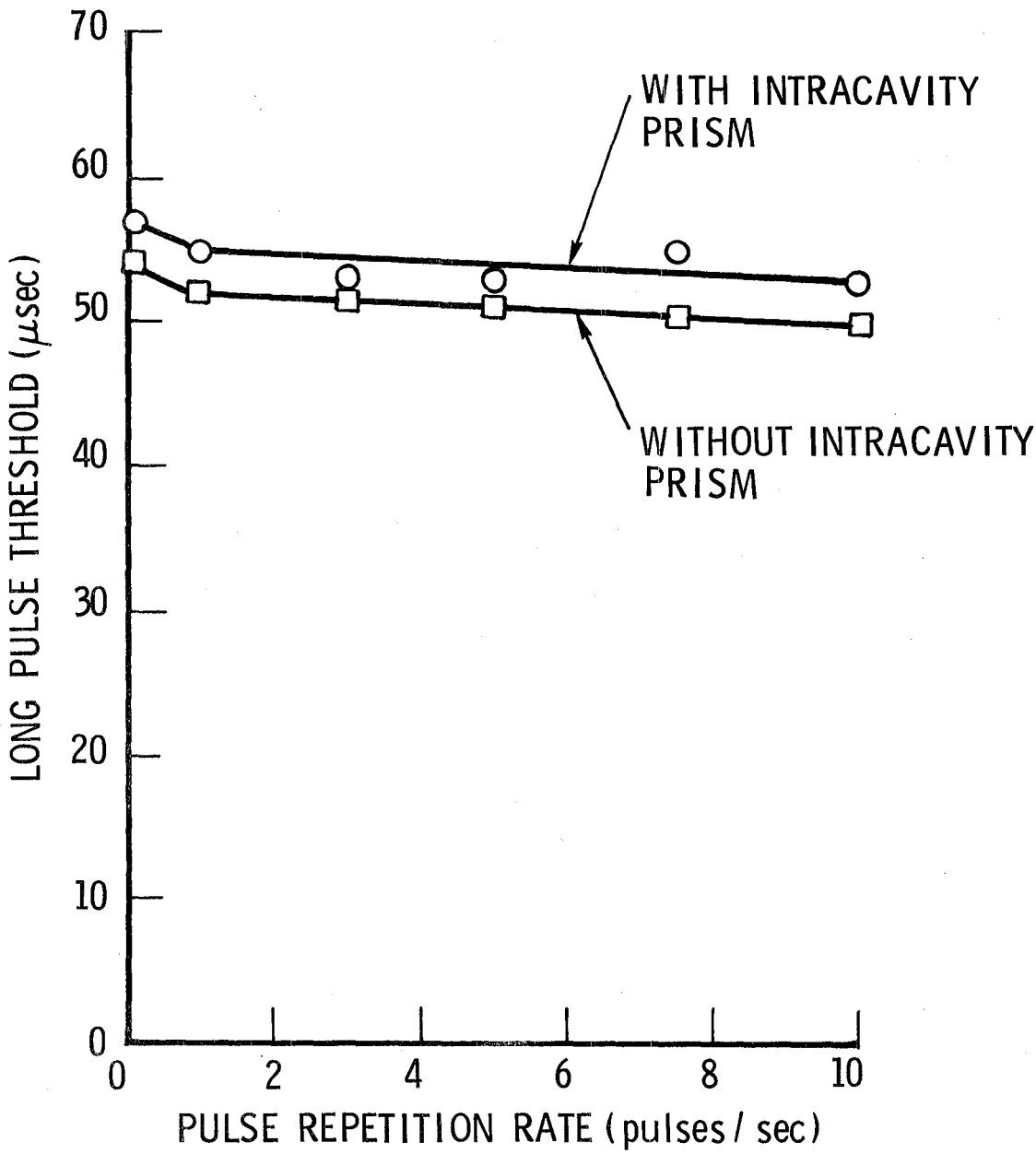

II-16 Nd:BeL Long Pulse Threshold Vs. Repetition Rate With and Without Intracavity Polarizer

As expected, the long pulse output energy with the Glan-prism polarizer inside the cavity is about 10 mJ higher than the Q-switch energy at each repetition rate and exhibits the same decrease with increasing repetition rate as does the Q-switch energy.

When the Glan-prism polarizer was removed from the cavity, the long pulse output energy still decreased with increasing repetition rate although not to the same extent as when the prism was in the cavity. While there was only a 15% decrease in long pulse output from 1 PPS to 10 PPS when the prism was removed from the cavity, there was a 33% decrease in long pulse output from 1 PPS to 10 PPS when the prism was installed in the cavity. In Figure II-16 we observe a slight decrease in long pulse threshold with increasing repetition rate. This was observed both with and without the intracavity polarizer.

Finally the eccentricity of the long pulse output polarization was compared at 1 PPS and 10 PPS without the intracavity Glan-prism. This data is plotted in Figures II-17 and II-18. Zero indicates the direction of the Y-axis of the Nd:BeL rod. Figure II-17 is a plot of the absolute energy output as a function of polarizing angle and Figure II-18 is a plot of normalized output vs. polarizing angle where the curves at 1 PPS and 10 PPS have been normalized to the peak output at 1 PPS and 10 PPS respectively. From this plot it is seen that the eccentricity in the polarization ellipse is the same at 10 PPS and 1 PPS.

Upon receipt of our new power supply, capable of delivering higher average power to the flashlamp, measurements of the Q-switched output energy, from x-axis Nd:BeL, as a function of repetition rate (1 PPS and 10 PPS) was extended to higher input energies to the flashlamp (up to 100 joules). Prior to performing this measurement we verified that the time at which the Q-switch occurred relative to the start of the flashlamp pulse was set to maximize the Q-switch output energy. This test at 1 PPS and a 61 joule electrical energy input to the flashlamp is shown in Figure II-19. This test was repeated at higher repetition rates (up to 10 PPS) and higher input energies and we found that the Q-switch time at which maximum output occurred was not

Nd:BeL

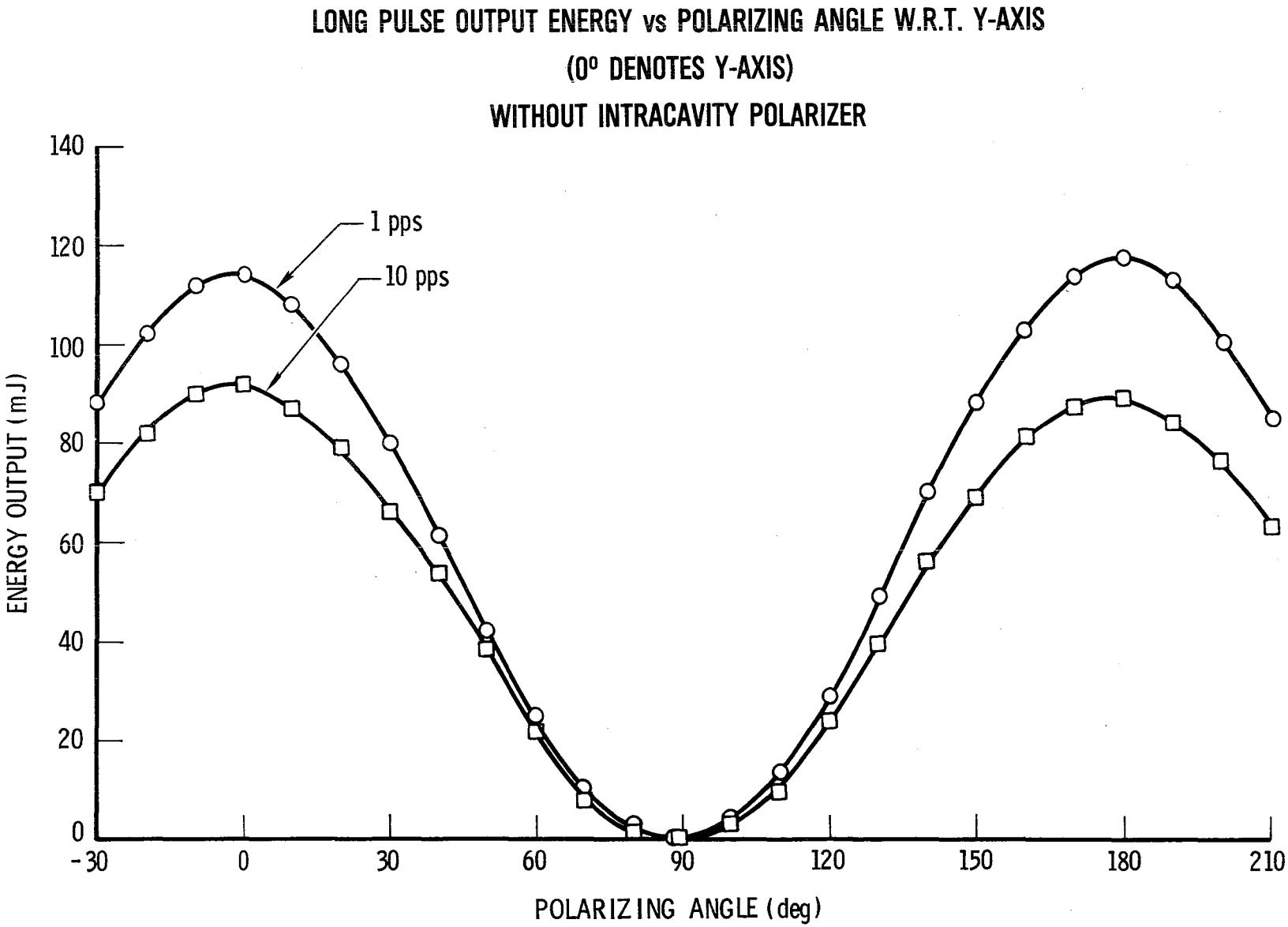

II-17 Nd:BeL Long Pulse Output Energy Without Intracavity Polarizer Vs. Polarizing Angle W.R.T. Y-Axis (0^{o} Denotes Y-Axis)

Nd:BeL

NORMALIZED LONG PULSE OUTPUT vs POLARIZING ANGLE W.R.T. Y-AXIS

(0° DENOTES Y-AXIS)

WITHOUT INTRACAVITY POLARIZER

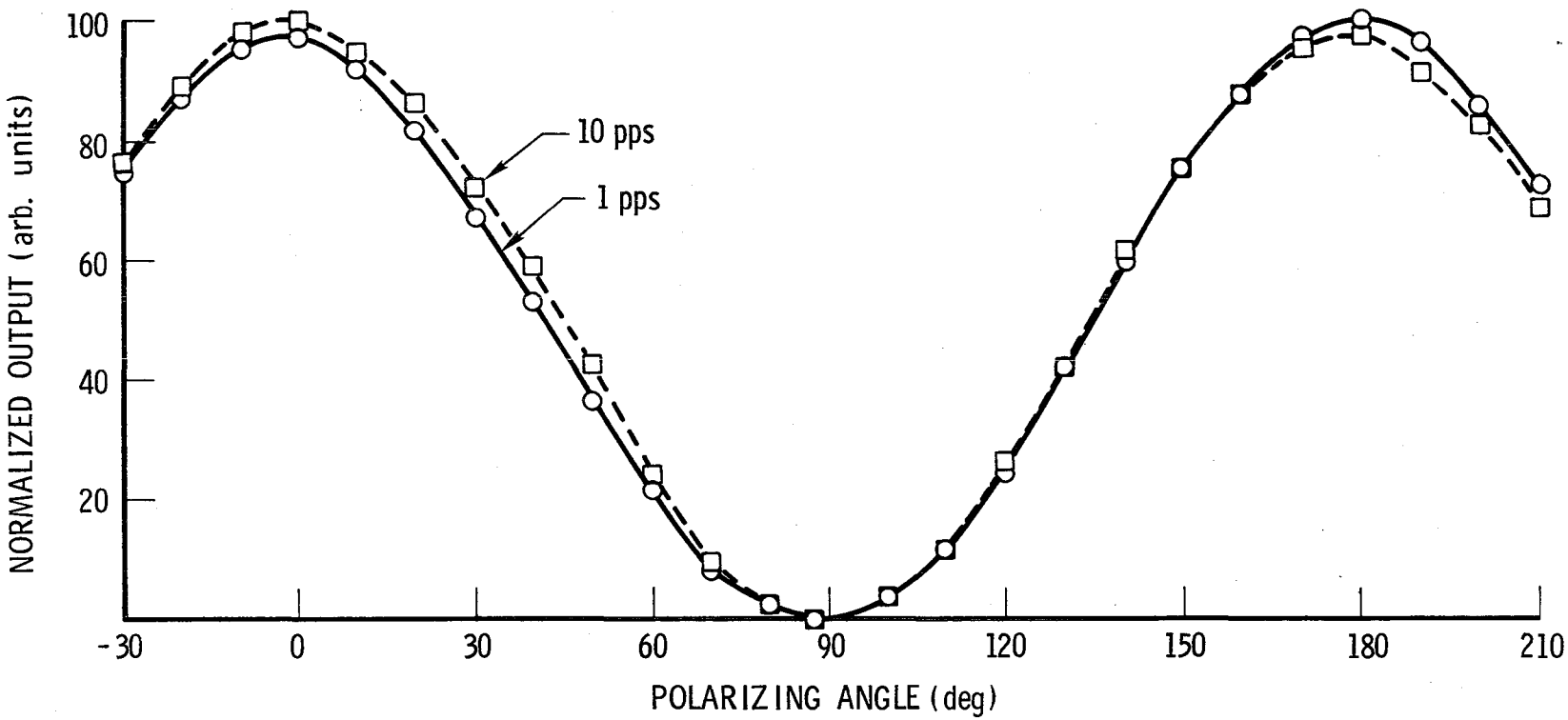

II-18 Nd:BeL Normalized Long Pulse Output Energy Without Intracavity Polarizer Vs. Polarizing Angle W.R.T. Y-Axis (0° Denotes Y-Axis)

X-Axis Nd:BeL
Q-Switch Output vs Q-Switch Time

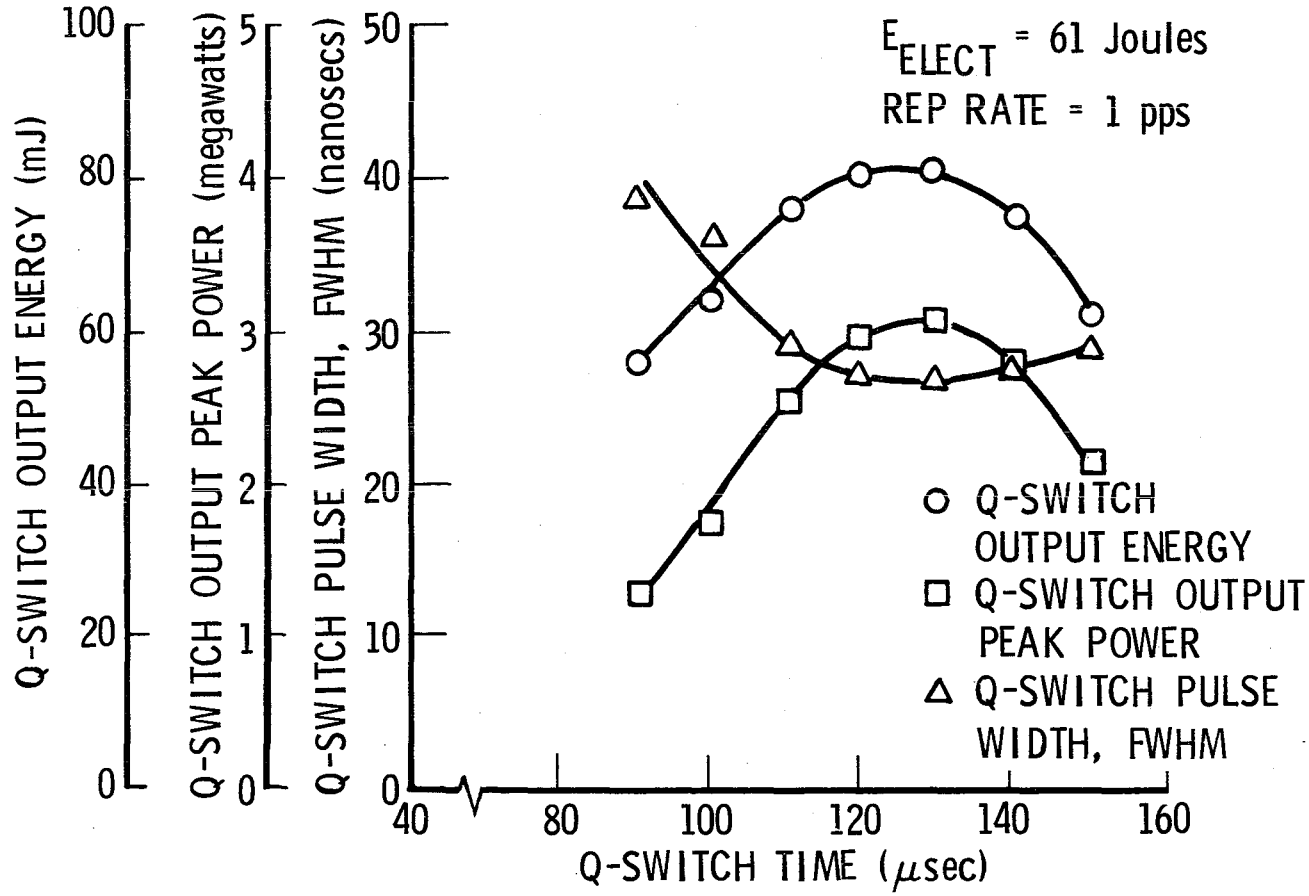

II-19 Q-Switch Output vs. Q-Switch Time for X-Axis Nd:BeL

sensitive to repetition rate or input energy. In Q-switch operation of Nd:BeL, the optimum Q-switch time was found to be 125 μsec (compared to 151 μsec for Nd:YAG). This means that at the time the Q-switch pulse occurs, 60% of the lamp output is used for pumping the Nd:BeL rod.

The Q-switched output energy, peak power, and pulse width (full width at half maximum) as a function of input energy up to Q-switch time were measured at 1 PPS and 10 PPS. These data are plotted in Figures II-20, II-21, and II-22, respectively. The tests were carried out up to 100 joules electrical energy input to the flashlamp. This corresponds to 60 joules input up to Q-switch time. At this point, the Q-switch energy output from x-axis Nd:BeL at 10 PPS was 60% lower than at 1 PPS. The Nd:YAG rod saturated at about 30 joules input at 1 PPS and about 40 joules input at 10 PPS. The saturated output energies were nearly the same at both repetition rates. However, for x-axis Nd:BeL, the output energy at 60 joule input and 1 PPS was a factor of 2 higher than the saturated output of Nd:YAG, but the output energy at 60 joules input and 10 PPS was only 1.2 higher than the saturated output of Nd:YAG.

In Figure II-22 we see that for both Nd:YAG and Nd:BeL, in general, for a given input energy, the pulse width at 10 PPS was wider than at 1 PPS and for both 1 PPS and 10 PPS, the pulse width narrows as the input energy is increased. An exception to this rule occurred at the 47 joule input and 51 joule input at 10 PPS for Nd:BeL. A double humped Q-switch pulse occurred with a full width at half-maximum which was 48 nsec wide as compared to 28 nsec wide at 40 joule input and 31 nsec wide at 60 joule input. This behavior is reflected in the flattening out of the peak power curve at this point in Figure II-21. The tests were repeated several times and this curious behavior occurred each time.

E. Thermally Induced Birefringence

A possible explanation for the decrease in Q-switch output energy with increasing pulse repetition rate of the Nd:BeL laser is a depolarization loss due to thermally induced stress birefringence.

Input/Output Curves
vs Pulse Repetition Rate

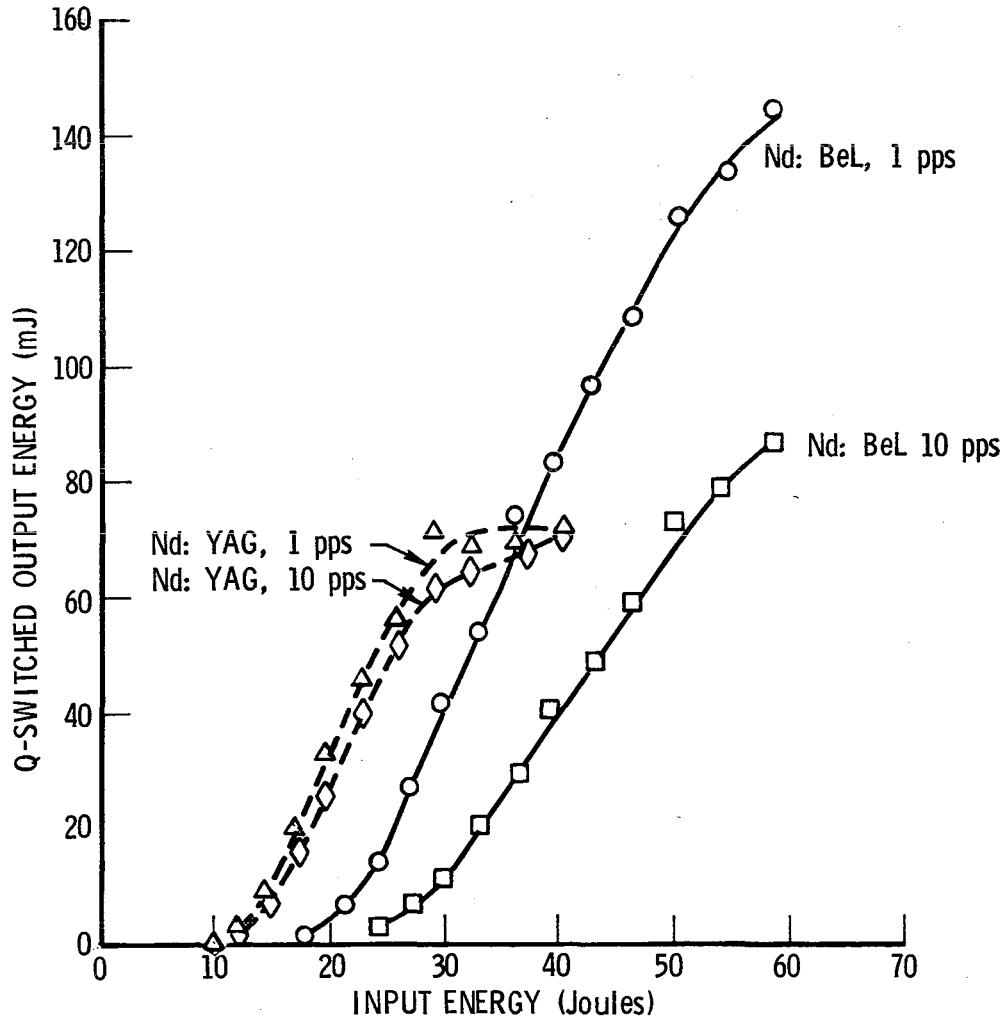

II-20 Q-Switch Energy Output vs. Energy Input Up to Q-Switch Time at 1 PPS and 10 PPS for Nd:YAG and X-Axis Nd:BeL. Tests Extended to 100 Joule Electrical Energy Input to Flashlamp

Q-Switch Peak Power/Input Energy Curves vs Pulse Repetition Rate

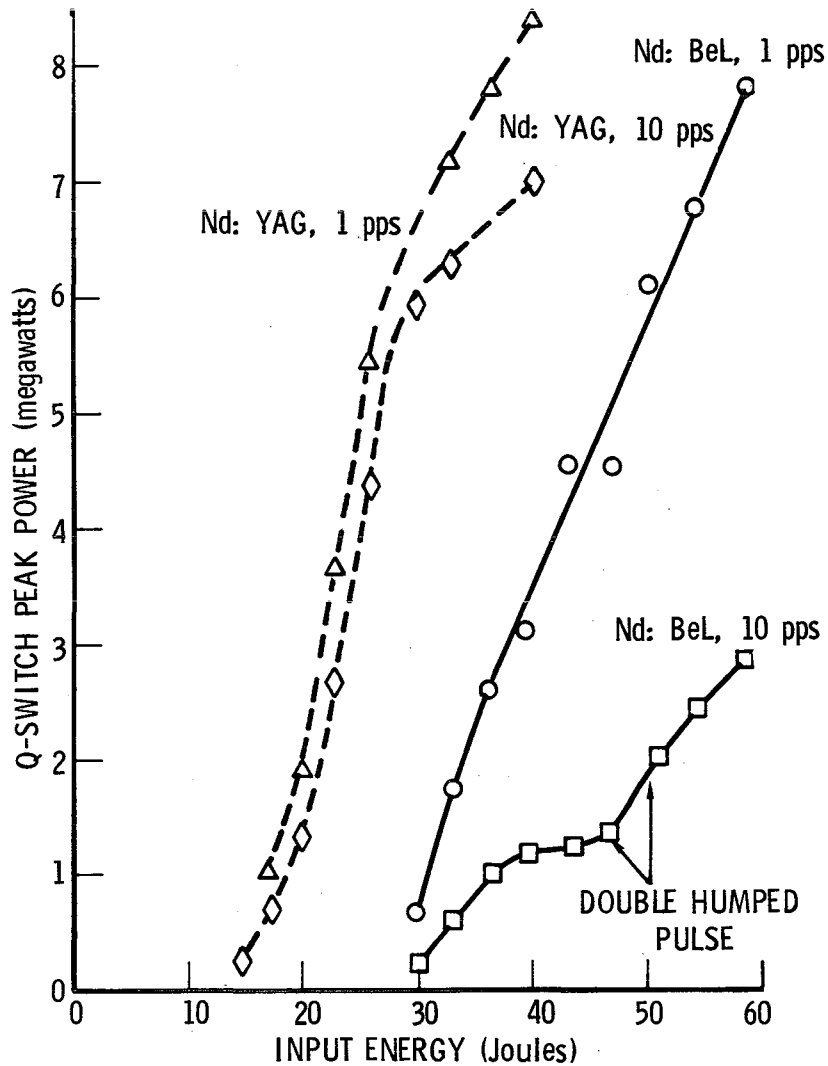

II-21 Q-Switch Peak Power vs. Energy Input Up to Q-Switch Time at 1 PPS and 10 PPS for Nd:YAG and X-Axis Nd:BeL. Tests Extended to 100 Joule Electrical Energy Input to Flashlamp

Q-Switch Pulse Width/Input Energy Curves vs Pulse Repetition Rate

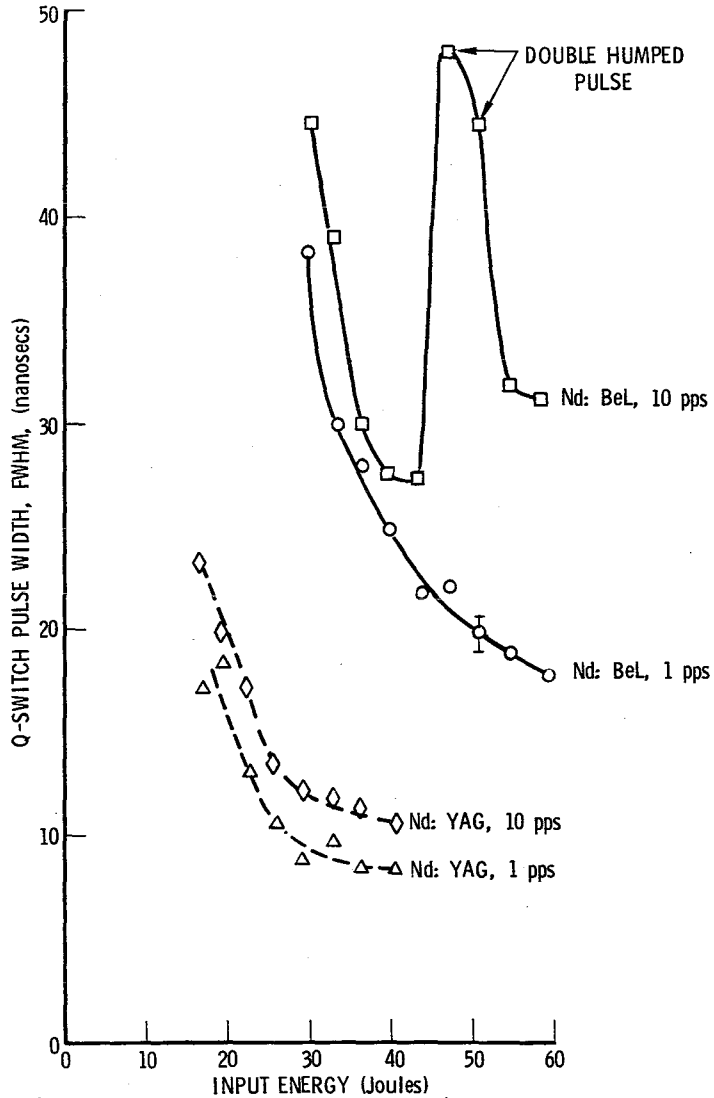

II-22 Q-Switch Pulse Width vs. Energy Input Up to Q-Switch Time at 1 PPS and 10 PPS for Nd:YAG and X-Axis Nd:BeL. Tests Extended to 100 Joule Electrical Energy Input to Flashlamp.

The thermally induced transverse stresses are in radial and tangential directions - relative to the coordinate system shown in Figure II-23 - the local indicatrix also orients its axis in these directions.[4] Consider the point $P_{(r,\phi)}$ in a plane perpendicular to the rod axes. At this point we have a radial refractive index component n_r, which is inclined at an angle ϕ with respect to the Z axis and a tangential component n_ϕ perpendicular to n_r. $\vec{E}$ is the polarization vector for incident radiation. Radiation incident at point P can be resolved into two components, one parallel to n_r, and the other parallel to n_ϕ. Since $\Delta n_r \neq \Delta n_\phi$ there will be a phase difference between the two components and the light will emerge elliptically polarized. This will occur for all points of the rod cross section with exception for points located along the y and z axes of Figure II-23. Radiation incident along the y axis will see only one refractive index, n_r, while along the z axis, n_ϕ will be the only refractive index. As a consequence, a linearly polarized beam passing through the laser rod may experience a substantial depolarization.

A laser resonator containing a polarizing element is optically equivalent to a laser rod of twice the actual length located between a polarizer and analyzer. For a system with intracavity polarizer, the effect of depolarization involves coupling a fraction of the circulating power into the orthogonal state of polarization followed by a subsequent ejection of that component from the cavity by the polarizer and represents the depolarization loss of the resonator.

To investigate if thermally induced birefringence was responsible for the decrease in output energy with increasing repetition rate of the Nd:BeL laser, the following experiment was performed. The mirrors were removed from the Q-switch laser resonator. The flashlamp pumped x-axis Nd:BeL laser rod (5 x 50 mm) was studied in a polariscopic arrangement in which the expanded and collimated light beam from an Argon ion laser serves as an illuminator for the observation of the rod between crossed polarizers as shown in Figure II-24. If thermally induced birefringence is significant, the probe light will suffer depolarization and be partially transmitted by the analyzer.

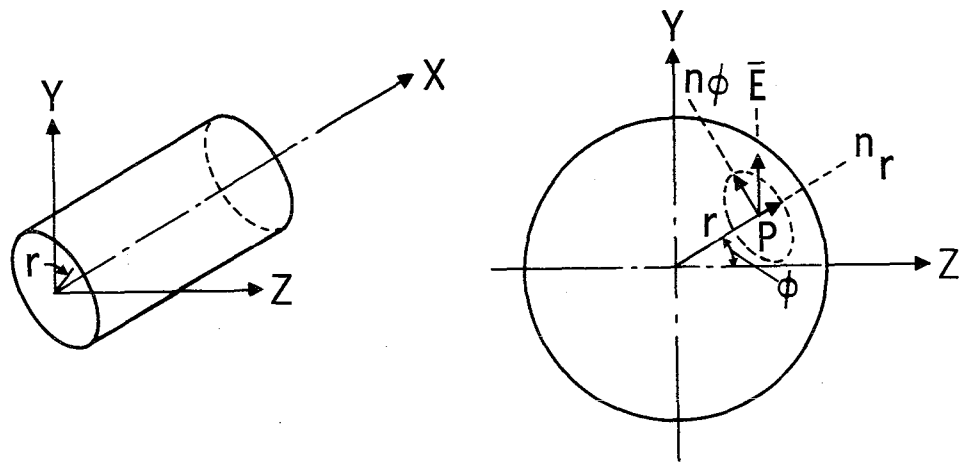

II-23 Crystal Orientation for a Laser Rod (left) and Orientation if Indicatrix of a Thermally Stressed Laser Rod in a Plane Perpendicular to the Rod Axis (right)

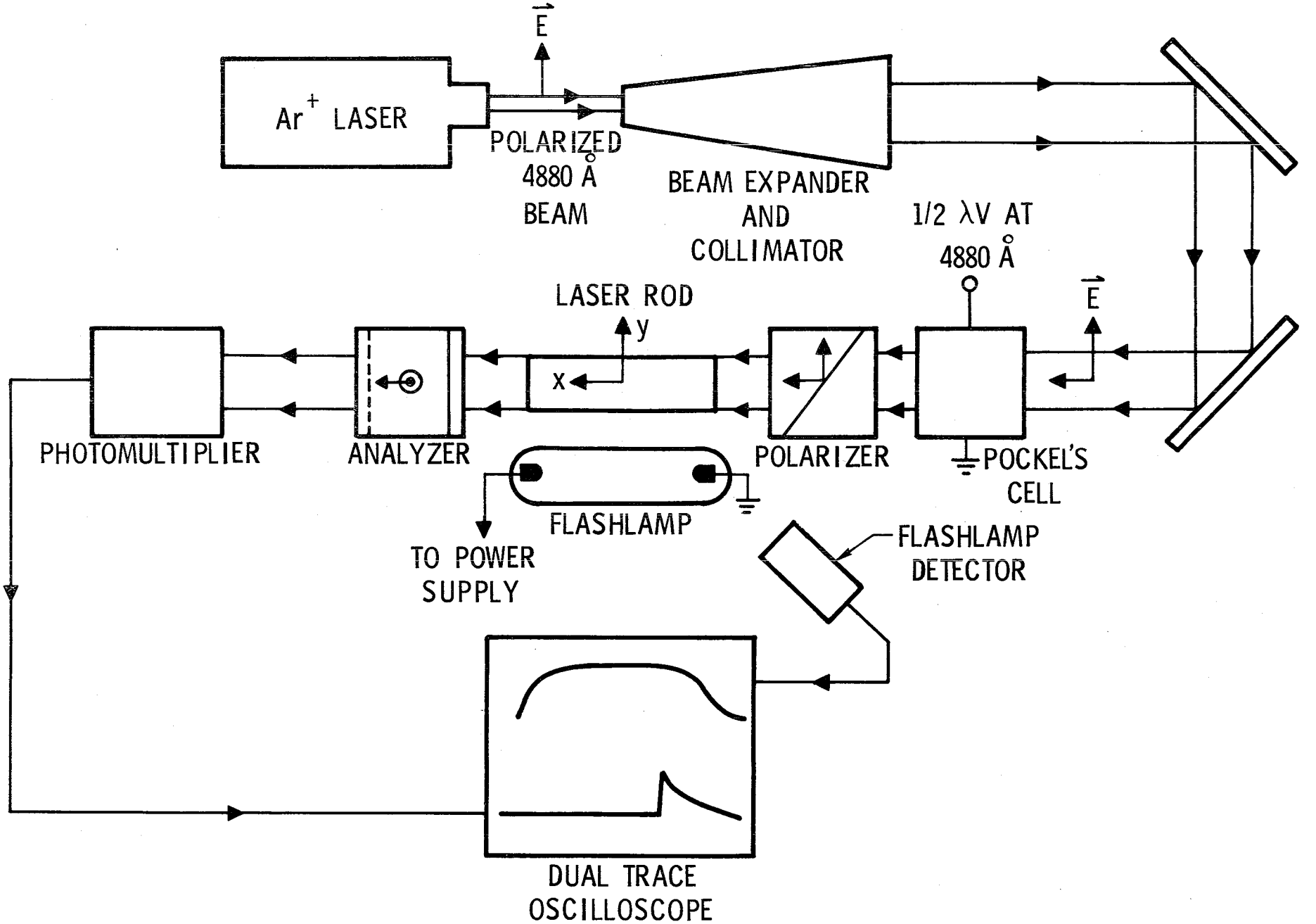

II-24 Experimental Arrangement for Measuring Depolarization Due to Thermally Induced Stress Birefringence

The Argon ion laser was operated at 4880 Å with the beam polarized parallel to the y-axis of the Nd:BeL laser rod. The input polarizer was also aligned parallel to the y-axis of the rod. The 4880 Å power incident on the Nd:BeL rod was about one watt. This power level was necessary in order for there to be a detectable signal on the photomultiplier. The wavelength of the probe beam was chosen to be 4880 Å since the absorption in Nd:Bel at this wavelength is small. This reduced the possibility of interferring thermal effects caused by heating of the rod which in turn was due to absorption of the probe beam. In order to observe the integrated effect resulting from the depolarization of the beam occurring at every point of the rod cross section, the probe beam was expanded and recollimated to the diameter of the laser rod (5 mm).

Our intent was to measure the amount of induced depolarization of the probe beam at the time the Q-switch pulse normally occurs after the initiation of the flashlamp (125 μsec). To accomplish this, a Pockel's cell was used to rotate the probe beam orthogonal to the polarizer thereby preventing the Nd:BeL rod from being exposed to the beam. At 125 μsec after the initiation of the flashlamp pulse, the Pockel's cell was switched on and the amount of 4880 Å probe light transmitted by the analyzer was detected on the photomultiplier. To eliminate interference from the flashlamp, a 4880 Å narrow band filter and aperture was placed in front of the photomultiplier and the photomultiplier located 8 meters from the Nd:BeL rod. The ouput of the photomultiplier was connected to the lower trace of a dual beam scope and the flashlamp pulse displayed on the upper trace. As shown in Fig. II-24 any light transmitted by the analyzer during Q-switch time would have been detected as a pulse with a 1msec decay time (decay time of Klytron switch) on the lower trace. Signals as little as 0.01% of the incident light were capable of being detected.

The experiment was performed with an electrical energy input to the flashlamp of 53 joules. No signal was detected as the pulse repetition rate was increased from 1 pulse per second to 10 pulses per second. Our conclusion is that there is negligible depolarization caused by thermally induced

birefringence in Nd:BeL. Therefore, this effect cannot be responsible for the decrease in Q-switch output energy with increasing repetition rate.

F. Q-Switch Laser Tests with Dielectric Mirror

It was discovered that when we placed the fused silica double-stacked resonant reflector (which had been used as the output reflector of the laser) between the Nd:BeL laser rod and analyzer that a very slight depolarization of the probe beam was experienced which could not be nulled out by the analyzer. This effect existed even when the flashlamp was not pumping the rod. Now it is well known that in crystalline quartz, light propagating normal to the optic axis with the polarization at some angle to the optic axis will result in a depolarization of the beam. In fused silica, this effect should ideally be very small and this is what we observed.

It is difficult to explain how a fused quartz resonant reflector exhibiting such a small mount of anisotropy could account for the drop in output energy of the Q-switch laser at higher repetition rates. Nevertheless, to eliminate this possibility, we replaced the resonant reflector with a dielectric coated mirror with 45% reflectivity and repeated the test shown in Figure II-20. That is, we measured the Q-switch output energy as a function of input energy at 1 pulse per second and at 10 pulses per second. The result was the same as we had observed with the quartz resonant reflector, namely, a 40% reduction in output energy at 10 PPS.

G. Thermal Lensing

In a further effort to understand the behavior of the Nd:BeL laser with respect to the fall off in output energy with increasing repetition rate, the following model was adopted. The combined effects of the temperature and stress-dependent variation of the refractive index and the distortion of the end-face curvature of the rod is such that to a first approximation the rod behaves as an ordinary thick lens having a well defined focal length. An equivalent system is a non lens like laser rod with two plane convex lenses inside the cavity one on each side of the rod. A knowledge of the focal length of the laser allows one to calculate the effective radius of curvature of the lenses through the use of the thick lens formula[5]:

$$R = f(n-1) \quad 1 + \left[\sqrt{1 - \frac{Ln}{f}}\right] \tag{1}$$

where R is the effective radius of curvature, f is the focal length, n is the index of refraction (n_y = 1.9974 for x-axis Nd:BeL), and L is the length of the rod (L = 5 cm).

This system is further equivalent to a laser resonator with concave spherical mirrors of equal curvature, R. Knowledge of R, allows one to calculate the radius of the beam waist, w_o, at the center of the resonator through use of the formula[6]

$$w_o = \left[\frac{\lambda}{2\pi} \sqrt{d(2R-d)}\right]^{1/2} \tag{2}$$

where λ is the laser wavelength (1079 nm for x-axis Nd:BeL) and d is the length of the laser resonator (d = 41 cm, see Figure II-3). If the focal length is very long, so that the radius of curvature of the equivalent mirrors is large compared to the cavity length, then the beam waist at the mirrors will be nearly equal to that at the center of the cavity. In this case the mode volume in the rod will approximate a cylinder of length L, and radius, w_o.

$$V = \pi w_o^2 L \tag{3}$$

We see then that the mode volume of the laser will decrease as the square root of the focal length

$$V \propto f^{1/2} \tag{4}$$

If the rod is isotropic with respect to the thermal conductivity and coefficient of thermal expansion (which is the case for Nd:BeL to a first approximation), then the simple lensing of the laser rod is the result of uniform heat generation throughout the cylindrical laser which is cooled at the cylindrical surface. This results in a quadratic radial temperature distribution and a thermal strain. As a consequence, this in turn causes index of refraction variations in the rod via dn/dT and the photoelastic effect. Perturbations on these principal thermal distortions occur in laser rods near the ends, where the free surface alters the stress character. The so-called end effects account for the physical distortion in the flatness of the rod ends via the coefficient of thermal expansion.

According to Koechner[4], the combined effects of the temperature and stress-dependent variation of the refractive index and the distortion of the end face curvature of the rod lead to the following expression for the focal length

$$f_{r,\phi} = \frac{KA}{\eta P_{IN}} \left[\frac{1}{2} \frac{dn}{dT} + \alpha C_{r,\phi} n_o^3 + \frac{\alpha r_o (n_o - 1)}{L} \right]^{-1} \tag{5}$$

where K is the thermal conductivity, A is the cross sectional area of the laser rod, $\frac{dn}{dT}$ is the change in refractive index with temperature, α is the coefficient of thermal expansion, r_o is the radius of the laser rod, n_o is the index of refraction, L is the length of the laser rod, P_{IN} is the average input power and η is the efficiency factor which relates the electrical input power to the power dissipated as heat in the rod ($Pa = \eta P_{IN}$). $C_{r,\phi}$ is a function of the photoelastic coefficients and has two values, C_r and C_ϕ, one for the radial and one for the tangential component of the polarized light, respectively. We see then that the rod may act as a bifocal lens with one focal length, f_r, for the radial component and the other being f_ϕ for the tangential component.

We may write Eq. (5) as

$$f = \frac{M}{P_{IN}} \tag{6}$$

where M is a constant dependent on the material parameters. Substituting (6) into (4) we have

$$V \alpha \frac{1}{P_{IN}^{1/2}} \tag{7}$$

For a fixed input energy, the average input power is proportional to the pulse repetition rate, PRR. [$P_{IN} = E_{IN}(PRR)$] so that

$$V \alpha \frac{1}{(PRR)^{1/2}} \tag{8}$$

We see then that an increase in pulse repetition rate will result in a decrease in mode volume in the Nd:BeL rod and a consequential decrease in output energy.

To check this hypothesis we measured the thermally induced focal length as function of repetition rate and calculated the reduction in mode volume through the use of Eqs. (1), (2) and (3) and then compared the ratio of mode volumes at 1 PPS and 10 PPS to the ratio of output energies.

Due to the mild focusing and large distance involved at 1 PPS, it was difficult to measure the focal length at this point. The following procedure was adopted. We measured the focal length at 10 PPS and 7.5 PPS and extrapolated to 1 PPS. The experimental arrangement is shown in Figure II-25 in which the 4880 Å output of an Argon ion laser whose polarization was parallel to the y axis of the Nd:BeL rod was used as the probe beam. The beam was expanded and recollimated to the diameter (5 mm) of the rod. Thermal effects were generated by pumping with a flashlamp in the single elliptical cavity used for the Q-switch laser. The focal length at each repetition rate was found by measuring the transmission of the 4880 Å probe beam through a 800 micron aperture at various distances from the front end of the Nd:BeL laser rod. These results are shown in Figure II-26. With the lamp input energy fixed at 53 joules, the focal lengths measured at 7.5 PPS and 10 PPS were 625 cm and 500 cm, respectively. Comparing our experimental results with Eq. (6) we find that the focal length does not vary exactly as the inverse of lamp input power. Our experimentally determined expression for focal length as a function of input power is

$$f = \frac{649 \text{ meters - watt}^{0.78}}{P_{IN}^{0.78}} \qquad (9)$$

This result is plotted in Figure II-27.

Extrapolating, we find the focal length at 1 PPS to be 2983 cm. Using these results, and Eqs. (1), (2) and (3) we may calculate the effective radius of curvature, R, the beam waist at the center of the cavity, w_o, and the mode volume, $V = \pi w_o^2 L$ respectively for each repetition rate. We may now take the ratio of the mode volume at 10 PPS to the mode volume at 1 PPS and compare this ratio to the ratio of Q-switched output energies at these pulse repetition rates. These results are given in Table II-1 where we observe

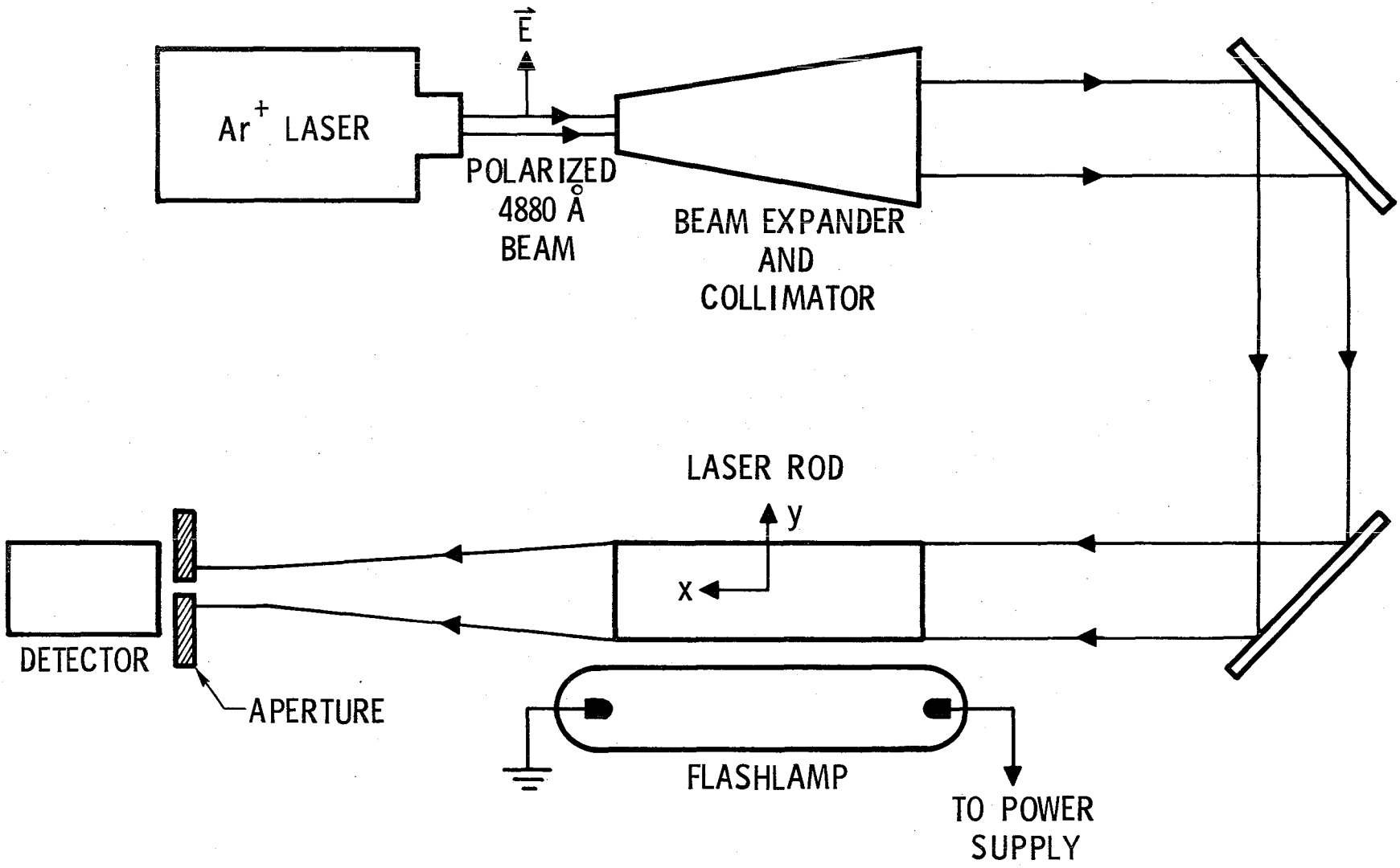

II-25 Experimental Arrangement for Measuring Thermal Lensing

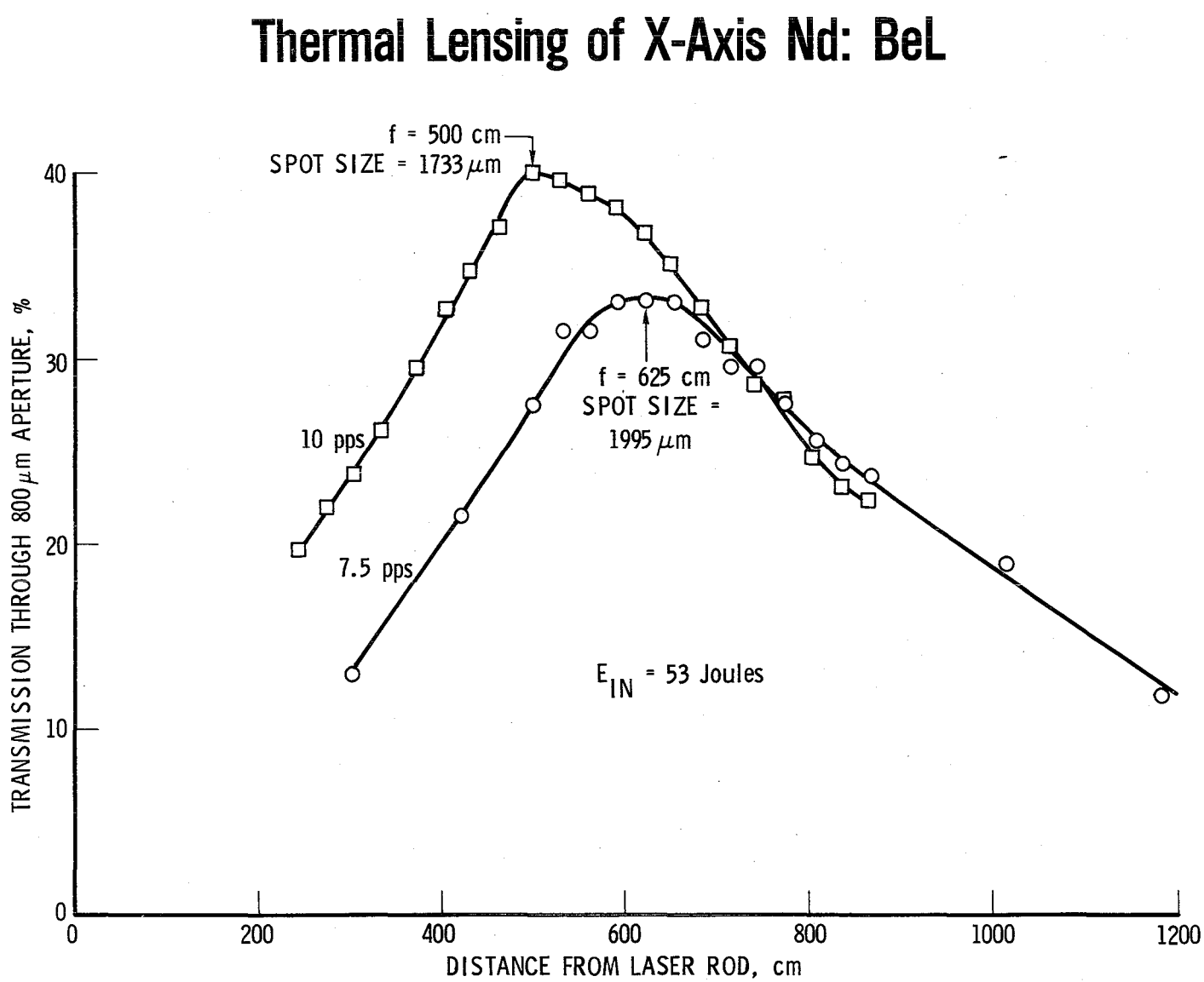

II-26 Thermal Lensing of X-Axis Nd:BeL

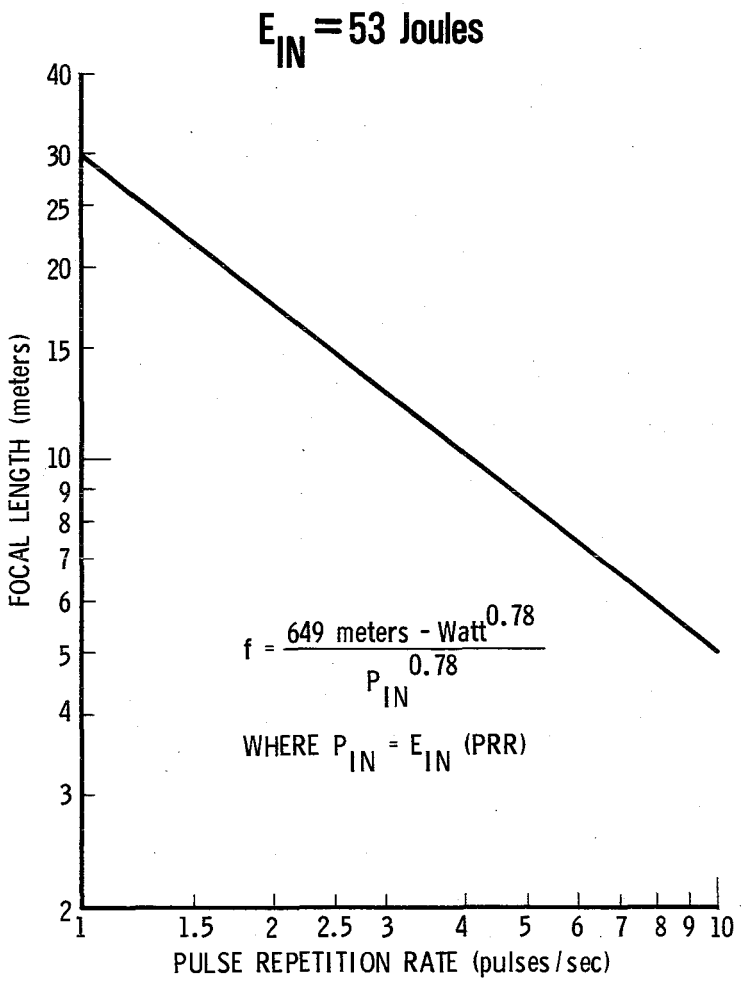

II-27 Thermally Induced Focal Length vs. Pulse Repetition Rate in X-Axis Nd:BeL

TABLE II-1

SUMMARY OF DATA FOR THE COMPARISON OF MODE VOLUME CHANGE TO THE Q-SWITCH ENERGY OUTPUT CHANGE WITH PULSE REPETITION RATE FOR X-AXIS Nd:BeL

Pulse Repetition Rate (pulses/sec)	Focal Length, f (cm)	Effective Radius of Curvature, R (cm)	Beam Waist Radius, w_o (mm)	Mode Volume $V = \pi w_o^2 L$ $(mm)^3$	$\frac{V_{10\ PPS}}{V_{x\ PPS}}$	Q-Switch Output Energy, E_o at 1079 nm (mJ)	$\frac{E_{10\ PPS}}{E_{x\ PPS}}$
10	500	992	0.70	76		30	
7.5	625	1242	0.74	85	0.89	37	0.81
1	2983	5950	1.09	164	0.46	70	0.43

that the percentage decrease in Q-switch output energy with increasing repetition rate is nearly the same as the percentage decrease in mode volume. This strongly supports the belief that the decrease in mode volume as a result of thermal lensing is the reason for the decrease in output energy with increasing average power.

The next question to approach is the possibility of compensating for the thermal lensing so as to regain the output energy at higher repetition rates. Returning to Eq. (5) we recall that the rod may behave as a bifocal lens with different focal lengths for light with radial and tangential polarization, f_r and f_ϕ, respectively. Our experimentally determined focal length is actually an average of these, $f_{meas.} = (f_r + f_\phi)/2$. Normally, a difference in focal length between different polarizations means that a resonator designed to compensate for the rod lensing for radial polarization cannot also compensate for the lensing of tangentially polarized light due to the different values of the photoelastic coefficients, C_r and C_ϕ. However, there are exceptions to this rule as will be shown here.

When we measured the thermally induced focal length of the Nd:BeL rod, we found the focused beam to be radially symmetric about the axis. In addition, the photographs of the far field pattern in Figure II-12 are also radially symmetric. The conclusion drawn from these observations is that the Nd:BeL rod does not act as a bifocal lens, that is $f_r = f_\phi$. This being the case and using Eq. (5) we can write the average of f_r and f_ϕ as

$$f = \frac{f_r + f_\phi)}{2} = \frac{KA}{\eta P_{IN}} \left[\frac{1}{2} \frac{dn}{dT} + \frac{\alpha (C_\phi + C_r) n_o^3}{2} + \frac{\alpha r_o (n_o - 1)}{L} \right]^{-1} \qquad (10)$$

This must be equated to our experimentally determined function for the focal length (repeating Eq. 9)

$$f = \frac{M}{P_{IN}^n} \qquad (11)$$

where $n = 0.78$ and $M = 649$ meters - watt$^{0.78}$.

Solving for C_r and C_ϕ we obtain,

$$\frac{(C_\phi + C_r)}{2} = \frac{1}{\alpha n_o^3}\left[\frac{KA}{\eta M} P_{IN}^{(n-1)} - \frac{1}{2}\frac{dn}{dT} - \frac{\alpha r_o(n_o-1)}{L}\right] \tag{12}$$

We will use for the material parameters, DeShazer's measured values found in Section III of this report. For an x-axis rod, the material parameters along the y and z axes are appropriate, $n_z \simeq n_y = 1.9974$, $\alpha_z = \alpha_y = 11.53 \times 10^{-6}/^oC$, $K_z \simeq K_y = 0.047$ W/cm ^oC[7], $(dn/dT)_y = -7.55 \times 10^{-6}/^oC$, $(dn/dT)_z = -8.35 \times 10^{-6}/^oC$, r_o is the radius of the laser rod, 2.5 mm, A is the cross sectional area of the rod ($A = \pi r_o^2$), 19.6 mm^2, L is the length of the rod, 50 mm, M is 649 meters-$watt^{0.78}$, and n = 0.78. A reasonable estimate of η is $\eta = 0.05$ based on considerations of electrical to optical conversion efficiency of the lamp, cavity efficiency, absorption of pump light, and heat generated due to non-radiative transitions. Using $P_{IN} = E_{IN}$ (PRR) = 530 watts where E_{IN} = 53 joules and PRR = 10 PPS and using $(dn/dT)_y$ for the calculation we find,

$$\frac{C_\phi + C_r}{2} = 4.24 \times 10^{-2} \tag{13}$$

Now, in Section III of this report, DeShazer measures the ratio of thermally induced birefringence per power absorbed in Nd:BeL to that in Nd:YAG as being 1/50, that is

$$\frac{(B/P)_{BeL}}{(B/P)_{YAG}} = \frac{1}{50} \tag{14}$$

DeShazer's B/P ratio is (in Koechner's model[4]) identically equal to

$$\frac{B}{P} = \frac{\alpha n_o^3 L}{KA}\,\frac{C_\phi - C_r}{2} \tag{15}$$

Taking $\lambda_{YAG} = 1064$ nm, $\alpha_{YAG} = 6.95 \times 10^{-6}/^oC$ (from DeShazer), $K_{YAG} = 0.11$ W/cm ^oC[4], $n_{YAG} = 1.82$[4], and putting in the appropriate values for Nd:BeL including $\lambda_{BeL} = 1079$ nm then a ratio yields

$$\frac{(C_\phi - C_r)_{BeL}}{(C_\phi - C_r)_{YAG}} = 4.12 \times 10^{-3} \tag{16}$$

From knowledge of the photoelastic tensor, Koechner[4] calculates $[(C_\phi - C_r)/2]_{YAG}$ to be - 0.00975. Using this in (16) we find

$$\frac{(C_\phi - C_r)_{BeL}}{2} = -4.02 \times 10^{-5} \tag{17}$$

Equations (13) and (17) can now be solved for C_r and C_ϕ.

$$\begin{aligned} C_\phi &= +4.23 \times 10^{-2} \\ C_r &= +4.24 \times 10^{-2} \end{aligned} \tag{18}$$

We see that since the depolarization of the beam is dependent on the difference in C_ϕ and C_r, this effect is quite small. On the other hand the magnitude of C_r and C_ϕ are relatively large and since the contribution of the thermally induced birefringence to the focal length depends on the sum of C_r and C_ϕ, the thermal lensing can be quite large. From knowledge of C_r and C_ϕ and the other material parameters, we may now use Eq. (5) to calculate the magnitude of the various contributions to the focal length.

The contribution to the focal length due to the stress dependent variation of refractive index (thermally induced birefringence) is

$$\frac{\alpha (C_\phi + C_r) n_y^3}{2} = 3.90 \times 10^{-6}/^\circ C \tag{19}$$

The contribution to the focal length due to the temperature-dependent variation of refractive index is

$$\frac{1}{2}\left(\frac{dn}{dT}\right)_y = \frac{1}{2}\left(-7.55 \times 10^{-6}/^\circ C\right) = -3.78 \times 10^{-6}/^\circ C \tag{13}$$

and the contribution to the focal length due to the effect of end face curvature caused by an elongation of the rod is

$$\frac{\alpha\, r_o\, (n_y - 1)}{L} = 0.575 \times 10^{-6}/^{o}C \qquad (14)$$

We see then that the negative $\frac{dn}{dT}$ is responsible for almost completely cancelling the effect due to thermally induced birefringence leaving only the contribution caused by end face curvature of the rod. This would indicate that a loss in output energy at high average input power may be compensated for by grinding concave surfaces on the ends of the rod.

H. REFERENCES

1. Engineering Design of Repetitively Q-Switched Solid State Lasers for Precision Ranging Applications, Final Report, NAS 5-23698, 31 Aug. 1977.

2. J. P. Markiewicz and J. L. Emmett, "Design of Flashlamp Driving Circuits, "IEEE J. Quant. Electr., Vol. QE-2, No. 11, Nov. 1966, pp. 707-711.

3. G. W. Day and C. F. Stubenrauch, "Laser Far-Field Beam Profile Measurements by the Focal Plane Technique", NBS Technical Note 1001, March 1978.

4. W. Koechner: Solid-State Laser Engineering (Springer-Verlag, New York, 1976).

5. F. Jenkins and H. White: Fundamentals of Optics (McGraw-Hill, New York, 1957) pg. 68.

6. H. Kogelnik and T. Li, "Laser Beams and Resonators", Proc. of IEEE, Vol. 54, No. 10, October, 1966, pp. 1312-1328.

7. R. C. Morris, C. F. Cline, R. F. Begley, M. Dutoit, P. J. Harget, H. P. Jenssen, T. S. La France, and R. Webb, "Lanthanum Beryllate: A New Rare-Earth Ion Laser Host", Appl. Phys. Lett., Vol. 27, No. 8, October 15, 1975, pp. 444-445.

III. Thermo-Optic Properties of Neodymium Doped Laser Materials*

A. Introduction

Two experiments were undertaken to measure the thermo-optic properties of neodymium doped $Y_3Al_5O_{12}$ (YAG), $Be_2La_2O_5$ (BeL) and ED2.1 glass. One experiment used a double interferometer to observe simultaneously shifts in Fizeau and Twyman-Green fringes with sample temperature. This technique obtained the coefficient of linear thermal expansion α_ℓ and the thermal variation of the refractive index dn/dT by one procedure. For Nd:YAG, the wavelength dependence of dn/dT was measured from 4579 Å to 1.0642 μm and fitted to a single-resonance theoretical model for dn/dT. This report is the first to give the wavelength variation of the thermo-optic coefficient for YAG and, in particular, at 1.0642 μm. In addition, an accurate technique of determining the temperature variation of birefringence was developed using the beating of Fizeau fringes of orthogonal polarizations.

The other experiment measured the relative stress-induced birefringence of these laser materials and showed that Nd:BeL had at most one-twentieth of the induced birefringence of Nd:YAG. This stress-optic experiment used the new technique of producing radial stress by heating a very small volume (50 μm dia) of the sample with a focused argon-ion laser beam. It is a simple procedure for obtaining relative stress-optic measurements without the difficulties of mechanical stress methods.

Previous measurements of dn/dT and α_ℓ for five solid-state laser materials are listed in Table 1. Ruby ($Cr:Al_2O_3$) is included for a comparison, and in our experiments it was used as a check on our measurements. The thermo-optic coefficient α_n is defined as n^{-1} dn/dT, similar to the

---

*by L. G. DeShazer, K. E. Wilson and C. L. Sauer

Sample	λ (μm)	n	dn/dT (10^{-6}/°C)	α_n (10^{-6}/°C)	α_ℓ (10^{-6}/°C)	Temp. Range (°C)	Ref.
Nd:YAG	0.6328	1.829	7.3	4.0	6.9	28-56°	1
1% Nd:YAG	-	-	-	-	7.5	23°	2
$CaWO_4$							
ord	0.5461	1.925	-7.1	-3.7	7.9(a)	20°	3,4
ext	0.5461	1.942	-10.2	-5.25	12.7(c)		
Nd:CaLaSOAP							
ord	0.6328	1.857	5.1	2.75	6.6(a)	40-160°	5,6
ext	0.6328	1.823	3.8	2.08	8.9(c)		
5% Nd:AOlux 3835 glass	0.6328	1.515	-1.89	-1.25	9.05	25°	7
0.01% Cr: Al_2O_3							
ord	0.5461	1.771	13.1	7.39	5.00(a)	25°	3,8
ext	0.5461	1.763	17.5	9.93	6.66(c)		

Table 1. Previously measured thermo-optic and thermal expansion coefficients for several solid-state laser materials. (In the column for α_ℓ "a" labels expansion along a-axis, "c" labels expansion along c-axis)

definition for the coefficient of linear thermal expansion α_ℓ as L^{-1} dL/dT. The importance of α_n lies in the fact that the relative thermal change in the optical path length $(nL)^{-1}$ d(nL)/dT equals the sum of the coefficients, $\alpha_\ell + \alpha_n$. In general, our measurements agreed with these past determinations except, significantly, for α_n of Nd:YAG which was 40% higher. We performed many experimental checks for YAG and since our maximum experimental error was 5%, our value of 5.66×10^{-6}/°C for α_n at 6328 Å is considered correct. Our value of α_ℓ for YAG agreed almost exactly with the previous measurement of α_ℓ.

B. Fizeau and Twyman-Green Interferometry

1. Theory

The thermo-optic and thermal expansion coefficients, α_ℓ and α_n, were measured by a double interferometric arrangement shown in Fig. 1. This interferometer is basically the method devised by Fizeau[9] for determining the coefficient of thermal expansion, except a Twyman-Green interferometer has been added in order to determine simultaneously the thermo-optic coefficient. Cabezas et al.[10] first used this double interferometer technique to measure temperatures of materials during pumping in a laser amplifier. We utilized this approach to measure α_n and α_ℓ with a well-controlled sample temperature, similar to the results of Lipson et al.[11] and Weil.[12]

Fizeau fringes are produced by interference of the two beams reflected from the almost parallel sample faces, and the Twyman-Green fringes are found by the interference of the two beams reflected from the fixed mirrors. As the sample is heated, both the Twyman-Green and Fizeau fringes move across the aperture as a result of the changing optical

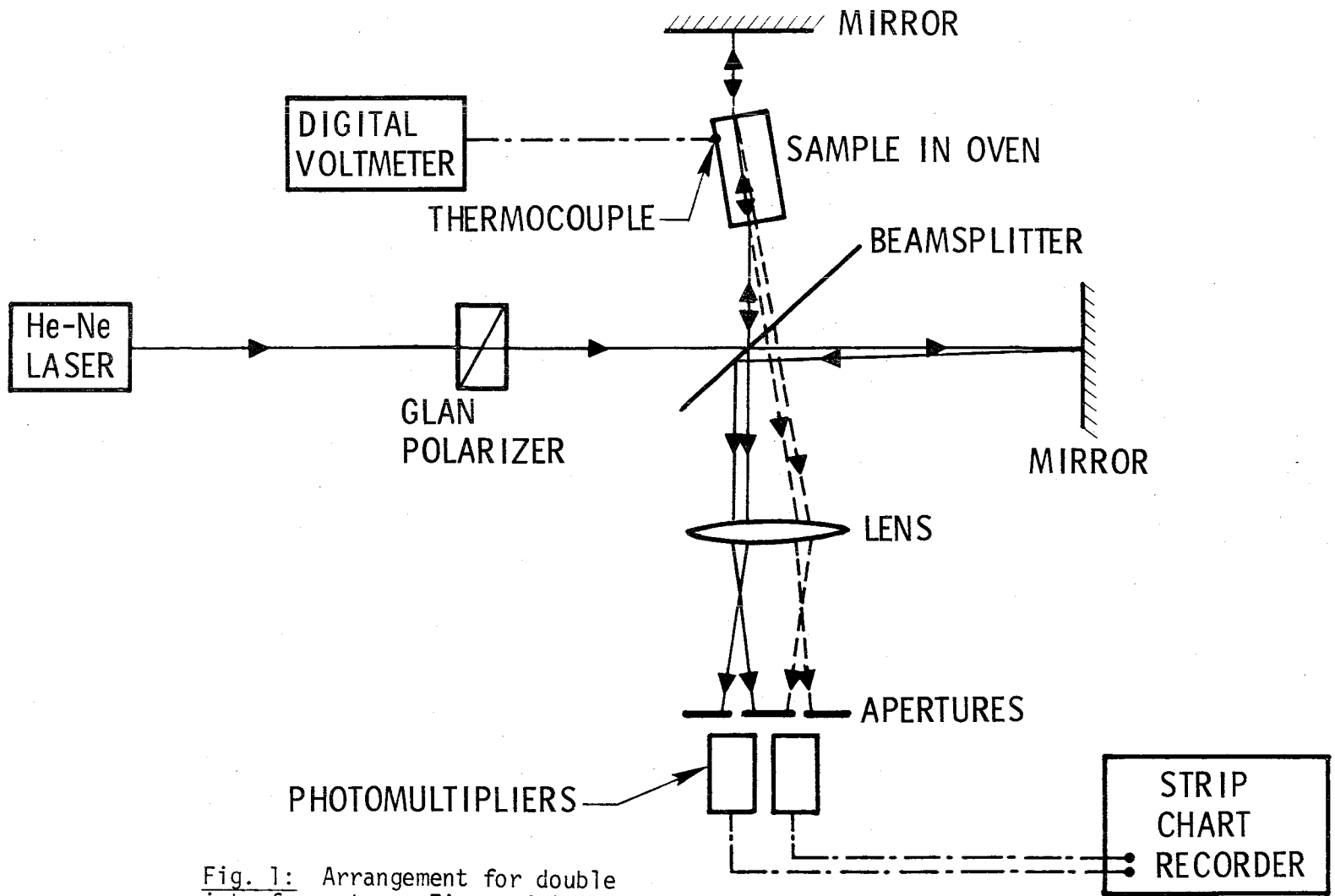

Fig. 1: Arrangement for double interferometer. Fizeau fringes are produced by beams (dashed lines) reflected from sample faces, and Twyman-Green fringes are produced by beams (solid lines) reflected from the fixed mirrors.

path length in the sample. Even though both fringe patterns are functions of α_ℓ and α_n, the Fizeau and Twyman-Green fringe patterns change with temperature at different rates. Then α_ℓ and α_n can be determined from measurement of these two fringe rates.

For the Fizeau interference pattern, the intensity is given by the superposition of the beams reflected from the entrance and exit faces of the sample (see Fig. 2). Including the π phase jump for the internally reflected beam, the combined field amplitude is

$$E = r + r\, e^{-i(2nk\ell + \pi)} \tag{1}$$

where $k = 2\pi/\lambda$ and r is the Fresnel reflection coefficient $(n-1)/(n+1)$. The intensity is

$$I = EE^* = 4r^2 \sin^2 nk\ell. \tag{2}$$

The phase change with temperature is

$$d\delta/dT = 2nk\ell\ (\alpha_n + \alpha_\ell). \tag{3}$$

Define ΔT_F as the temperature difference between two maximum intensity values at a particular point in the Fizeau interference pattern. Then

$$\frac{2\pi}{\Delta T_F} = 2nk\ell\ (\alpha_n + \alpha_\ell)$$

or,

$$\Delta T_F = \frac{\lambda}{2n\ell}\ \frac{1}{(\alpha_n + \alpha_\ell)}\ . \tag{4}$$

ΔT_F is measured by the experiment, where the order of magnitude of ΔT_F is 1°C since $(\lambda/2n\ell) \simeq 10^{-5}$ and $(\alpha_n + \alpha_\ell) \simeq 10^{-5}/°C$.

Now, for the Twyman-Green interference pattern, the intensity is given by the superposition of the beams reflected from the two mirrors in a Twyman-Green arrangement (see Fig. 3). Assuming that the mirror reflectivity is near unity, the combined field amplitude is

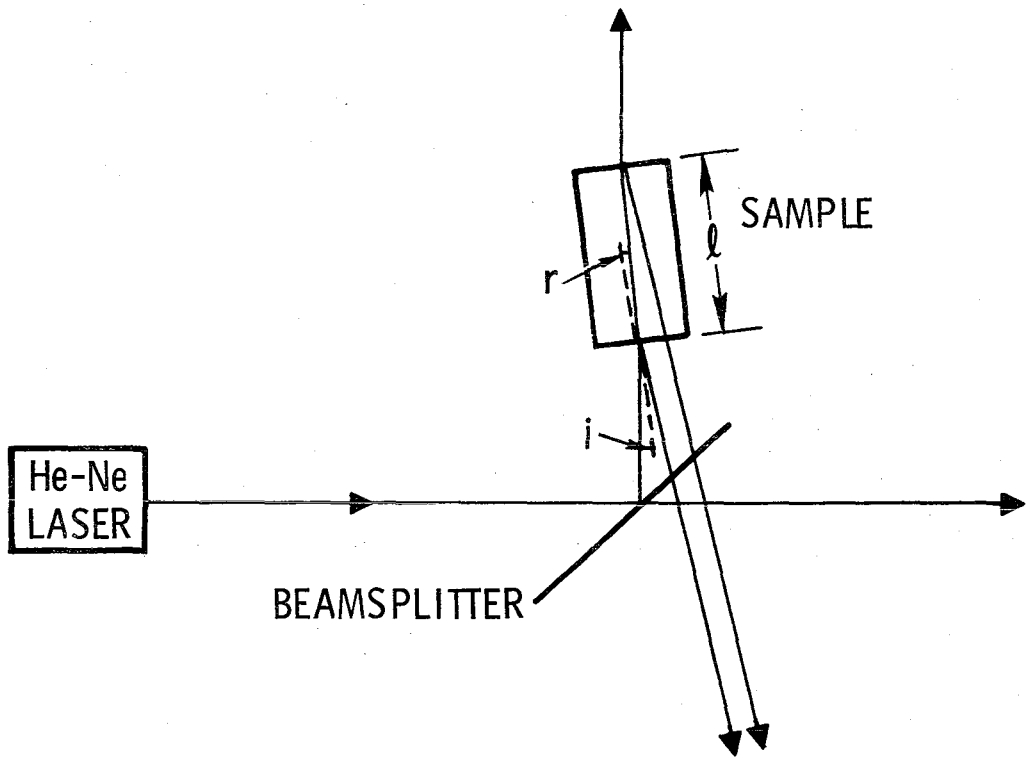

Fig. 2: Fizeau Interferometer Arrangement.

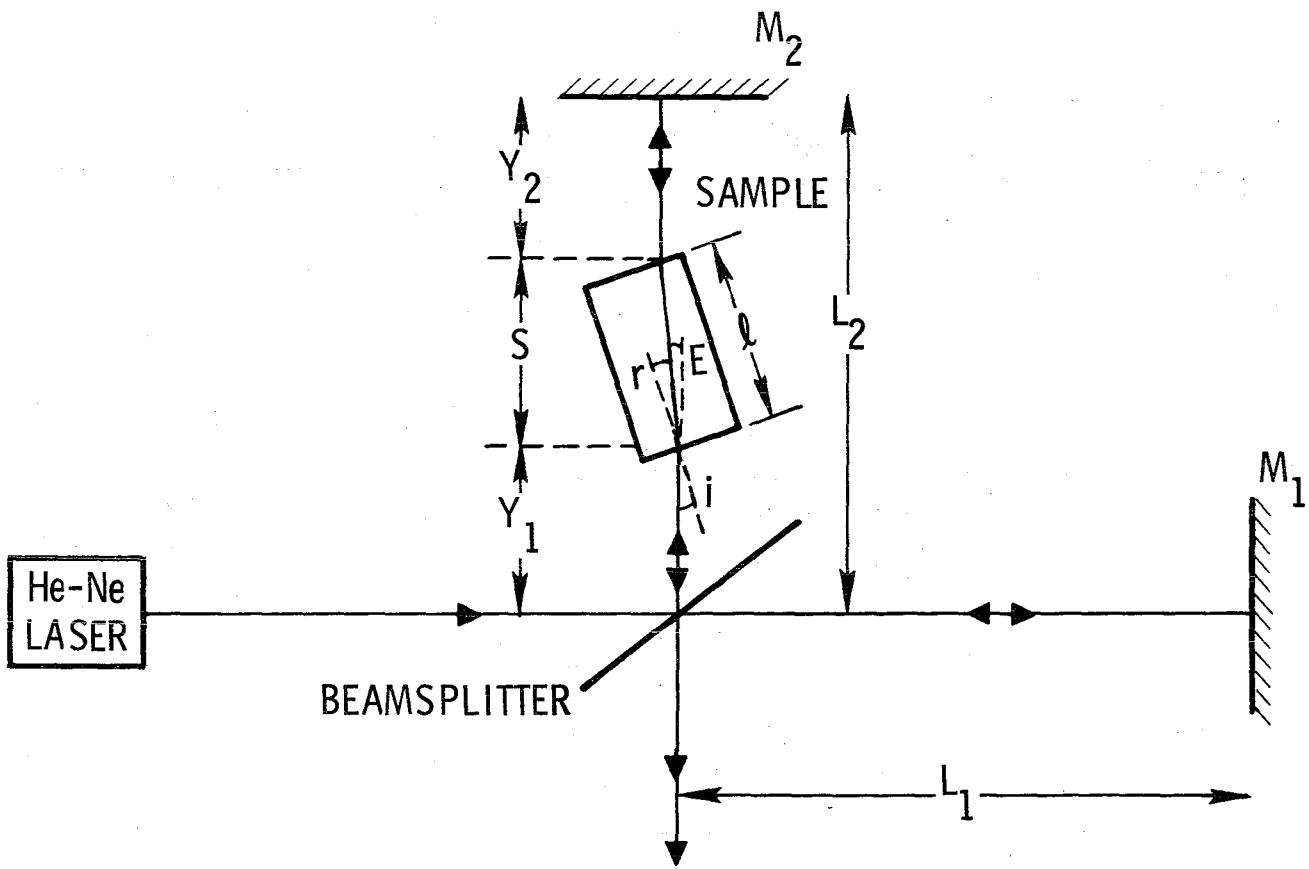

Fig. 3: Twyman-Green Interferometer with the samples at a slight tilt to avoid overlap of the Fizeau and Twyman-Green patterns.

$$E = e^{-i2kL_1} + e^{-i2kn\ell}\, e^{-i2k(L_2-\ell)}$$

$$= 1 + e^{-i2k\Delta L}\, e^{-i2k(n-1)\ell} \tag{5}$$

where $\Delta L = L_2 - L_1$. The intensity is

$$I = 4\cos^2\left[k\ell(n-1 + \frac{\Delta L}{\ell})\right]. \tag{6}$$

For fixed mirrors where the ambient mirror vibrations are small, $\Delta L << \ell$, the $\Delta L/\ell$ phase term can be neglected. The phase change with temperature is

$$d\delta/dT = 2kn\ell\left[(\frac{n-1}{n})\alpha_\ell + \alpha_n\right] \tag{7}$$

Define T_T as the temperature period for the Twyman-Green interference pattern.

$$\Delta T_T = \frac{\lambda}{2n\ell}\left[(\frac{n-1}{n})\alpha_\ell + \alpha_n\right]^{-1} \tag{8}$$

ΔT_T is also measured by experiment and is larger than ΔT_F for positive α_n since the factor $(n-1)/n$ ranges from 1/3 to 1/2. When α_n is negative, both ΔT_F and ΔT_T can be positive or negative with the magnitude of ΔT_F greater than ΔT_T a possibility.

Therefore, the two unknowns α_n and α_ℓ can be determined by measurement of the two temperature periods ΔT_F and ΔT_T and solving simultaneously the two equations (4) and (8). ΔT_F and ΔT_T are different due to the factor $(n-1)/n$. This factor arises from the fact that the sample fills the Twyman-Green interferometer path by varying fractions dependent on temperature ($\propto n-1$) while for the Fizeau interferometer the sample always fills the entire path ($\propto n$). The expressions for α_n and α_ℓ are:

$$\alpha_n = \frac{\lambda}{2\ell}\left(\frac{1}{\Delta T_T} - \frac{(n-1)}{n}\frac{1}{\Delta T_F}\right) \tag{9}$$

and,

$$\alpha_\ell = \frac{\lambda}{2\ell}\left(\frac{1}{\Delta T_F} - \frac{1}{\Delta T_T}\right). \tag{10}$$

Note that Eq. (9), which determines α_n, requires knowledge of the refractive index n at the wavelength λ, while Eq. (10) for α_ℓ does not require any extra information.

Another approach to the solution of the simultaneous equations (4) and (8), as given by Cabezas et al.,[10] is that the ratio α_n/α_ℓ is very accurately determined by this double interferometry, independent of temperature calibration, whereas the individual coefficients depend critically on the temperature measurements. By dividing Eq. (8) by Eq. (4), the ratio of coefficients is determined to be

$$\alpha_n/\alpha_\ell = \frac{(\frac{n-1}{n})\ (\Delta T_T/\Delta T_F) - 1}{1 - (\Delta T_T/\Delta T_F)} \quad . \tag{11}$$

This Eq. (11) can be represented by two hyperbolas with asymptotes at $\Delta T_T/\Delta T_F = 1$ and $\alpha_n/\alpha_\ell = -(n-1)/n$. Experimental error can be evaluated easily from these hyperbolas, the greatest error occurring for values near the asymptotes. There is no double-valuedness in the solution, but there is ambiguity in the sign of $\Delta T_T/\Delta T_F$ which can cause some confusion if not handled carefully. For example, the ratio $\Delta T_T/\Delta T_F$ is positive when either both ΔT_T and ΔT_F are positive or both are negative.

The refractive indices necessary for the double-interferometry analysis were taken from previous work. The index values are determined from the Sellmeier equation

$$n^2 = 1 + A\lambda^2/(\lambda^2 - B) \tag{12}$$

where the Sellmeier coefficients A and B are listed in Table 2. The Sellmeier coefficients for YAG were determined by Wang[13] from his refractive index measurements, and agreed with the measurements of Bond.[14] For BeL, the values of refractive indices were taken from

Material	A	B (μm^2)
Nd:YAG	2.2779	0.01142
Nd:BeL		
n_x	2.7990	0.01875
n_y	2.9268	0.01918
n_z	3.0725	0.01950
Ruby		
n_o	2.06182	0.00943
n_e	2.04483	0.00865
Nd:YALO		
n_x	2.70852	0.013017
n_y	2.67542	0.012805
n_z	2.62507	0.012322

Table 2. Sellmeier coefficients for several solid-state laser crystals

Jenssen et al.[15] who reported n_x, n_y, n_z (x,y,z correspond to the three crystallographic directions) from 0.6 to 2.0 μm. These data were fit to three Sellmeier equations resulting in the tabulated coefficients. Also the previously published data[8] for ruby were fit by the least-squares method to the Sellmeier equation giving the coefficients in Table 2. The Sellmeier coefficients for $YA\ell O_3$ were determined by Martin and DeShazer.[16] With these Sellmeier coefficients the indices of refraction were computed for each wavelength used in the interferometer.

2. Experiment

The two interferometers were formed by the optically flat front and back faces of the sample (Fizeau interferometer) and the two dielectric reflectors (Twyman-Green interferometer) as shown in Fig. 1. When anisotropic samples were investigated, a Glan-Thompson polarizer was placed in front of the light source. Depolarization by the beamsplitter was very low but nevertheless was eliminated by orienting the polarization of the incident beam such that a null was obtained for crossed polarizers located before and after the beamsplitter.

The fringe patterns from the two interferometers were magnified by a lens and projected onto a screen with two circular apertures with diameters much less than the projected fringe spacing. The thermal motion of the fringes across the apertures was detected by two S-11 photomultipliers and simultaneously recorded by a dual-pen strip chart recorder (Hewlett-Packard model 7100 BM). Mechanical shocks were minimized by mounting the interferometer assembly on a Gaertner optical bench.

The samples were heated in a vacuum oven (Fig. 4). A nichrome heater coil was wrapped around a solid copper cylinder (26 mm dia x 48 mm height) which held the samples in a hole drilled through the cylinder. The heater coil was connected to a variac power supply and the samples were heated by conduction from the copper cylinder. Long samples (76 mm) were wrapped in copper foil to reduce thermal gradients in the samples while the short samples (10 mm) were placed in a glass sleeve to minimize shifting and vibrations during the heating cycle.

The oven was evacuated to 10^{-5} Torr pressure to eliminate thermal change of the refractive index of the air and heating of the fused silica windows by air convection. The windows were not heated by conduction since the copper cylinder was insulated from the brass housing of the oven. The top trace of Fig. 5 shows the motion of the Twyman-Green fringes due to heating of the air in the oven without a sample. By Eq. (9) with λ = 6328 Å, n = 1, T_T = 2.81°C and ℓ = 11 cm (the distance between the fused silica windows), dn/dT for air was determined to be -1.02×10^{-6}/°C which is in good agreement with the value -0.91×10^{-6}/°C given by the International Critical Tables,[17] considering the uncertainty in the H_2O and CO_2 content in our air. The bottom trace of Fig. 5 shows that there was no motion of the Twyman-Green fringes for an evacuated oven indicating that there was no heating of the windows by conduction and thermal radiation.

The sample temperature was measured by a chromel-alumel thermocouple using an "Omega" cold-junction compensator. The thermocouple was calibrated by immersing the copper cylinder and thermocouple in water at four temperatures (1°, 20°, 28°, 63°C). The measured emf/°C was 40.8 μV/°C as determined by a least-squares fit (see Fig. 6). This measurement compares very well with the accepted value[18] of 40 μV/°C for chromel-alumel

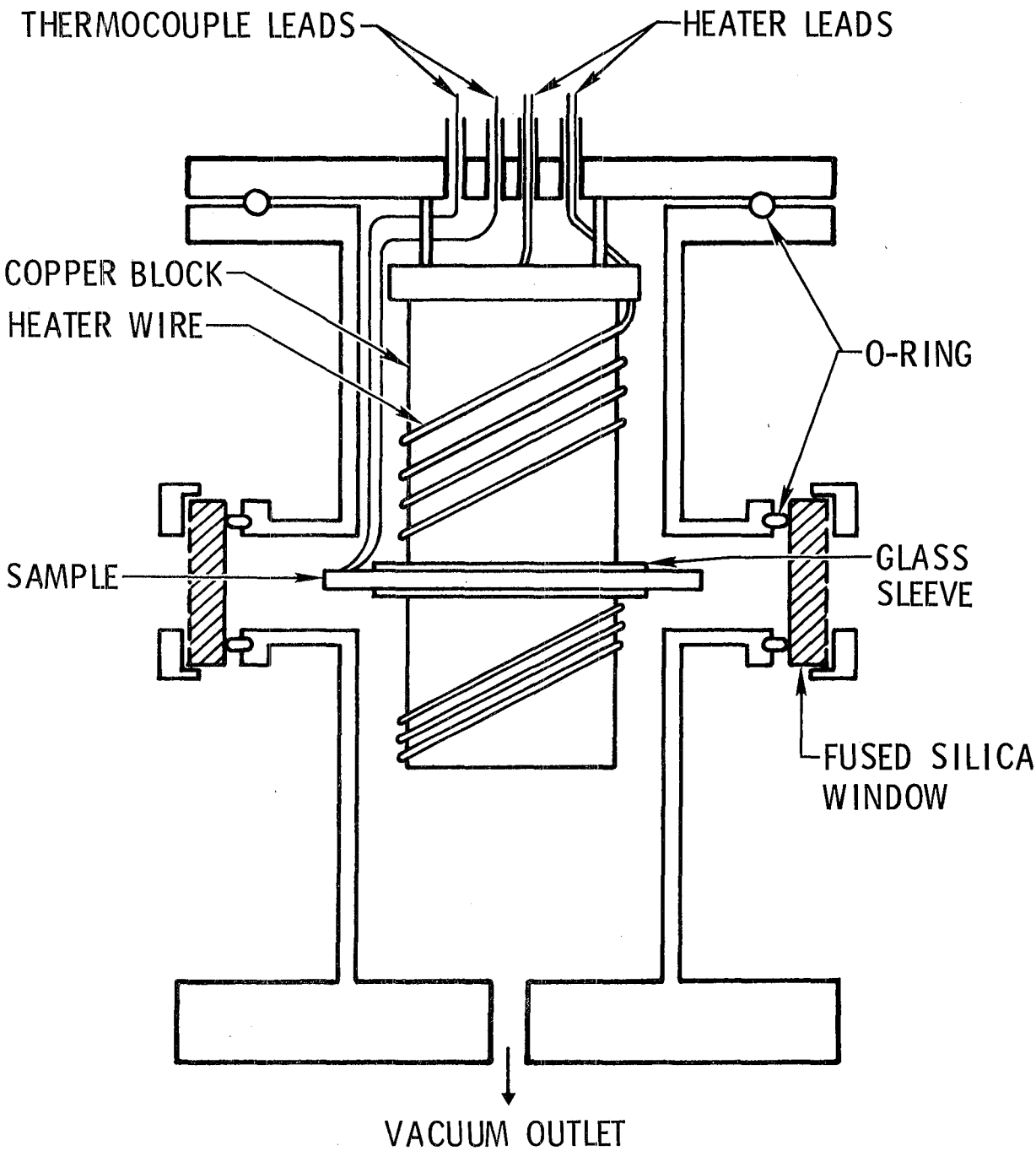

Fig. 4: Vacuum Oven for Heating Samples.

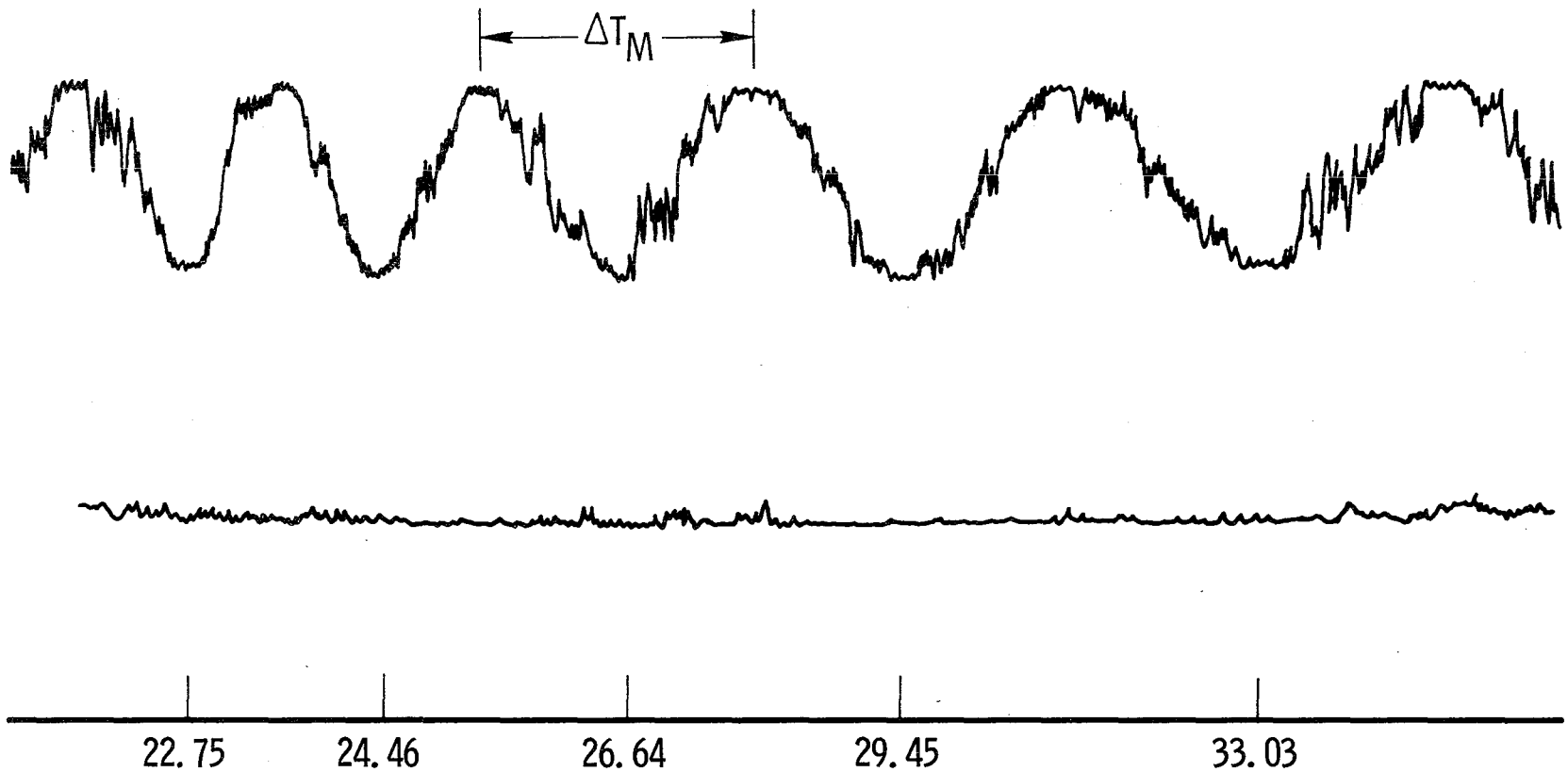

Fig. 5: Twyman-Green fringe motion (top trace) due to heating of the air in oven without a sample (ΔT_T = 2.81°C). Bottom trace demonstrates that there is no fringe motion when oven is evacuated.

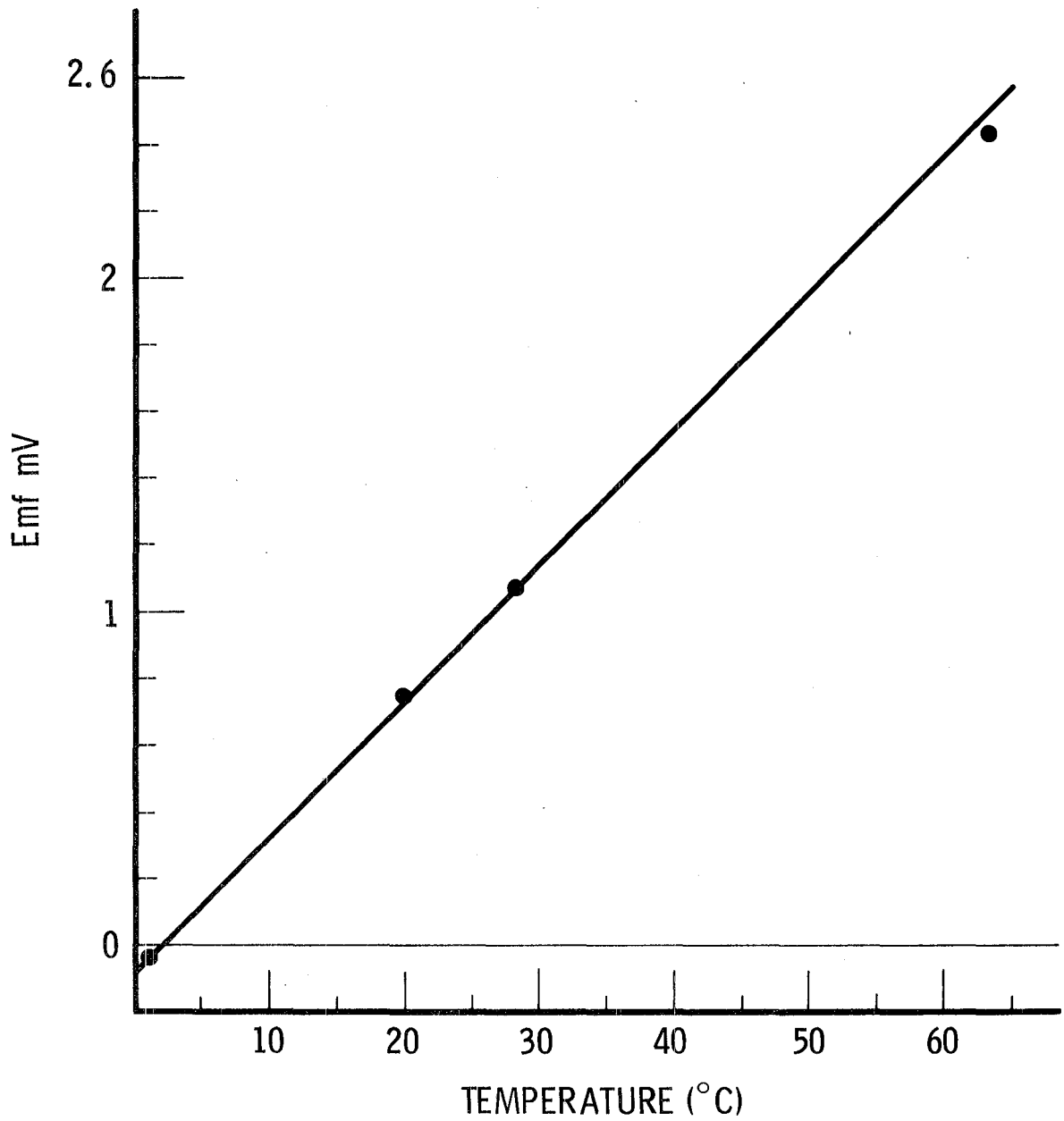

Fig. 6: EMF vs temperature for chromel-alumel thermocouple.

thermocouples. Good thermal contact between the thermocouple and sample was achieved by holding them together with a few turns of Teflon tape. A typical temporal increase in temperature of a YAG sample is shown in Fig. 7. Initially the temperature rise is non-uniform but after about a 6°C increase, the temperature rises linearly with time. Having this linear change with a constant $\Delta T/\Delta t$ allowed the measurement of fringe motion with temperature to be given simply as fringe motion in time.

The Nd:YAG crystal studied was a laser rod (6.34 mm dia x 76.5 mm long) with nominal 1.0 at. % Nd doping. A YAG rod, undoped and 8.13 cm long, was also studied. Two Nd:BeL rods (5 mm dia x 12.7 mm long) with x-axis and y-axis orientation were investigated. Three Nd:YALO laser rods (a,b,c axes) used in our investigation had dimensions 5 mm dia x 50 mm length and were donated by Union Carbide Corp. The Nd laser glass was Kodak glass with 1% Nd and dimensions of 6.4 mm dia x 44.5 mm. The 0° ruby laser rod (6.34 mm dia x 76.5 mm) had Cr concentration of 0.04 at. % and was purchased from Adolf Meller Co. The 60° ruby laser rod (6.34 mm dia x 76.5 mm) had 0.05 at. % of Cr^{3+} and was purchased from Union Carbide Corp.

The light sources for the interferometry system were a He-Ne laser (Spectra-Physics model 133), an argon-ion laser (Coherent Radiation model CR3) and a Nd:YAG laser (GTE Sylvania model 605).

3. Results

The coefficients of linear thermal expansion were measured for four crystals and a Nd glass over the temperature interval 30-60°C and are listed in Table 3. The value of α_ℓ is independent of the light wavelength used in its interferometric measurement; any observed wavelength

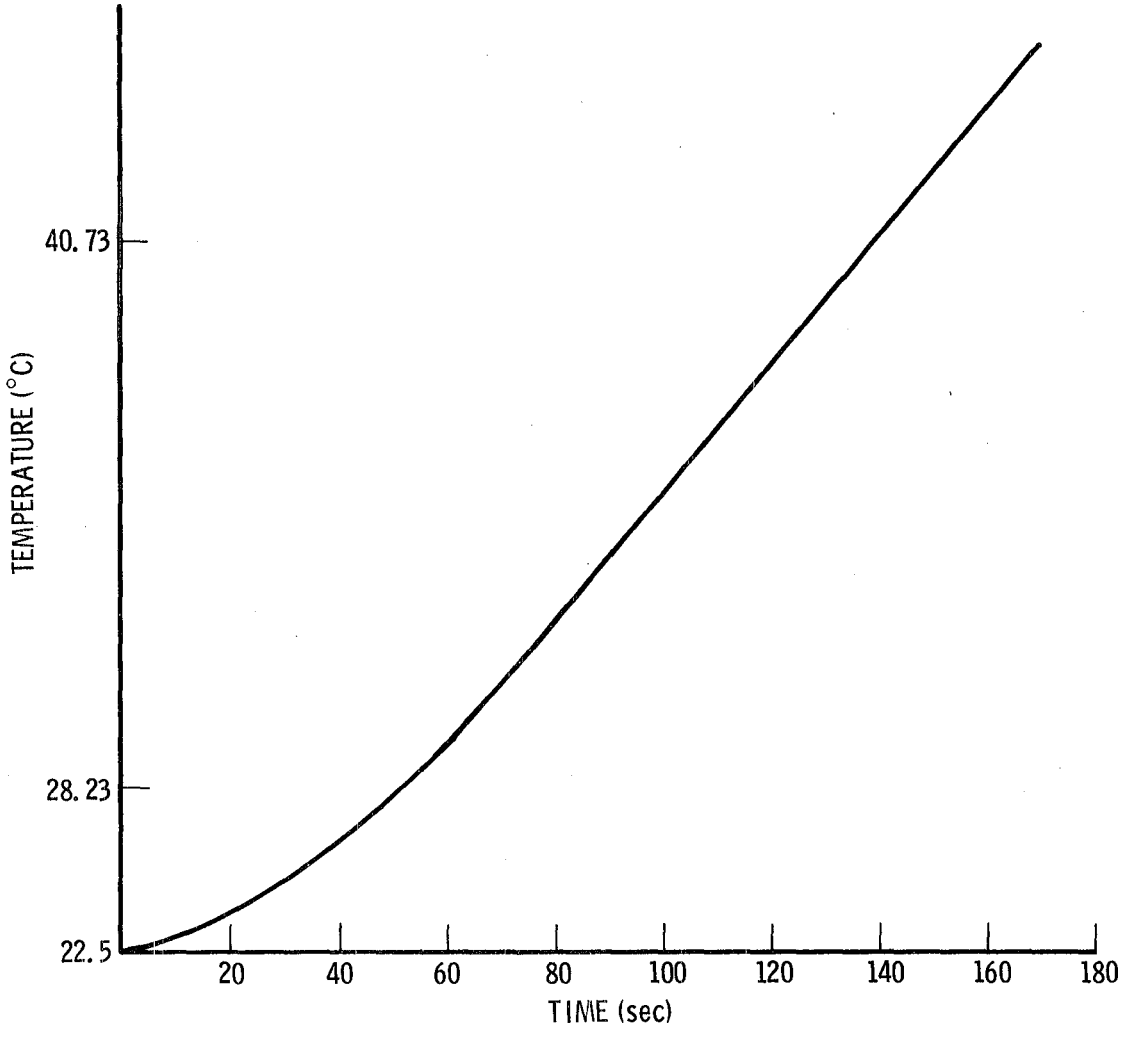

Fig. 7: Temperature of YAG sample vs. time showing linear temperature rise after the initial 6°C increase.

Sample	α_ℓ ($\times 10^{-6}$/°C)
YAG:Nd	7.04 ± 0.14
BeL:Nd	
x-axis	11.53 ± 0.14
y-axis	11.63 ± 0.70
YALO:Nd, Cr	
a-axis	9.62 ± 0.25
b-axis	3.73 ± 0.57
c-axis	10.01 ± 0.33
Kodak glass:Nd	13.30 ± 0.27
Ruby	
0°	6.90 ± 0.18
60°	5.71 ± 0.38

Table 3. Linear thermal expansion coefficients α_ℓ measured over the temperature interval 30-60°C

differences in α_ℓ will be indicative of the experimental error. Table 4 lists measured α_ℓ of YAG for seven wavelengths with values from 6.88 to 7.21 x $10^{-6}/^{o}C$ having an average of 7.04 $\pm$ 0.14 x $10^{-6}/°C$, a $\pm$2% error. Undoped YAG was used for this measurement since fringe visibility was lower for Nd:YAG due to the absorption of the laser light by Nd. There was no change observed in α_ℓ for Nd:YAG but the error was greater.

Figure 8 shows the fringe motion with increasing temperature for the Nd:YAG laser rod at 6328 Å. Notice that the Fizeau fringe motion is 44% greater than the Twyman-Green fringe motion, a consequence of α_n being positive for YAG. The slight fluctuations in the peak intensities of the fringes is due to a slow variation in the output intensity of the He-Ne laser. Figure 9 shows that the Fizeau fringe motion for Nd:YAG using the 4965 Å line of an argon-ion laser is about 33% greater than the Fizeau fringe motion at 6328 Å, indicating α_n for YAG increases towards the UV. Table 5 lists the refractive indices, the thermo-optic coefficients α_n and dn/dT for YAG at eight wavelengths.

The plot of Eq. (11) for YAG at 6328 Å is the solid curve given in Fig. 10. The triangles indicate the YAG data with the open triangle representing the data of Sylvania[1] which is significantly lower than the value obtained in this work, the black triangle. This discrepancy between Sylvania and ourselves cannot be due to possible variations in Nd doping since we could not observe any differences in α_n and α_ℓ between doped and undoped YAG. We conjecture that the discrepancy is due to strain-induced refractive-index changes in the Sylvania experiment caused by their bonding of silica flats onto the YAG rod with epoxy.

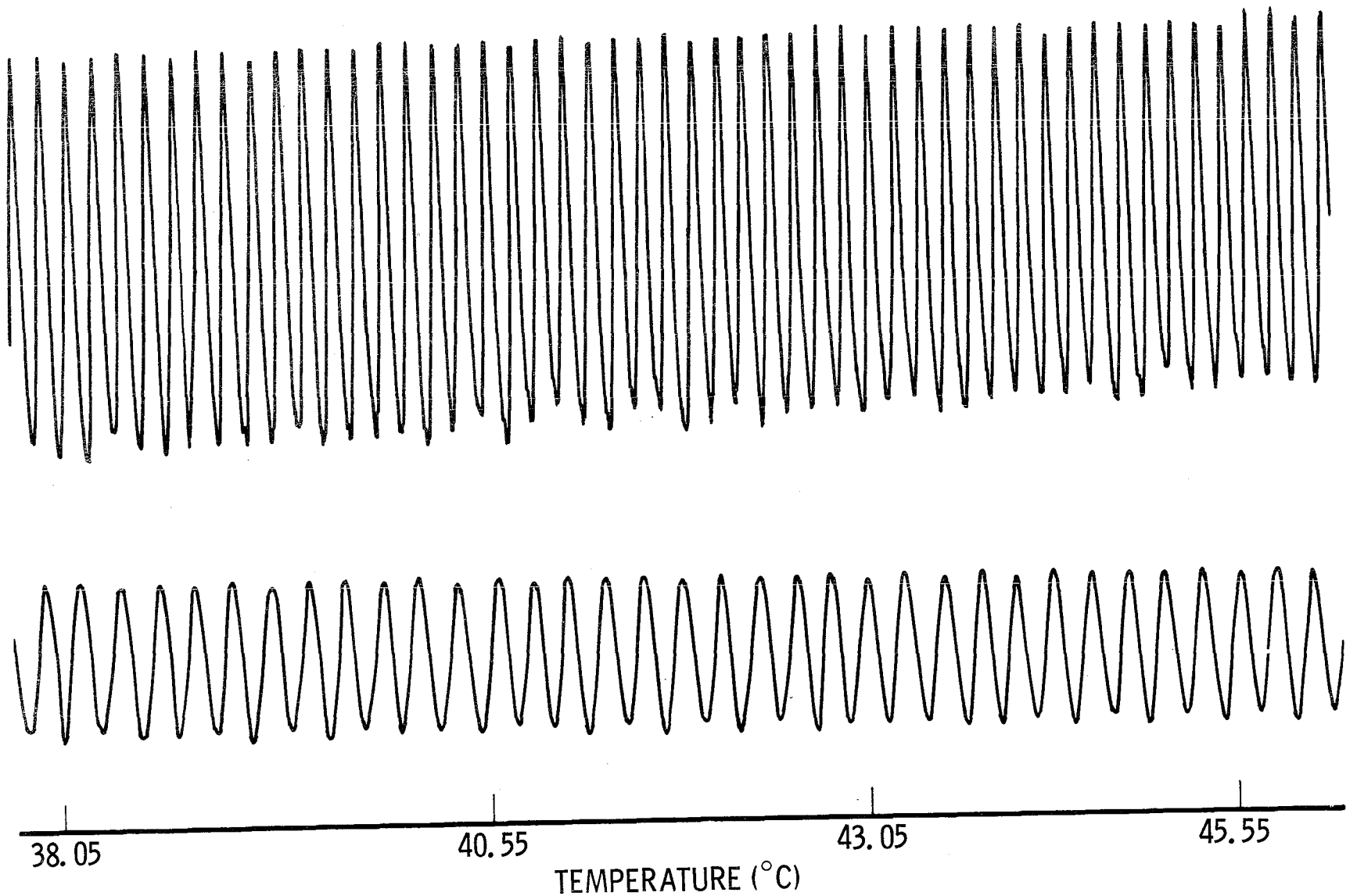

Fig. 8: Thermal fringe motion o for Nd^{3+}:YAG (7.65 cm) at 6328 A. Top trace is for Fizeau fringe motion and bottom trace is for Twyman-Green fringe motion.

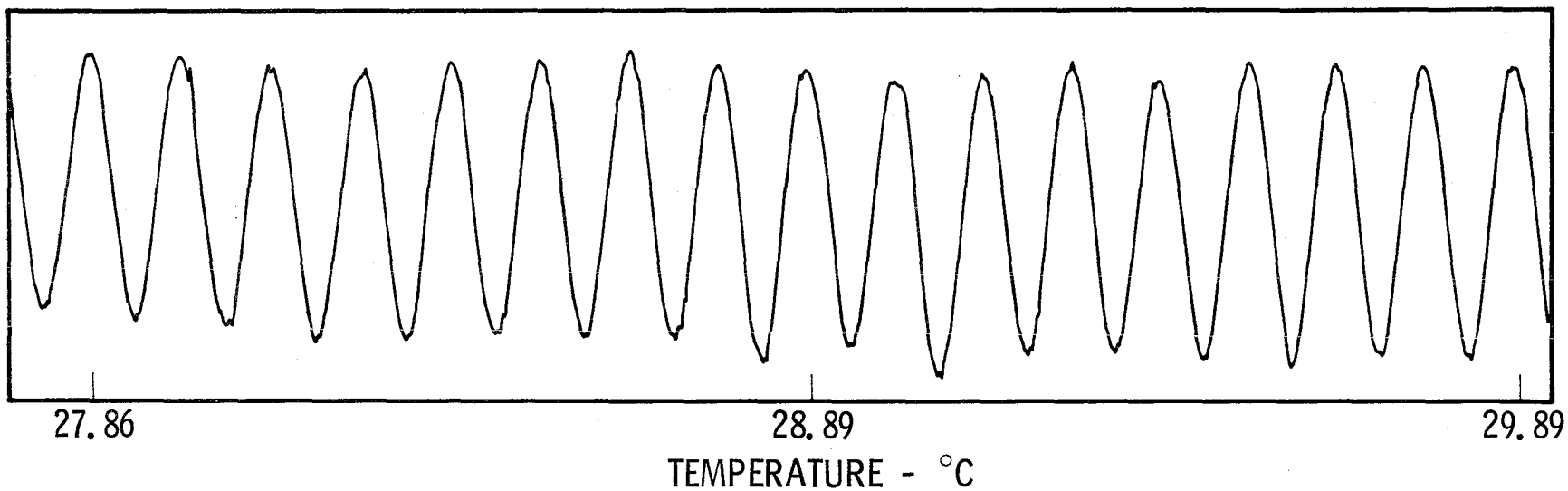

Fig. 9: Fizeau fringe motion for Nd:YAG at 4965 Å.

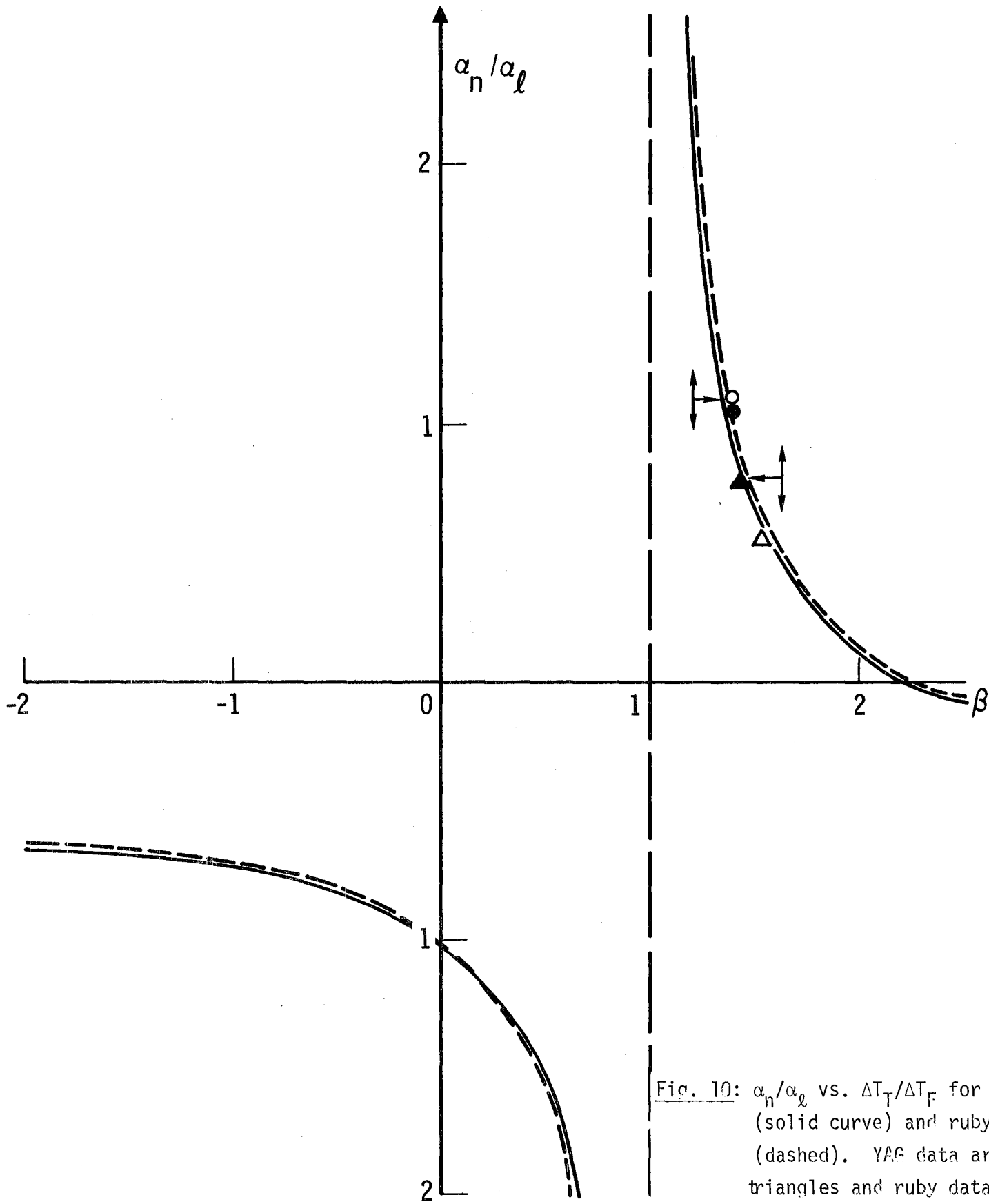

Fig. 10: α_n/α_ℓ vs. $\Delta T_T/\Delta T_F$ for YAG (solid curve) and ruby (dashed). YAG data are triangles and ruby data circles.

λ (μm)	ΔT_F (°C)	ΔT_T (°C)	α_ℓ (10^6/°C)
0.4579	0.1146	0.1591	6.87
0.4765	0.1185	0.1643	6.90
0.4880	0.1218	0.1707	7.07
0.4965	0.1245	0.1757	7.14
0.5015	0.1284	0.1799	6.88
0.5145	0.1328	0.1904	7.21
0.6328	0.1656	0.2386	7.19

Table 4. Measured temperature periods ΔT and coefficient of linear expansion α_ℓ for YAG over the interval 30-45°C. Average $\alpha_\ell = 7.04 \pm 0.14 \times 10^{-6}$/°C. Length of sample was 8.13 cm.

λ (μm)	n	α_n (10^{-6}/°C)		dn/dT (10^{-6}/°C)	
		meas.	calc.	meas.	calc.
0.4579	1.8464	6.44	6.477	11.89	11.96
0.4765	1.8435	6.51	6.327	12.00	11.66
0.4880	1.8419	6.30	6.243	11.60	11.50
0.4965	1.8408	6.18	6.176	11.38	11.37
0.5017	1.8402	6.18	6.148	11.37	11.31
0.5145	1.8386	5.75	6.064	10.57	11.15
0.6328	1.8289	5.66	5.567	10.35	10.18
1.0642	1.8169	4.98	4.989	9.05	9.06

Table 5. Thermo-optic coefficients of YAG over the interval 30-45°C. Error for α_n is $\pm$ 0.07 x 10^{-6}/°C and for dn/dT, $\pm$ 0.15 x 10^{-6}/°C.

The wavelength variation of α_n for YAG is shown in Fig. 11 and fitted a single-resonance theoretical model within 2%. The values fitted to the data are listed as "calc" in Table 5. Following the approach of Ramachandran,[19,20] the dispersion of dn/dT originates from the thermal change of oscillator density and the thermal change of resonance frequency of the oscillator. This is easily seen by differentiating the Sellmeier equation, written in terms of frequency, with respect to temperature.

$$n^2 = 1 + \frac{N\, e^2/m\varepsilon_o}{\omega_o^2 - \omega^2} \tag{13}$$

$$2n \frac{dn}{dT} = \frac{1}{N} \frac{dN}{dT} \frac{N\, e^2/m\varepsilon_o}{\omega_o^2 - \omega^2} - \frac{2}{\omega_o} \frac{d\omega_o}{dT} \frac{\omega_o^2}{(\omega_o^2-\omega^2)} \frac{Ne^2/m\varepsilon_o}{(\omega_o^2-\omega^2)} \tag{14}$$

Since N $\propto$ mass/volume, $N^{-1}\, dN/dT = -3\, \alpha_\ell$. Define the coefficient of thermal change of resonance frequency as $\alpha_\omega \equiv \omega_o^{-1} d\omega_o/dT$. Then α_n can be written as

$$\alpha_n = -3\alpha_\ell \frac{(n^2-1)}{2n^2} - \alpha_\omega \frac{\omega_o^2}{(\omega_o^2 - \omega^2)} \frac{(n^2-1)}{n^2} \tag{15}$$

Therefore the thermo-optic coefficient α_n can be separated into a thermal expansion part ($\propto \alpha_\ell$) and an electronic dispersion part ($\propto \alpha_\omega$). Table 6 gives this separation of α_n for YAG. The thermal expansion part α_n^e of α_n was calculated from the measured values of n and α_ℓ and is seen to be negative for a positive α_ℓ. The electronic dispersion part α_n^u was determined by fitting the measured α_n^u ($\equiv \alpha_n(\text{meas}) - \alpha_n^e$) to the equation

$$\frac{1}{\alpha_n^u} \left(\frac{n^2 - 1}{n^2}\right) = \frac{1}{\alpha_\omega} \left(\frac{\lambda_o^2}{\lambda^2} - 1\right) \tag{16}$$

which is a linear equation with the variables

$$\frac{1}{\alpha_n^u} \left(\frac{n^2 - 1}{n^2}\right) \quad \text{and} \quad \frac{1}{\lambda^2}\,.$$

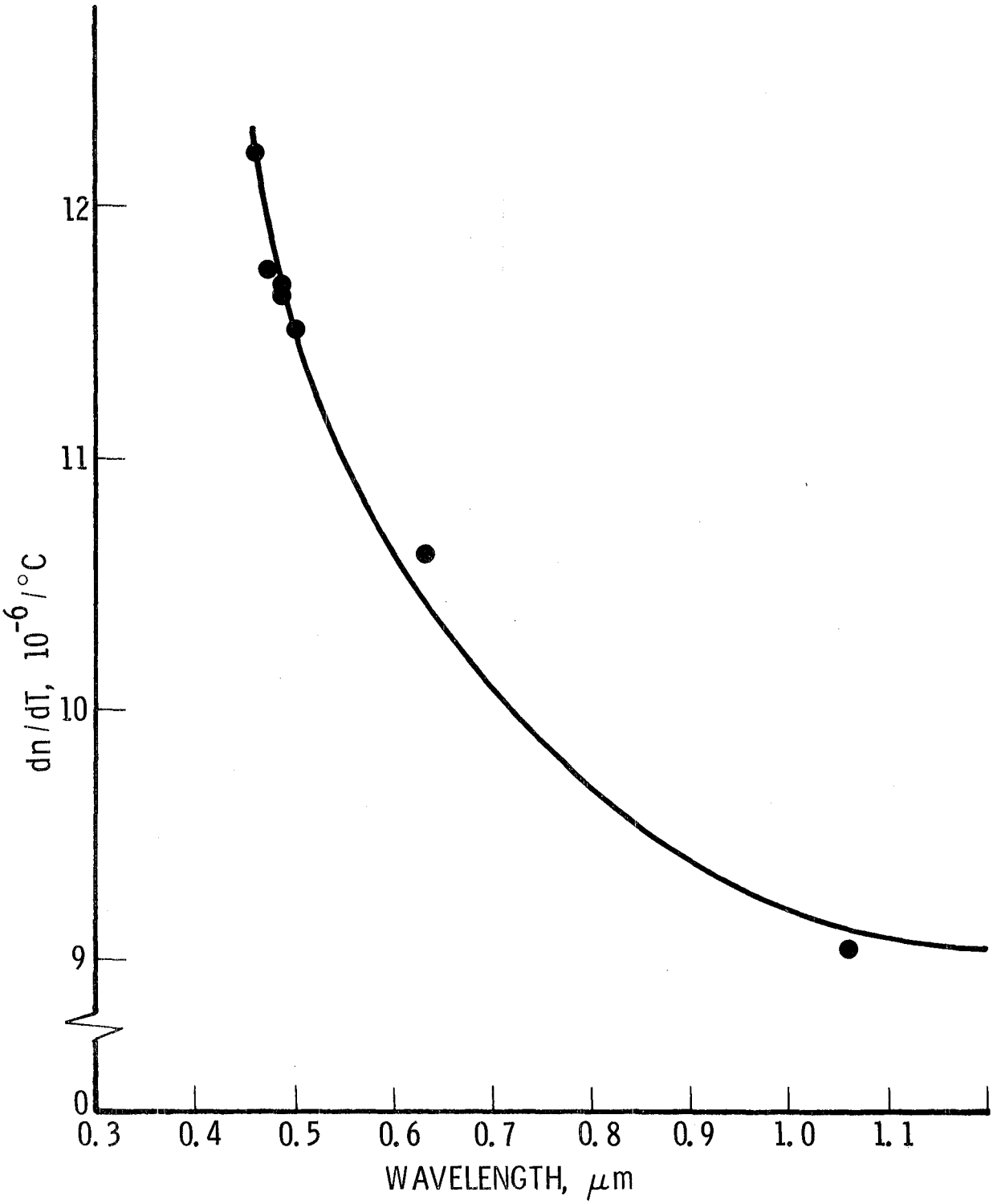

Fig. 11 Dispersion of dn/dT for YAG

λ (μm)	α_n meas. (10^{-6}/°C)	α_n^e calc. (10^{-6}/°C)	α_n^u meas. diff. (10^{-6}/°C)	α_n^u l.s. fit (10^{-6}/°C)
0.4579	6.44	-7.463	13.90	13.94
0.4765	6.51	-7.453	13.96	13.78
0.4880	6.30	-7.447	13.75	13.69
0.4965	6.18	-7.444	13.62	13.62
0.5017	6.18	-7.442	13.62	13.59
0.5145	5.75	-7.436	13.19	13.50
0.6328	5.66	-7.403	13.06	12.97
1.0642	4.98	-7.361	12.34	12.35

Table 6. Separation of the thermo-optic coefficient (α_n) for YAG into its thermal expansion (α_n^e) and electronic dispersion (α_n^u) parts.

Figure 12 shows this linear least-squares fit where the constants are $\alpha_\omega = -17.31 \times 10^{-6}/^{o}C$ and $\lambda_o = 1603.3$ Å, with the standard error of estimate being $\pm 0.15 \times 10^{-6}/^{o}C$.

The thermo-optic coefficients of the biaxial Nd:BeL crystal were measured for the three polarizations $\vec{E} || \hat{x},\hat{y},\hat{z}$ using x- and y-axis rods. The values of dn/dT and α_n at 6328 Å are given in Table 7. Figure 13 shows the fringe motions with increasing temperature for the x-axis rod with polarization $\vec{E} || \hat{Z}$, and Figure 14 shows the fringe motions for the y-axis rod with $\vec{E} || \hat{X}$. More mechanical vibrations occur for short samples such as BeL causing intensity fluctuations in the Twyman-Green fringe pattern. The Fizeau pattern is not susceptible to these fluctuations since sample vibrations do not change the relative spacing and tilt of the reflecting faces. The ratio of α_n/α_ℓ for the BeL samples was lower than than of YAG (see Fig. 15). In the case of the x-axis rod this ratio was negative for both polarizations, E||Z and E||Y, near -0.33. For the y-axis rod the value of α_n/α_ℓ was 0.20 for E||X.

The Fizeau fringe motions for the Nd Kodak glass sample at 5017 Å, 6328 Å and 1.064 μm are shown in Figs. 16, 17 and 18. Table 8 lists the thermo-optic coefficients of this glass at four different wavelengths. Note that for this sample α_n is negative for wavelengths longer than 5000 Å.

The coefficient of thermal expansion and α_n were measured for the 0^{o} ruby crystal (light propagation along crystal axis) at 6328 Å and 1.064 μm (see Figs. 19 and 20). Measurements at the argon-ion laser wavelengths were not possible because of the strong absorption of ruby at these wavelengths. α_ℓ for the 0^{o} ruby was measured to be $6.90 \pm 0.2 \times 10^{-6}/^{o}C$ (expansion along c axis), near the $6.66 \times 10^{-6}/^{o}C$ value quoted in ref. 3. dn/dT for the

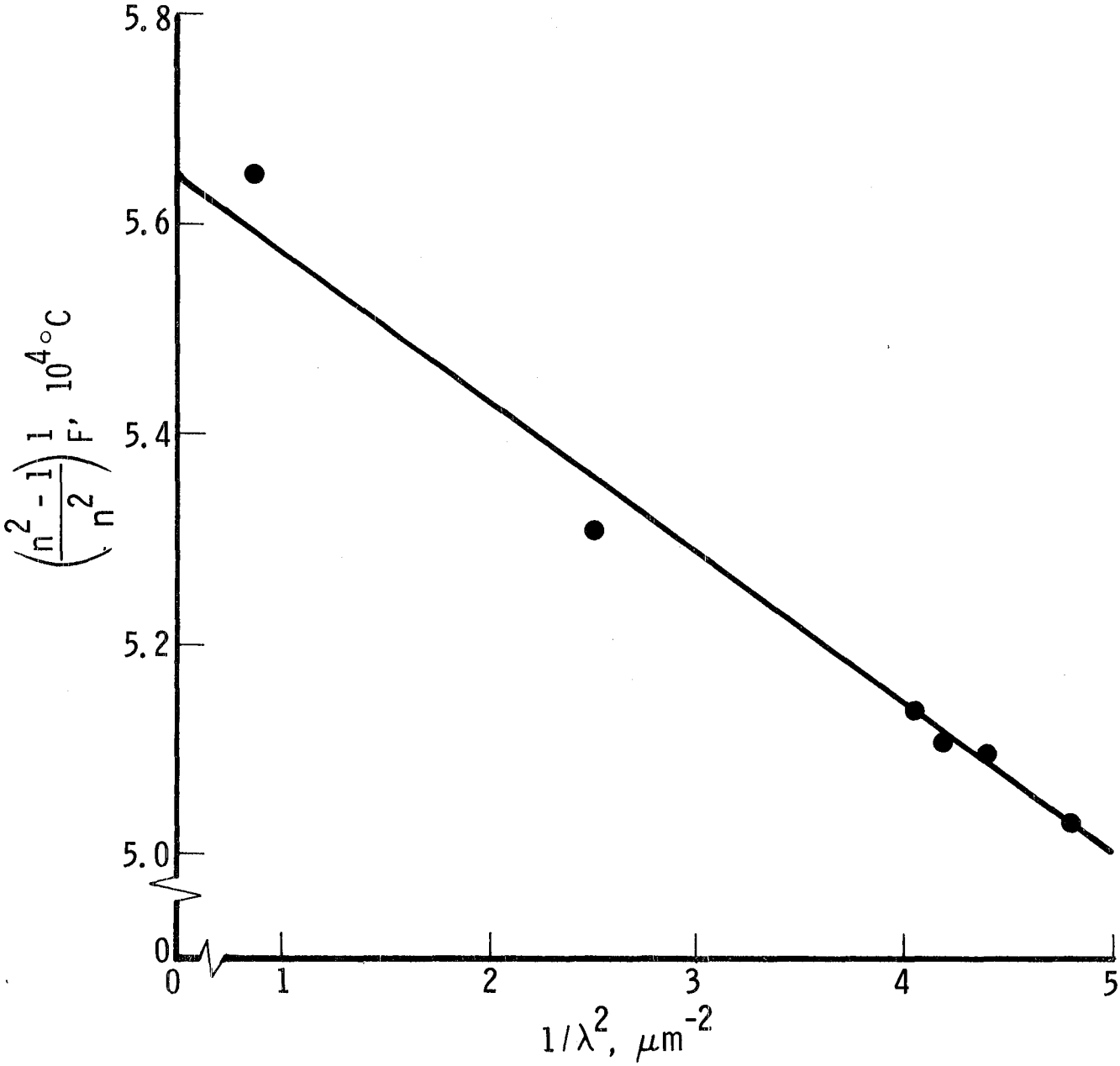

Fig. 12 Plot of $\left(\frac{n^2 - 1}{n^2}\right) \frac{1}{F}$ vs $\frac{1}{\lambda^2}$ where $F = \alpha_n^u$ is the Electronic Dispersion Part of α_n for YAG

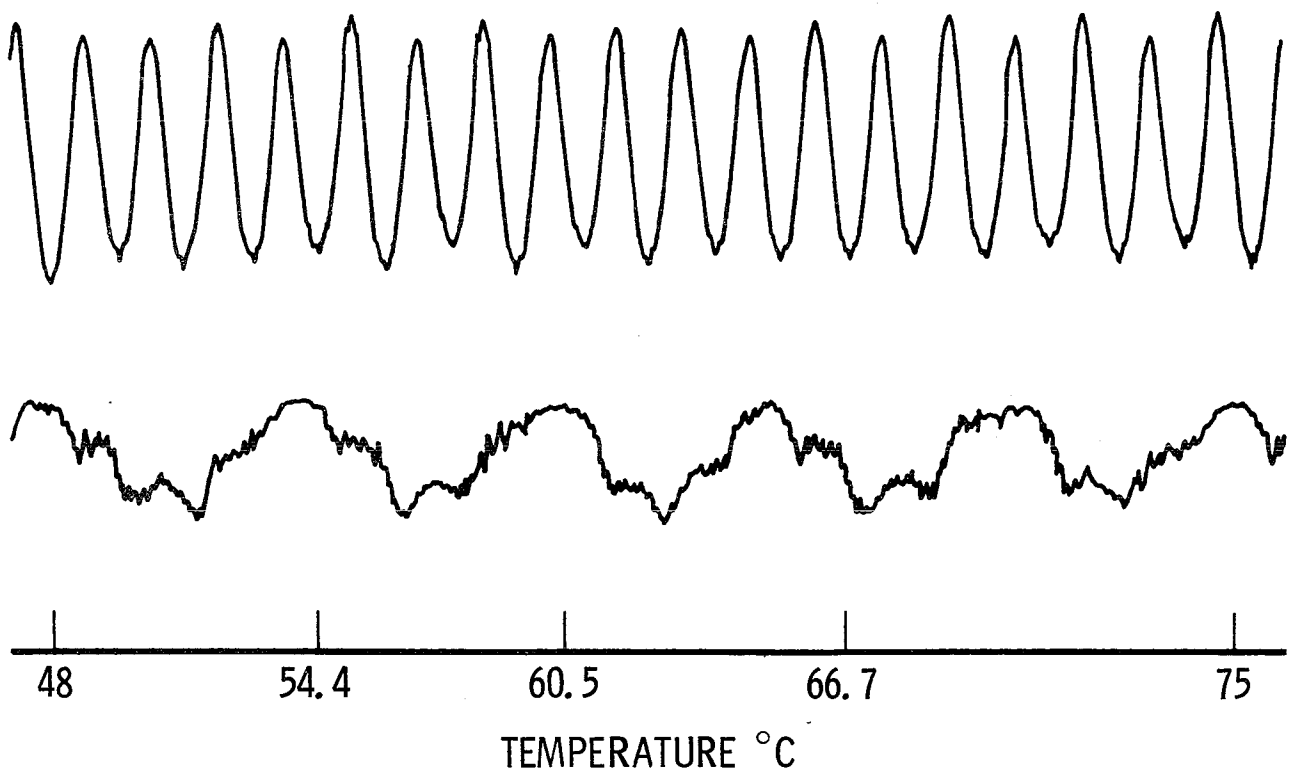

Fig. 13: Fringe motion for Nd:BeL x-axis rod with E||Z at 6328 Å. Top trace is for Fizeau fringe motion and bottom trace is for Twyman-Green fringe motion.

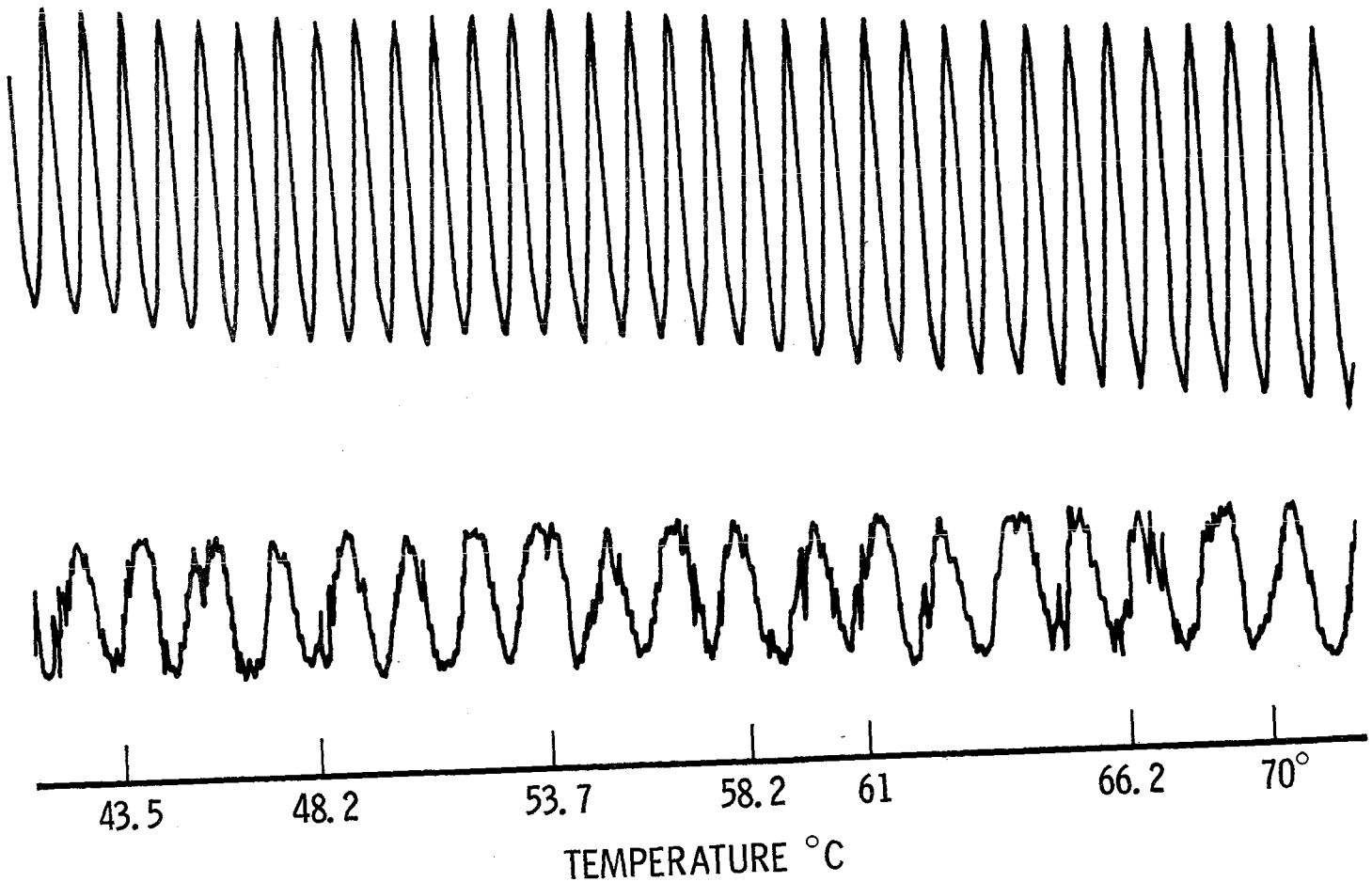

Fig. 14: Fringe motion for Nd:BeL y-axis rod with E||X at 6328 Å. Top trace is Fizeau fringe motion and bottom trace is for Twyman-Green fringe motion.

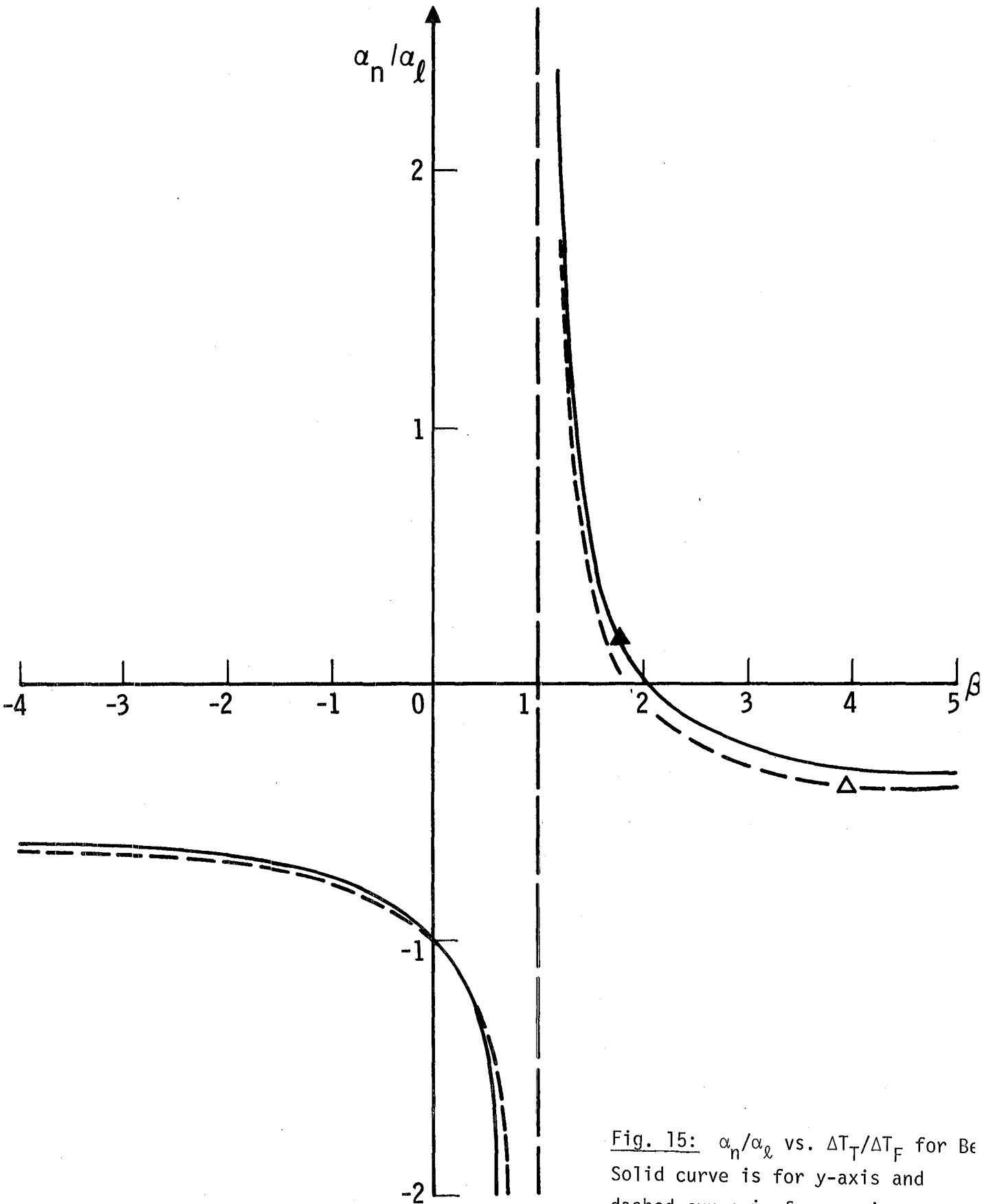

Fig. 15: α_n/α_ℓ vs. $\Delta T_T/\Delta T_F$ for Be
Solid curve is for y-axis and
dashed curve is for x-axis.
Triangles are data points.

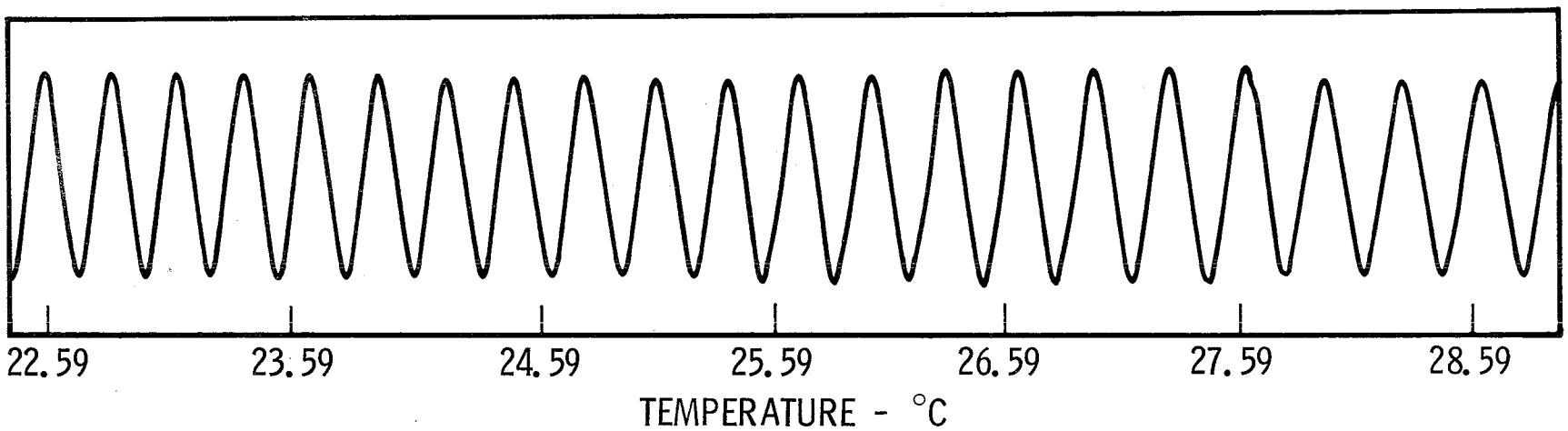

Fig. 16: Fizeau fringe motion for Nd Kodak glass at 5017 Å.

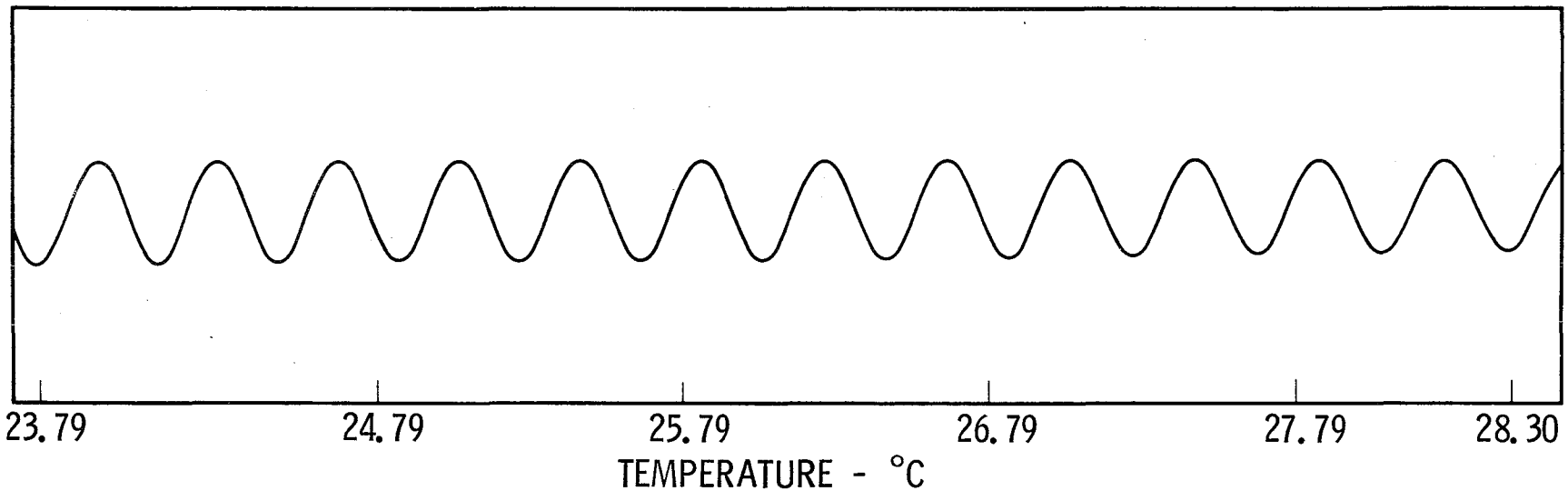

Fig. 17: Fizeau fringe motion for Nd Kodak at 6328 Å.

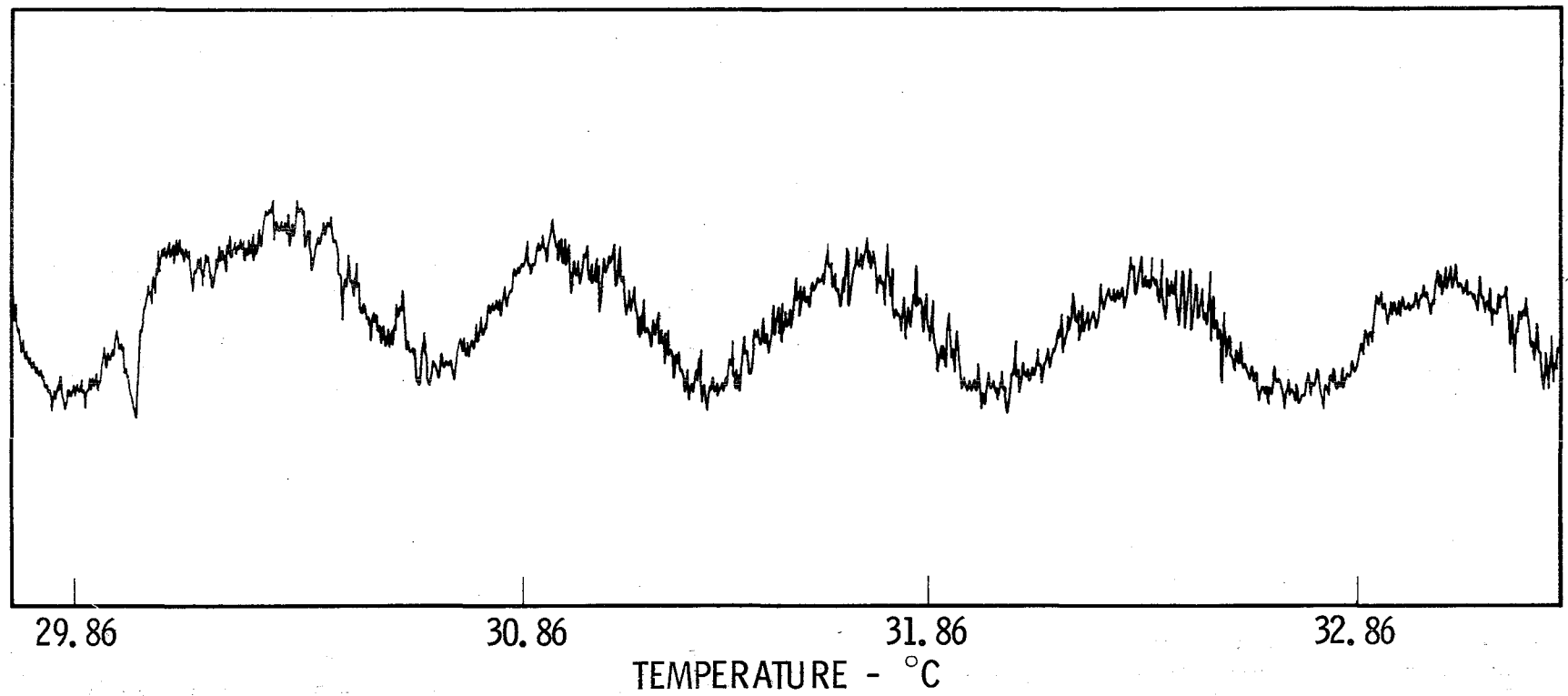

Fig. 18: Fizeau fringe motion for Nd Kodak glass at 1.064 μm

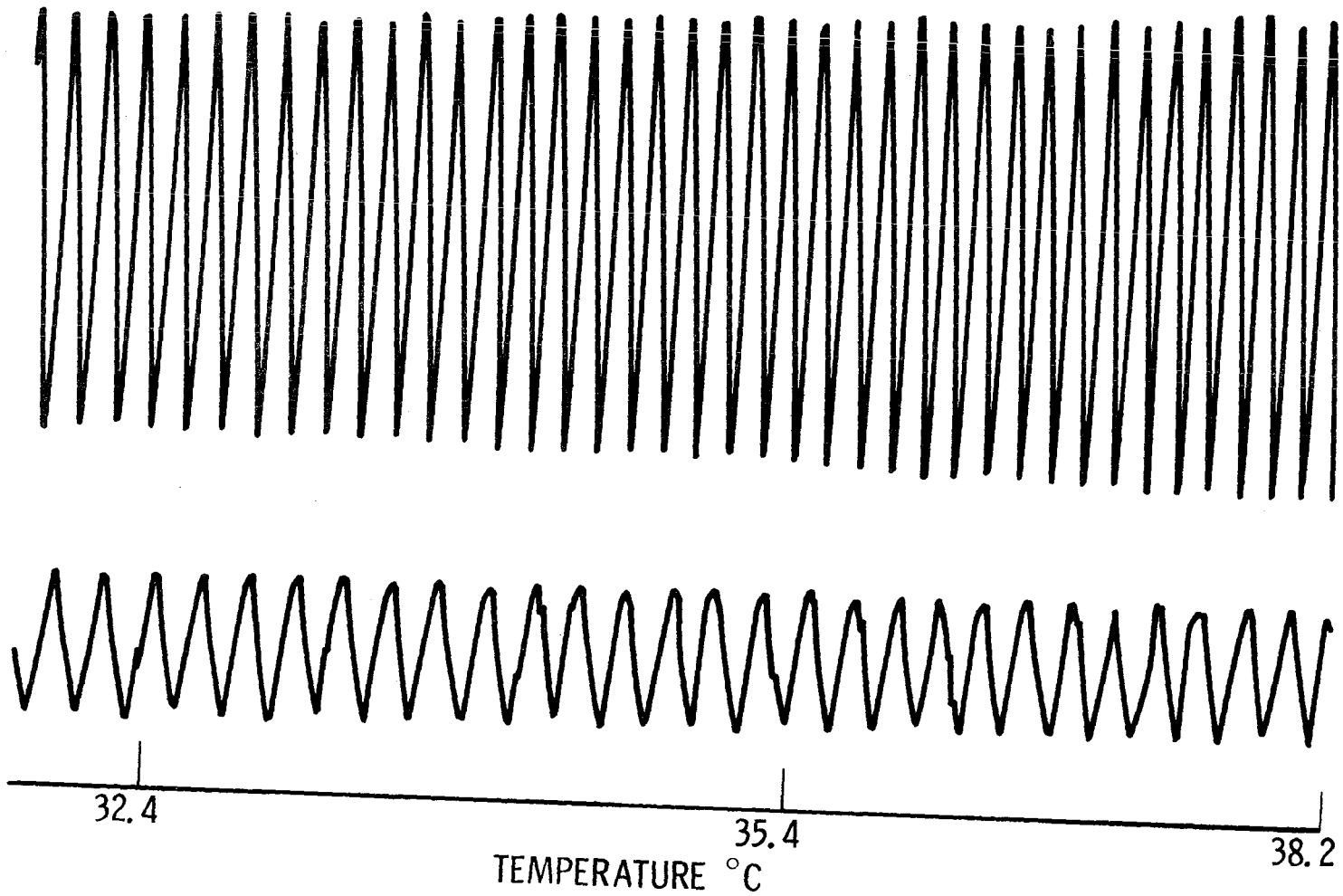

Fig. 19: Fringe motion for 0° ruby at 6328 Å. Top trace is Fizeau fringe motion and bottom trace is Twyman-Green fringe motion.

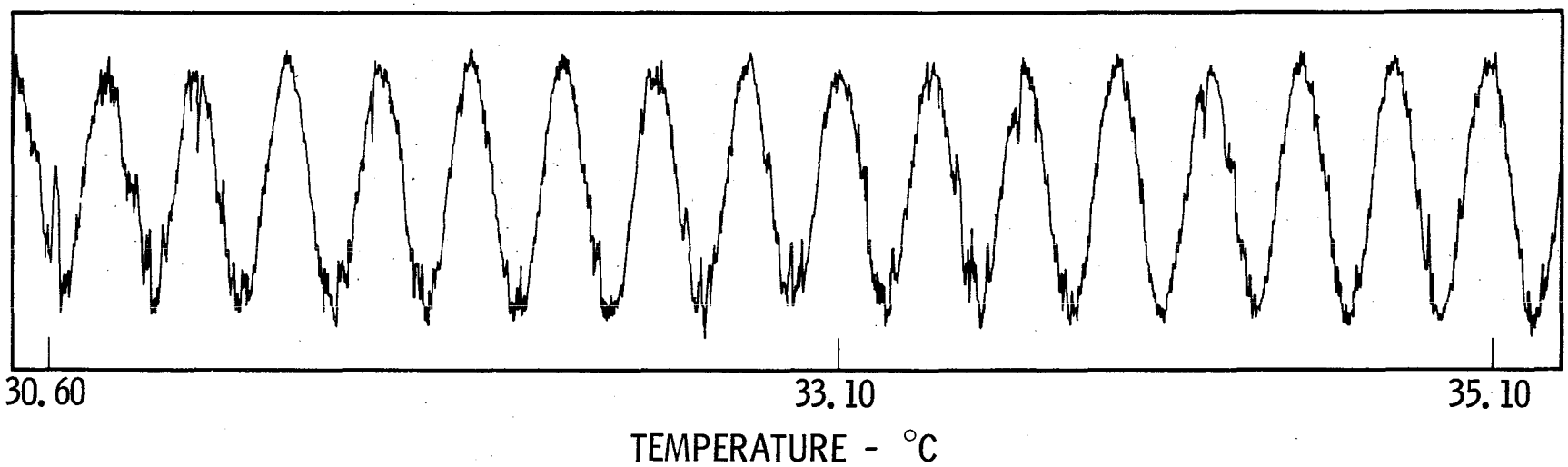

Fig. 20. Fizeau fringe motion for 0^{o} ruby at 1.064 μm.

Direction and Polarization	n	α_n ($\times 10^{-6}$/°C)	dn/dT ($\times 10^{-6}$/°C)
x-axis rod			
$\vec{E} \parallel \hat{Z}$	2.0566	-4.06	-8.35
$\vec{E} \parallel \hat{Y}$	2.0184	-3.74	-7.55
y-axis rod			
$\vec{E} \parallel \hat{X}$	1.9841	+2.37	+4.70

Table 7. Thermo-optic coefficients of BeL:Nd at 6328 Å over the interval 30-45°C.

λ (μm)	α_n (10^{-6}/°C)
0.4765	+0.21
0.5017	-0.57
0.6328	-1.84
1.0642	-3.70

Table 8. Wavelength variation of thermo-optic coefficient of Nd:Kodak glass rod over the temperature interval 30-60°C. Measured $\alpha_\ell = 13.30 \pm 0.3 \times 10^{-6}$/°C.

ordinary polarization was 12.95 ± 0.3 x $10^{-6}/^{o}C$ at 6328 Å and 12.29 ± 0.3 x $10^{-6}/^{o}C$ at 1.0642 μm. Malitson et al.[8] found dn/dT for clear sapphires to be 12.8 x $10^{-6}/^{o}C$ at 6438 Å, very close to our measurement. The plot of α_n/α_ℓ vs. $\Delta T_T/\Delta T_F$ for 0^{o} ruby is shown in Fig. 10 as the dashed curve. α_n/α_ℓ for our 6328 Å measurement was 1.068 (black dot), and 1.11 (open circle) for the 5461 Å measurement of Houston et al.[3]

4. Measurement of Thermal Change of Birefringence by Fringe Beats

During the interferometry measurements we found an accurate method of measuring the change of birefringence with temperature, more accurate than any other method used before. For our study this method was applied to several anisotropic solid-state laser materials: ruby, BeL and YALO. In the future, this new method will be more useful in determining the phase matching conditions of nonlinear optical crystals.

Beating of the thermal motions of the Fizeau fringes for the two fundamental polarization directions in anisotropic crystals is due to the thermal change of birefringence. Birefringence is defined as $B \equiv n_e - n_o$. From Eq. (2), the intensity in a Fizeau fringe pattern for each polarization, ordinary and extraordinary, is a sine-squared function with arguments $2n_o k\ell$ and $2n_e k\ell$, respectively. The Fizeau fringe intensity for unpolarized light is just the arithmetic sum of these two intensity patterns, since orthogonal polarizations are independent. Assuming that the Fresnel reflection coefficients of both polarizations are equal, the unpolarized Fizeau intensity pattern is

$$\begin{aligned} I &= 4\, r^2\, (\sin^2 n_o k\ell + \sin^2 n_e k\ell) \\ &= 4\, r^2\, (1 - \cos Bk\ell \cos 2\bar{n}k\ell) \end{aligned} \qquad (17)$$

where the mean refractive index is $\bar{n} = (n_o + n_e)/2$. Since $\bar{n} > B$, the cos Bkl factor is a slow modulation of the more rapid cos 2 $\bar{n}$kl variation. Similarly, the unpolarized Twyman-Green intensity is

$$I = 4 \left[1 + \cos B k\ell \cos 2k\ell \left(\bar{n} - 1 + \frac{\Delta L}{\ell}\right)\right] \tag{18}$$

Notice that the modulation of the Twyman-Green pattern is exactly that of the Fizeau pattern.

Following the previous procedure, Eqs. (3) - (4), the thermal change of these patterns are determined by the following temperature periods:

$$\Delta T_B = \frac{\lambda}{2B\ell} \frac{1}{\alpha_\ell + \alpha_B} \tag{19}$$

$$\Delta T_{SF} = \frac{\lambda}{2\bar{n}\ell} \frac{1}{\alpha_\ell + \alpha_{\bar{n}}} \tag{20}$$

$$\Delta T_{ST} = \frac{\lambda}{2\bar{n}\ell} \left[\left(\frac{\bar{n}-1}{\bar{n}}\right) \alpha_\ell + \alpha_{\bar{n}} \right]^{-1} \tag{21}$$

where $\alpha_B \equiv B^{-1}\, dB/dT$ and $\alpha_{\bar{n}} \equiv (\bar{n})^{-1}\, d\bar{n}/dT$.

ΔT_B is the temperature difference between nulls in the beating for both the Fizeau and Twyman-Green patterns. ΔT_{SF} and ΔT_{ST} are the temperature periods of the rapid fringe motions for the Fizeau and Twyman-Green patterns, respectively. From these three measurements, the three coefficients α_ℓ, α_B and $\alpha_{\bar{n}}$ can be determined.

$$\alpha_\ell = \frac{\lambda}{2\ell} \left(\frac{1}{\Delta T_{SF}} - \frac{1}{\Delta T_{ST}}\right) \tag{22}$$

$$\alpha_B = \frac{\lambda}{2\ell} \left(\frac{1}{B\Delta T_B} + \frac{1}{\Delta T_{ST}} - \frac{1}{\Delta T_{SF}}\right) \tag{23}$$

$$\alpha_{\bar{n}} = \frac{\lambda}{2\ell} \left[\frac{1}{\Delta T_{ST}} - \left(\frac{\bar{n}-1}{\bar{n}}\right) \frac{1}{\Delta T_{SF}}\right] \tag{24}$$

Since in general $B \ll 1$, a simple approximate formula for dB/dT is found from Eq. (23):

$$dB/dT \cong \lambda/2\ell\Delta T_B. \qquad (25)$$

This approximation is a slight over-estimate by the amount $B\alpha_\ell$, only a 3% discrepancy for ruby. Thus, a rapid direct determination of dB/dT can be made from the beats in either the Fizeau or Twyman-Green fringe motions with temperature.

Figure 21 shows the beats in the fringe motions for 60^o ruby using unpolarized 6328 Å light. Table 9 lists the measured temperature periods and the derived coefficients α_ℓ, $\alpha_{B'}$, $\alpha_{\bar{n}'}$ where the primes indicate that the extraordinary index is the value at 60^o. The extraordinary index of refraction θ is given by the formula:

$$n_e(\theta) = n_o n_e (n_e^2 \cos^2\theta + n_o^2 \sin^2\theta)^{-\frac{1}{2}} \qquad (26)$$

Figure 22 shows the beating of the Fizeau fringes for the 60^o ruby using the CW Nd:YAG laser as probe. Using the coefficient of linear thermal expansion for 60^o obtained at 6328 Å, the value of dB'/dT at 1.0642 μm was found to be $1.09 \times 10^{-6}/^oC$.

Beating of the Fizeau and Twyman-Green fringes was observed for Nd:BeL, but the beats were not as definitive as for ruby because ΔT_B was nearly ΔT_{SF} and ΔT_{ST}. Figure 23 shows the fringe beating for x-axis Nd:BeL at 6328 Å, and Figure 24 shows the fringe beating for y-axis BeL.

Figure 25, 26 and 27 show the Fizeau beat patterns for the a, b and c axes for Nd, Cr:$YA\ell O_3$ samples using the He-Ne laser as probe beam. Listed in Table 10 are the coefficients of linear expansion and thermal variation of birefringence.

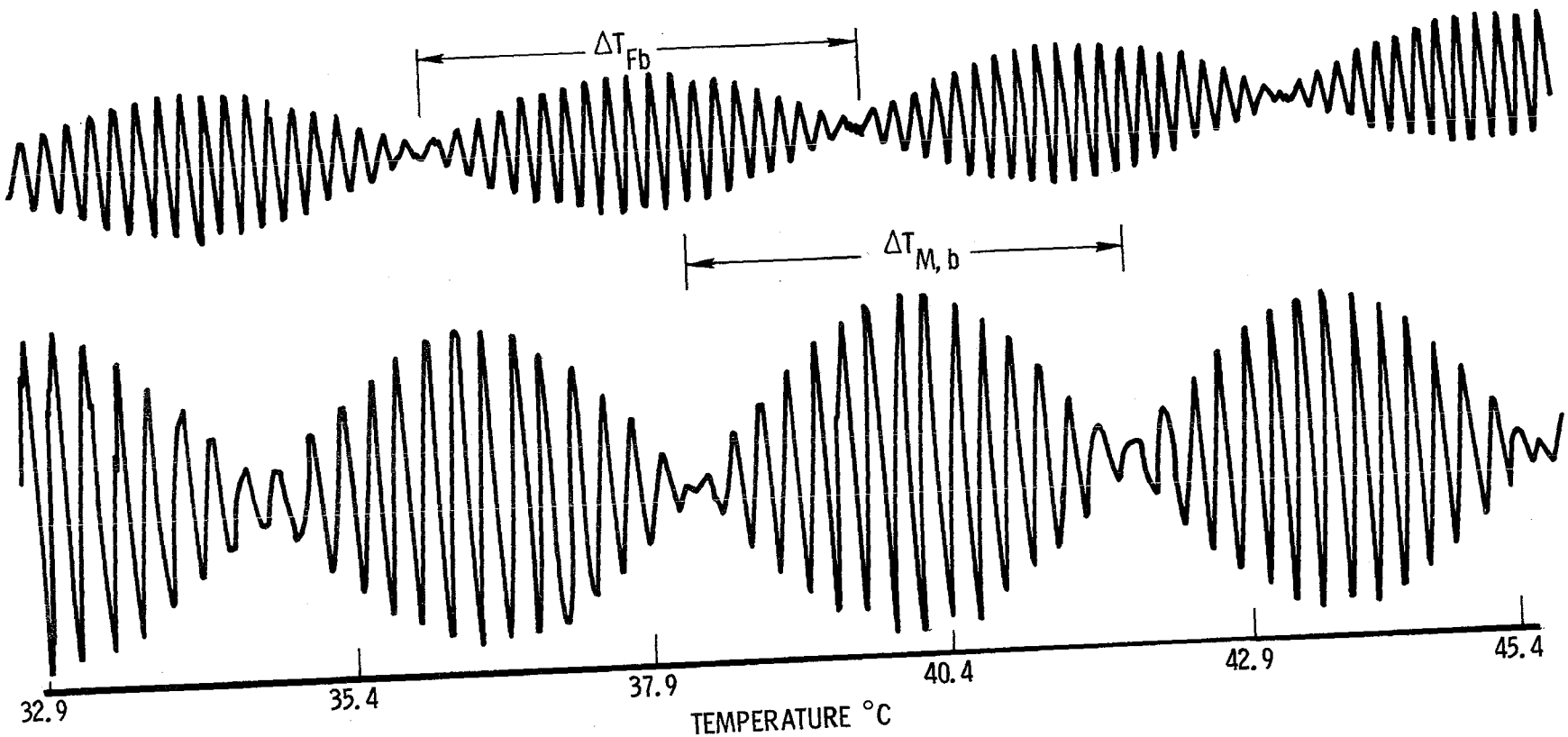

Fig. 21: Fringe beating for 60° ruby using unpolarized 6328Å light. Fizeau fringe motion is top trace, and Twyman-Green fringe motion is bottom trace.

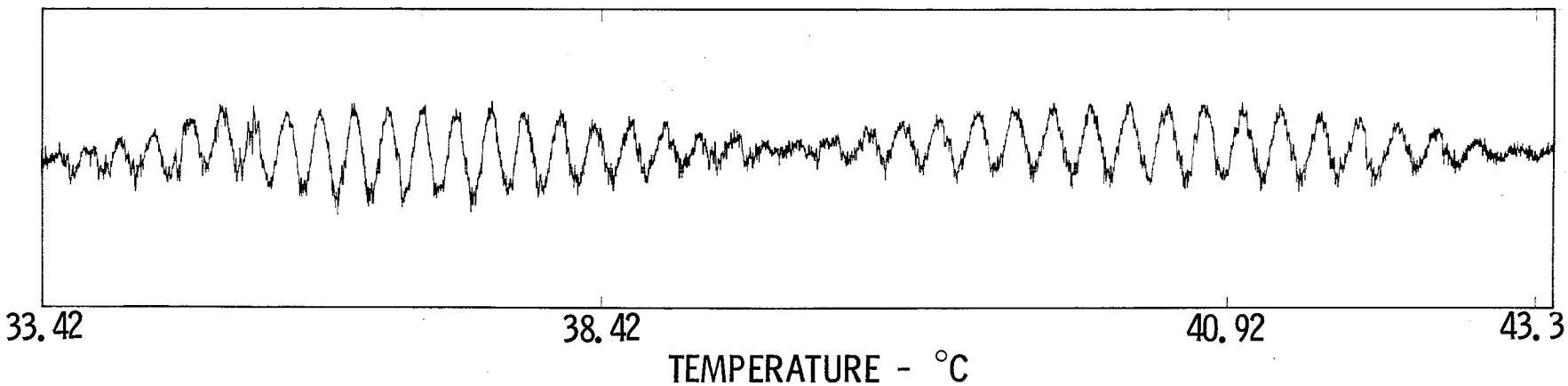

Fig. 22: Fizeau fringe beats for 60^{o} ruby at 1.0642 μm.

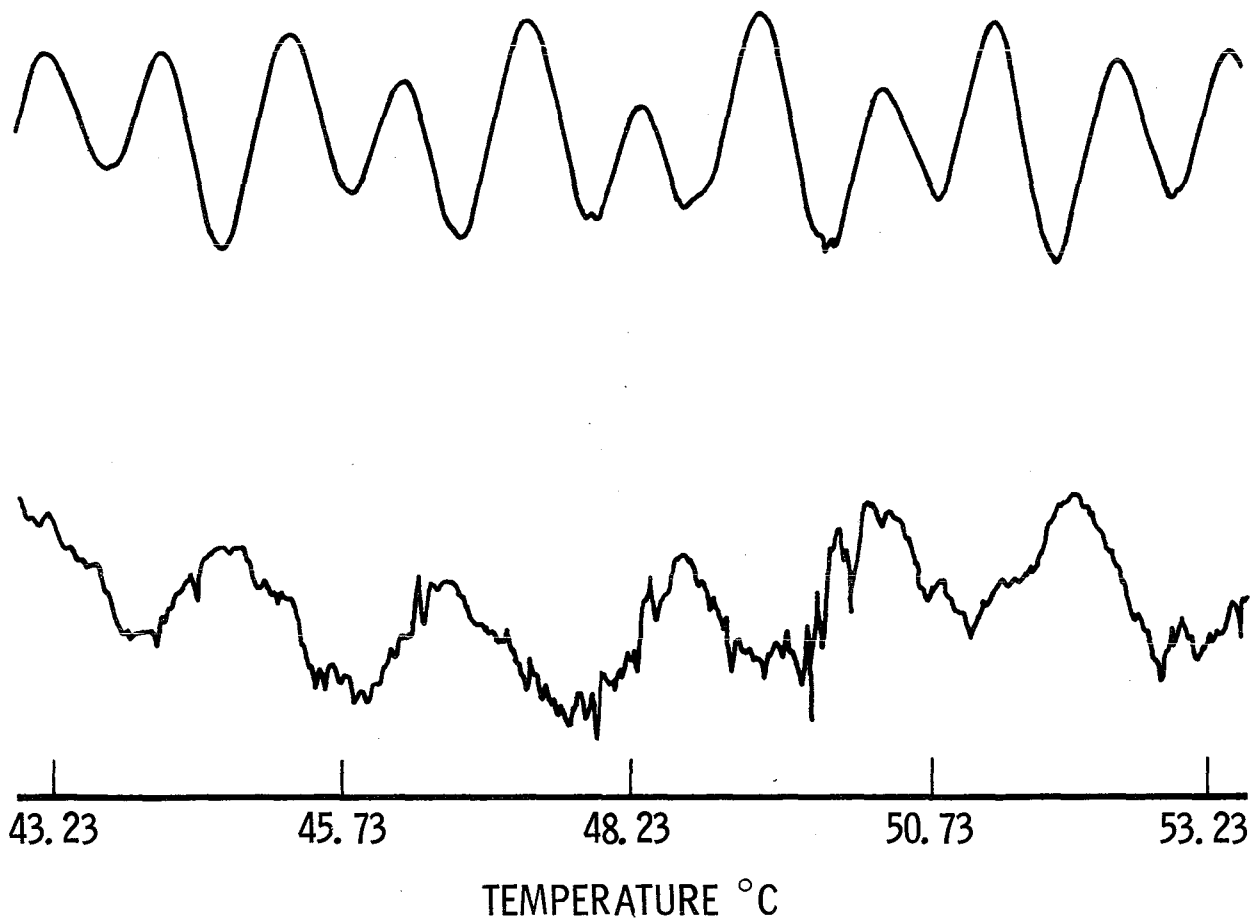

Fig. 23: Fringe beating for x-axis Nd:BeL at 6328 Å. Top trace is Fizeau fringe motion and bottom trace is Twyman-Green fringe motion.

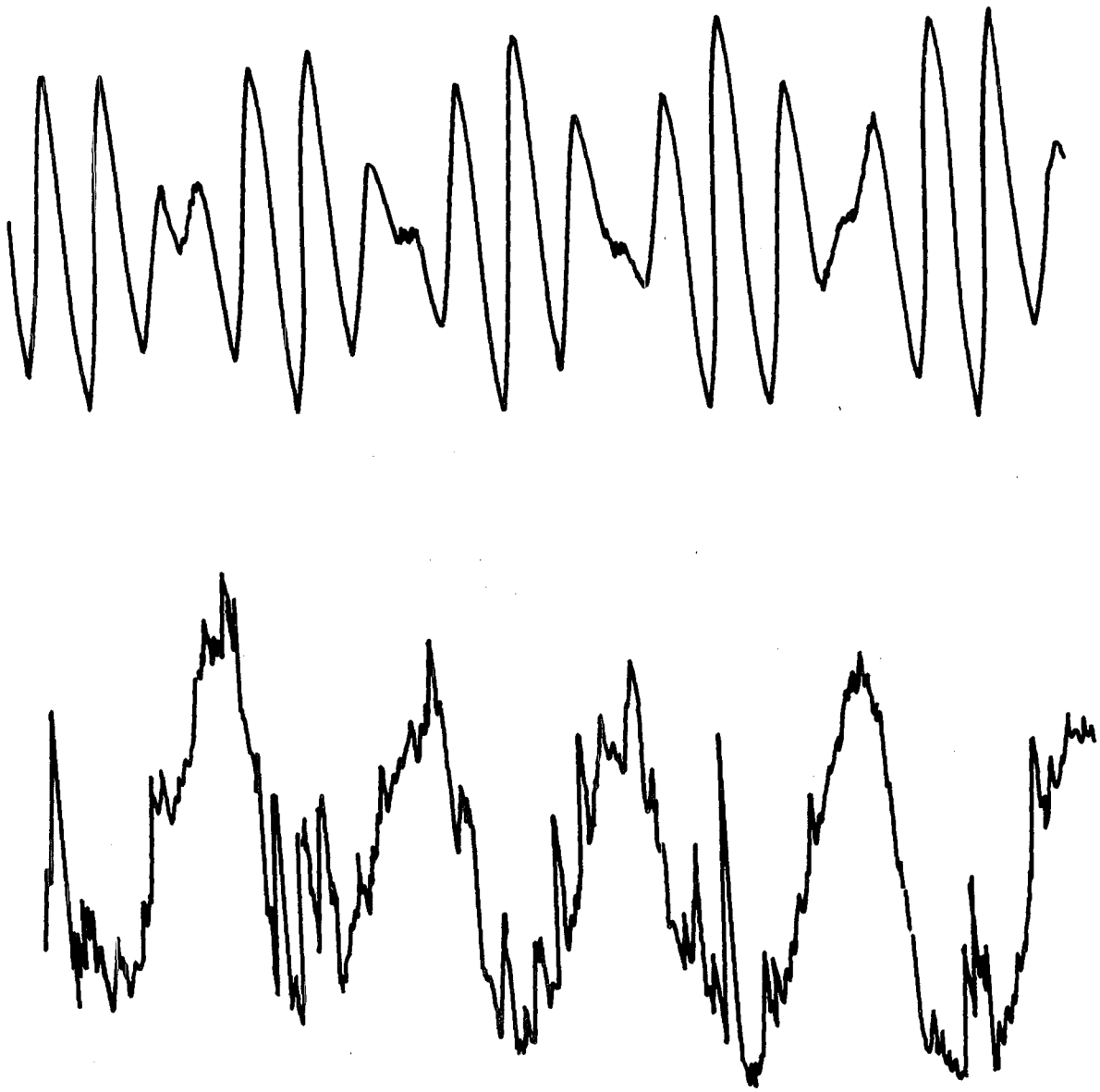

Fig. 24: Fringe beating for y-axis Nd:BeL at 6328 Å. Top trace is Fizeau fringe motion and bottom trace is Twyman-Green fringe motion.

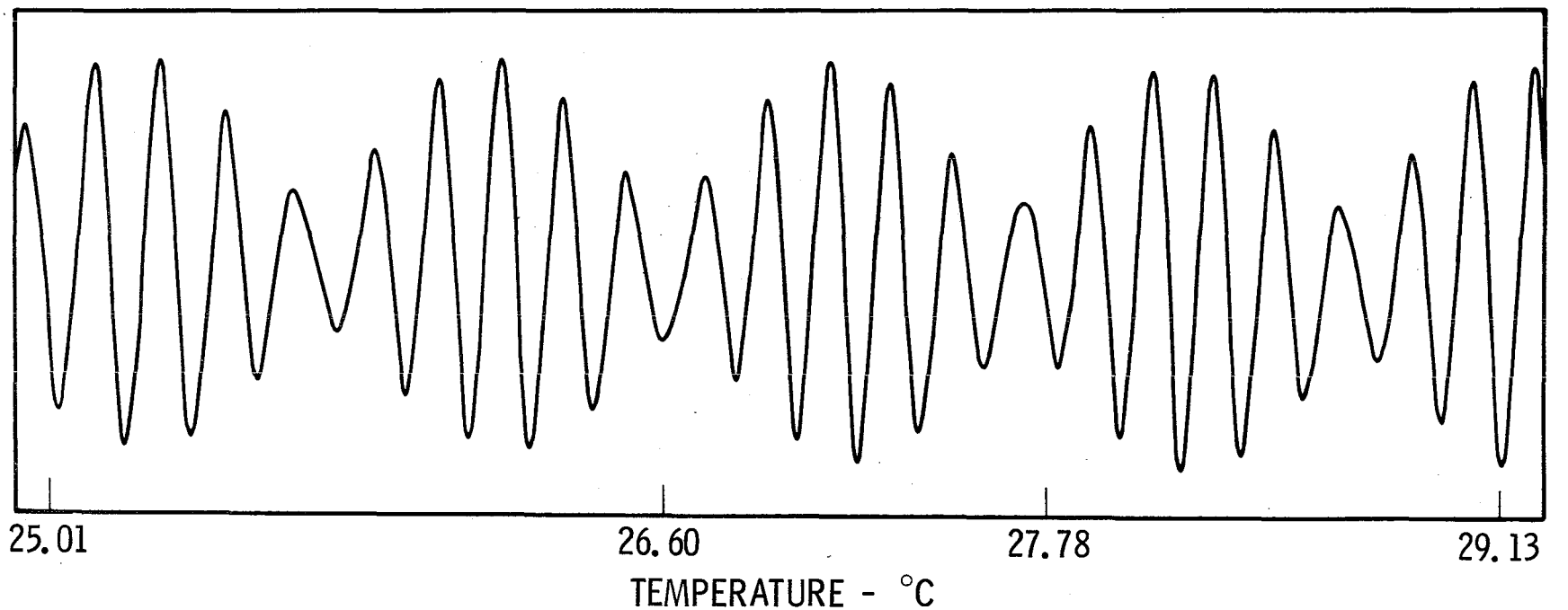

Fig. 25: Fizeau fringe beating for a-axis Nd, Cr:YALO at 6328 Å.

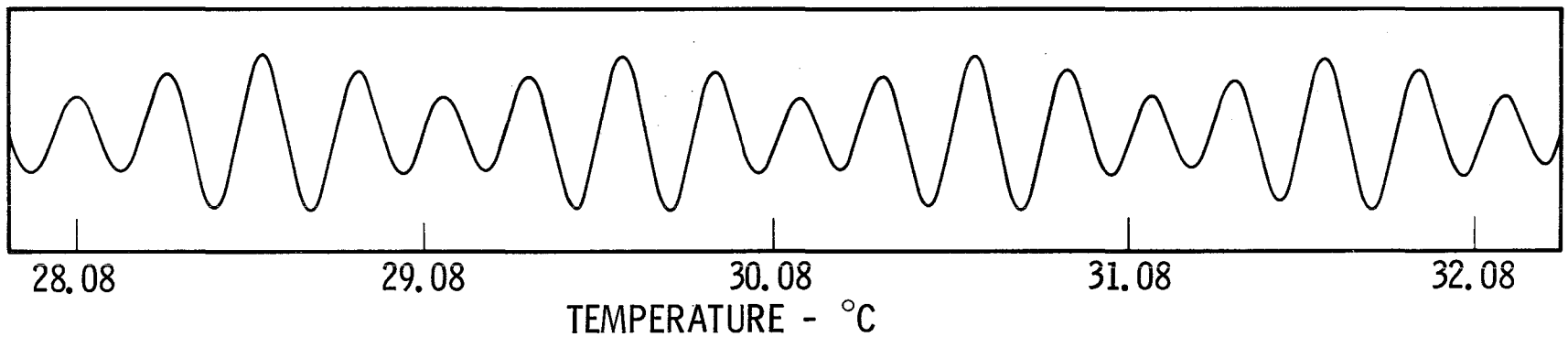

Fig. 26: Fizeau fringe beating for b-axis Nd, Cr:YALO at 6328 Å.

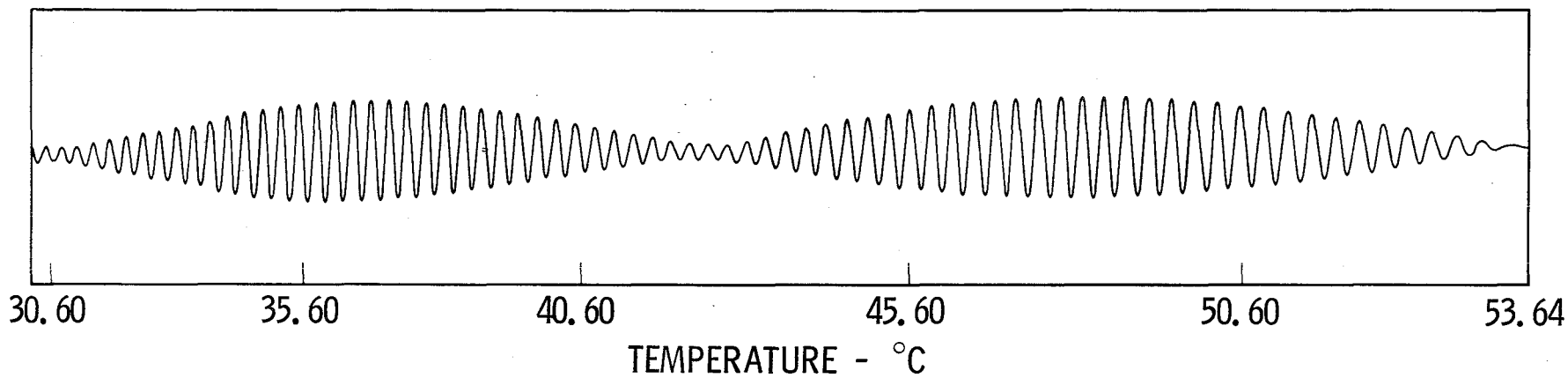

Fig. 27: Fizeau fringe beating for c-axis Nd, Cr:YALO at 6328 Å.

Parameter	Value
ΔT_{FS}	$0.1750 \pm 0.002°C$
ΔT_{FB}	$3.491 \pm 0.220°C$
ΔT_{TS}	$0.2308 \pm 0.006°C$
ΔT_{TB}	$3.525 \pm 0.09°C$
$\alpha_{B'}$	$248.3 \times 10^{-6}/°C$
$\alpha_{\bar{n}'}$	$7.71 \times 10^{-6}/°C$
α_{ℓ}	$5.71 \times 10^{-6}/°C$
dB'/dT	$1.15 \times 10^{-6}/°C$
dn_o/dT	$12.99 \times 10^{-6}/°C$
dn_e'/dT	$14.14 \times 10^{-6}/°C$

Table 9. Measured temperature periods ΔT and thermo-optic coefficients of 60° ruby at 6328 Å over the interval 30-45°C. Refractive indices are $n_e = 1.7578$ and $n_o = 1.7640$. At 60°, extraordinary index $n_e' = 1.76244$, $\bar{n}' = 1.76012$ and $B' = 0.00464$.

Orientation	α_ℓ (10^{-6}/°C)	dB/dT (10^{-6}/°C)
A-axis	9.62 ± 0.25	5.89 ± 0.02
B-axis	3.73 ± 0.57	5.61 ± 0.05
C-axis	10.11 ± 0.33	0.39 ± 0.01

Table 10. Coefficients of linear thermal expansion and temperature dependence of the birefringence of Nd, Cr:$YALO_3$ as measured by fringe beating.

C. Stress-Induced Birefringence

Stress-induced birefringence of samples of Nd in YAG, BeL and ED2.1 glass was measured using the polariscope arrangement shown in Fig. 28. This stress-optic experiment used the new technique of producing radial stress by heating a very small volume of the sample with a focused laser beam. This approach has been used only once before [21] in a study of the stress-optics of IR windows with a CO_2 laser. In our experiment, since visible transmissive materials are involved, an 18W argon-ion laser was used to heat the material via Nd absorption.

An argon-ion laser beam was focused into a 3-mm thick sample heating a small 50-μm diamter cylindrical volume. The light is absorbed by the neodymium ions in each sample pumping them up to an excited state. The ions will then convert the pump energy into both heat (nonradiative decay) and fluorescence energy (0.9, 1.06 and 1.32 μm). Now, the thermal expansion of the heated volume creates a cylindrically symmetric stress which causes optical birefringence of the photoelastic effect. The amount of birefringence is measured by passing a He-Ne laser probe beam through the sample nearly collinear ($\sim 10^{o}$) with the argon-ion laser beam. The probe beam is expanded sufficiently to illuminate the entire sample aperture (1 cm^2) and passed between crossed Glan polarizers, one on either side of the sample. The birefringence pattern, called in optics the "interference figure," is then projected onto a film plane by lens L_2 where it is recorded on Polaroid type 57 film.

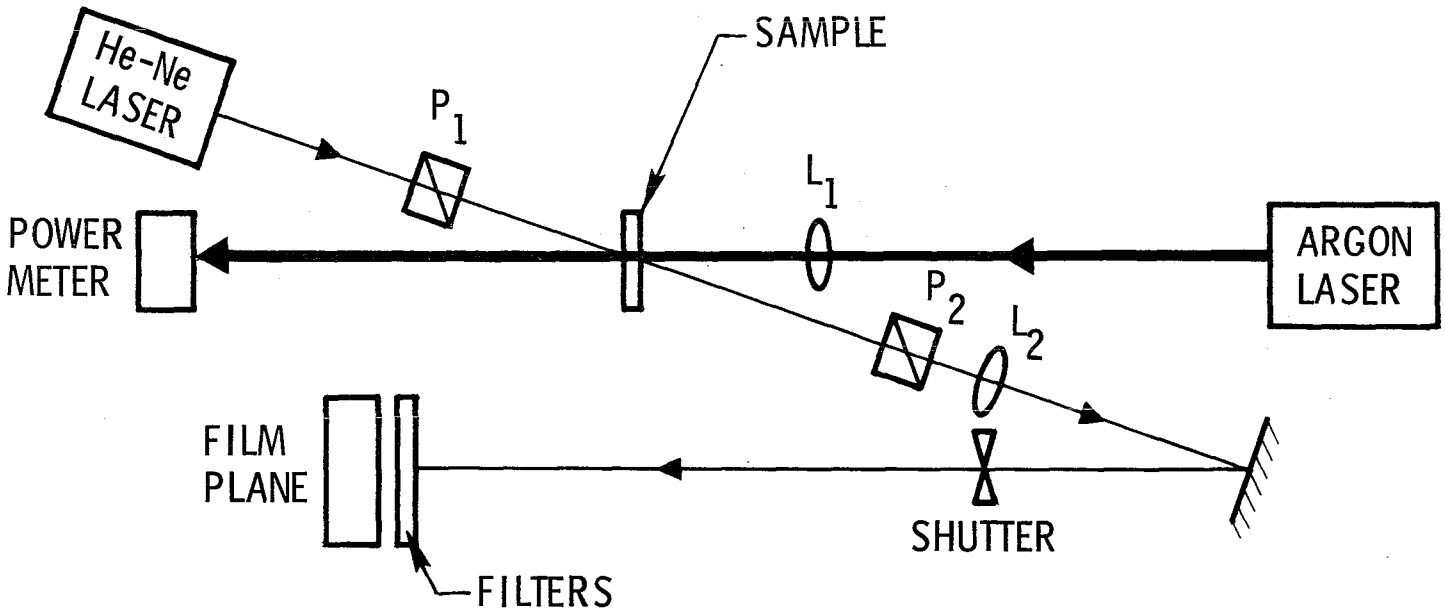

Fig. 28: Schematic of Stress-induced birefringence experiment.

The interference figure for ED2.1 glass is shown in Figure 29. The radial stress in this normally isotropic material produces a uniaxial optic axis parallel to the heated filament. The observed interference figure is identical to the classic "ring-and-brush" pattern observed in unstressed uniaxial crystals cut perpendicular to the optic axis when placed in a polariscope[22]. An interference figure of typical uniaxial crystal (taken from ref. 22) is shown in Figure 29 for comparison.

The general formula for the intensity $I(\theta, \phi)$ in the interference figure of a uniaxial crystal of thickness L is

$$I = \frac{(\delta_o - \cos^2\theta\delta_e)^2 \sin^2 2\phi}{(4\cos^2\theta + \sin^2 2\phi \sin^4\theta)} \qquad (27)$$

where

$$\delta_o = \exp(-ikn_o \sec\theta/L)$$

$$\delta_e = \exp(-ikn_e(\theta)\sec\theta/L)$$

with $n_e(\theta)$ given by Eq. (26). θ is the divergence angle of ray from optic axis and ϕ is the angle between the principal plane of the ray and the polarizer acceptance plane. In the observation plane, the intensity is expressed in the polar coordinates r, ϕ where $r = L \tan\theta$. In the small divergence angle approximation ($\theta \ll 1$), which is applicable for our case, the phase term becomes

$$(\delta_o - \cos^2\theta\delta_e)^2 \simeq 4 \sin^2 (kBL\theta^2/2) \qquad (28)$$

where

$$B \cong n_o(n_o^2 - n_e^2)/2n_e^2 \ .$$

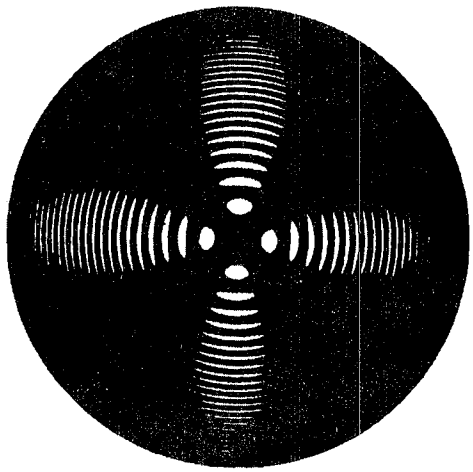

TYPICAL UNIAXIAL CRYSTAL

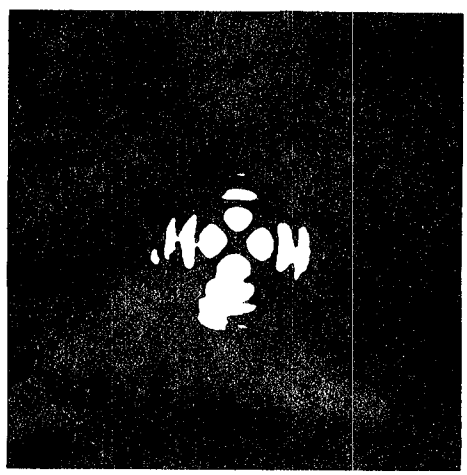

STRESSED ED2.1 GLASS

Fig. 29 Comparison of interference figure of stressed ED2.1 glass with that of a typical uniaxial crystal.

Then, the intensity of the interference figure in the observation plane is

$$I \cong \sin^2 2\phi \sin^2 (kBr^2/2L). \tag{29}$$

This is identical to the transmission of a crystal between crossed polarizers according to Drude,[23] except with inclusion of the r^2/L^2 factor which represents the change of the extraordinary refractive index with divergence from the optic axis.

From Eq. (29) it is seen that the rings of zero intensity in the interference figure have radii r_N where

$$r_N = (2N\pi L/kB)^{\frac{1}{2}} \tag{30}$$

where N is an integer. Thus, the dark rings in the interference figure obey the relation

$$r_N = r_1 \sqrt{N} \quad . \tag{31}$$

The dark rings in both of the interference figures of Fig. 29 were observed to obey Eq. (31), demonstrating the appropriateness of the small angle approximation.

To get quantitative results we replaced the film plane shown in Figure 28 with a radiometer and measured the He-Ne laser power transmitted by the sample as a function of the argon-ion laser power absorbed. The birefringence is directly proportional to the square-root of the transmittance through the crossed polarizers. This relation is derived by integrating Eq. (29) over a central disk of radius R of the interference figure. The transmittance T over area πR^2 is:

$$T = \frac{1}{\pi R^2} \int_0^{2\pi} \int_0^R \sin^2 2\phi \sin^2 (kBr^2/2L)\, r\, dr\, d\phi$$

$$= \tfrac{1}{4} \left[1 - \frac{L}{kBR^2} \sin (kBR^2/L)\right] \tag{32}$$

For small birefringences, $B << 1$, this transmittance becomes

$$T \cong k^2B^2R^4/24L^2,$$

or

$$B \cong \left(\frac{2\sqrt{6}\,L}{kR^2}\right)\sqrt{T} \qquad (33)$$

This approximation is valid for our experiment since the order of magnitude of T is 10^{-3}.

Figure 30 shows the interference figure induced in Nd:YAG as a function of incident argon-ion laser power P_{inc}. The exposure times T_{ex} indicate the relative amount of transmission at each power setting. YAG has a cubic structure so it is isotropic when unstressed as is the ED2 glass. However, since the stress-optic tensor is a fourth rank tensor, an axial heating term will in general produce a biaxial stress in YAG and not a uniaxial stress[24]. For the <111> direction, a stress will be produced in YAG as shown in Figure 30. The picture at the upper left was taken when no heating was present and can be taken as a reference. The remaining pictures show the evolution of the birefringence pattern with increased heat loading.

The patterns observed for Nd:BeL are vastly different from the patterns of the two previous cases as shown in Figure 31. Since unheated BeL is biaxial it is not surprising that the stress pattern is much different from the isotropic cases. In order that there be no transmission of the probe beam when there is no heating of the sample, the crystal is rotated about the axis of the probe beam in the ϕ direction, until the fast and slow axes are aligned with the crossed polarizers ($\phi = 0^o$). The "a" pictures were taken when ϕ was equal to zero degrees and T_{ex} was two minutes. The "b" pictures were taken when ϕ was 90^o. The unprimed captions refer to patterns where no heating

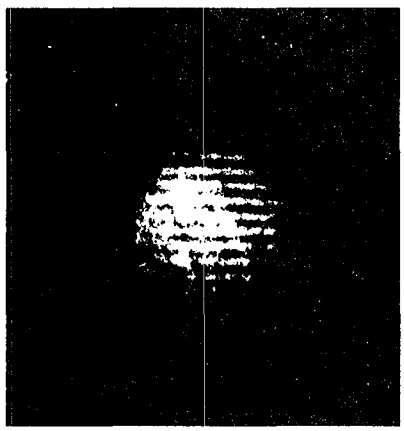

P_{inc} = 0.0W
T_{ex} = 28 sec

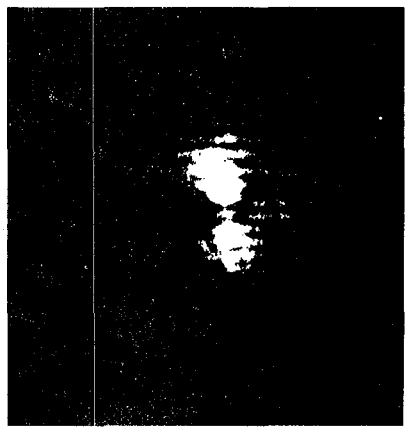

P_{inc} = 1.2W
T_{ex} = 24 sec

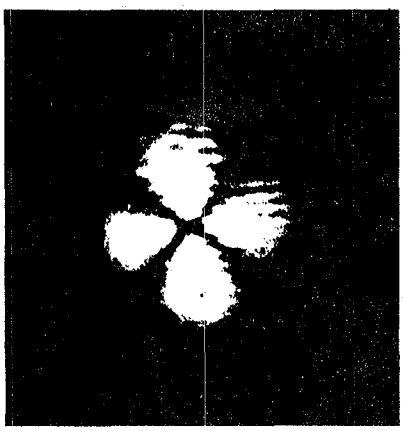

P_{inc} = 6.4W
T_{ex} = 3.0 sec

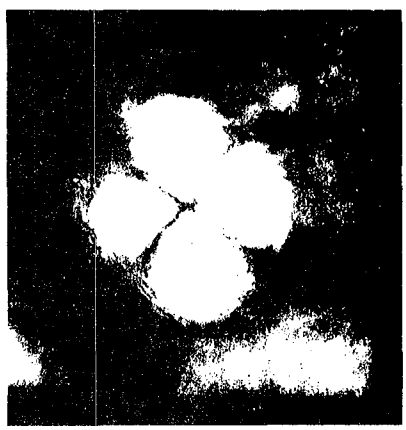

P_{inc} = 10.0W
T_{ex} = 3.0 sec

Fig. 30: Interference figure of <111> Nd:YAG as a function of incident argon-ion laser power.

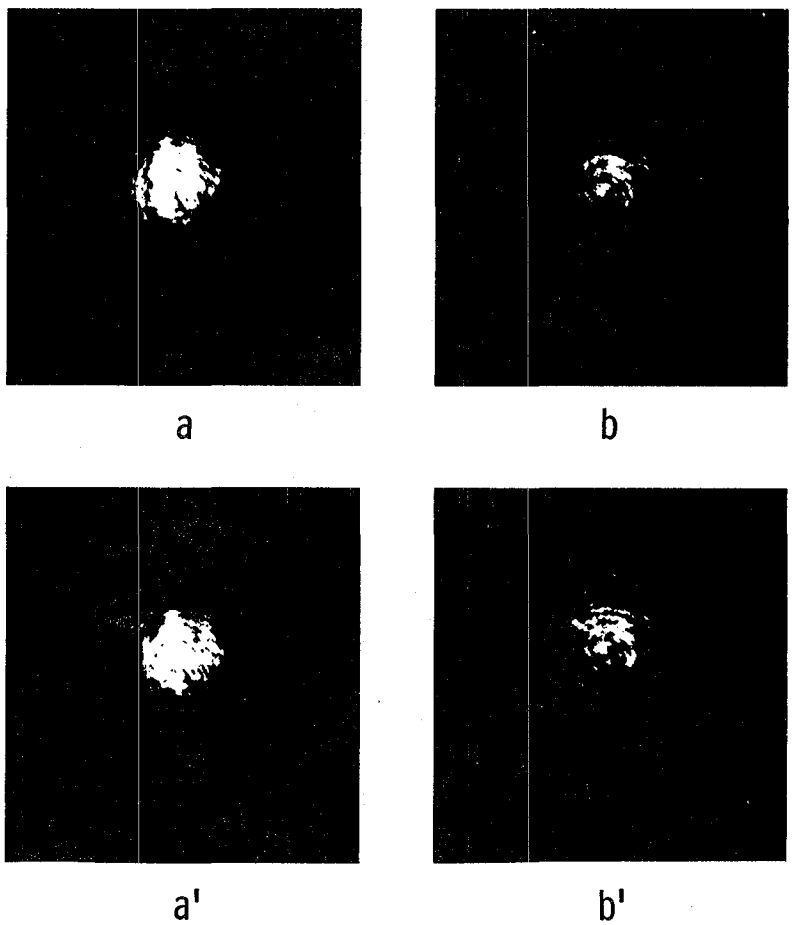

Fig. 31: Interference figures for Nd:BeL. "a" pictures are for $\phi = 0^{o}$ and "b" pictures for $\phi = 90$. Unprimed captions refer to no heating and primed, heating with 5 W incident power.

The poor optical quality of these interference figures is indicative of the mottled quality of the low level light transmitted through the crossed polarizers rather than the quality of the BeL material. These marginal distortions are visible in these pictures because of the long 2 minute exposure times.

was applied and the primed captions refer to those where 5W of argon laser power was incident on the sample.

As can be seen from these four pictures there is little difference between the "heating" and "no heating" cases. We can conclude then that the effect of stress-induced birefringence for Nd:BeL is nearly negligible. This result agrees with that of Massey[25] who proposed that any stress-induced birefringence present in a naturally birefringent material is approximately two orders of magnitude smaller than the natural birefringence and will therefore be negligible in comparison.

Even though Nd:BeL exhibits little stress-induced birefringence, it does show thermal lensing due to α_ℓ and α_n coefficients. Figure 32 is the pattern transmitted by Nd:BeL through slightly uncrossed polarizers. Notice the central bright spot that appears in the region where the heating is present. This spot cannot be the result of depolarization since it was not observed between crossed polarizers. It is due to a change in optical path with respect to temperature.

Figure 33 is a comparison of the stress-optic effect in the three samples studied. Again the exposure times are a measure of the order of magnitude of the effect. All three samples have nearly the same Nd concentration and approximately the same incident argon power. The ED2.1 the exposure time T_{ex} is 0.0167 sec, for YAG it is 0.10 sec and for BeL it is 90 sec. Since the transmittance is proportional to the inverse of T_{ex}, the estimated ratio of transmittances of ED2:YAG:Bel is 6000:1000:1.

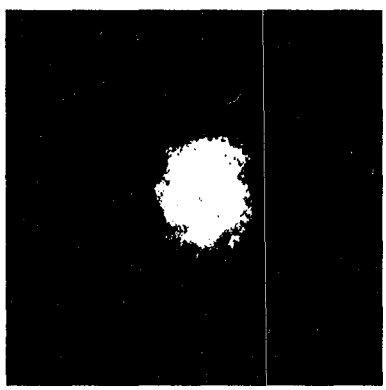

Fig. 32: Thermal lensing in Nd:BeL. (Bright central spot was more discernible in original photograph).

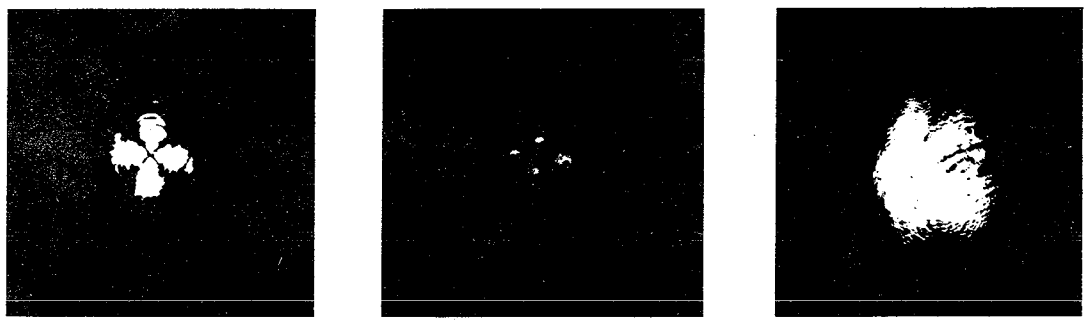

Fig. 33: Comparison of interference figures for ED2.1, YAG and BeL at same incident power.

A more accurate comparison of ED2, YAG and BeL was made by measuring photoelectrically the transmittance vs. power absorbed at 5145 Å. A line-selecting prism in the argon-ion laser cavity permitted only the 5145 Å line to lase. Figure 34 shows the results for Nd:YAG where the bottom curve is a quadratic curve fitted to the data. The top curve is the birefringence which is proportional to the square-root of the transmittance. It is observed that the measured birefringence is linearly proportional to the heat power deposited by the argon-ion laser.

Figure 35 compares the stress-induced birefringence vs. power absorbed for ED2, YAG and BeL in a log-log plot. Table 11 lists the induced birefringence per power absorbed (B/P) determined from the least-squares fit to the data. It is seen that BeL has only one-twentieth of the induced birefringence of YAG for the same power absorbed.

D. Thermal Lensing

In the analyses available in the literature,[26, 27] the laser rod is assumed to be a long cylinder, pumped uniformly throughout its volume and cooled uniformly over its cylindrical surface. Under these conditions, a radial thermal gradient develops to carry heat outward to that surface. This radial gradient, strongest near the outer edge, modifies the refractive index due to both the temperature change and induced strain. The net effect is to give the rod a lens-like character. The relationship[27] of the focal length f of the rod to the material and rod parameters is:

$$1/f = (P/2KA)\ [dn/dT + n^3\alpha C + (n-1)\alpha d/L] \qquad (34)$$

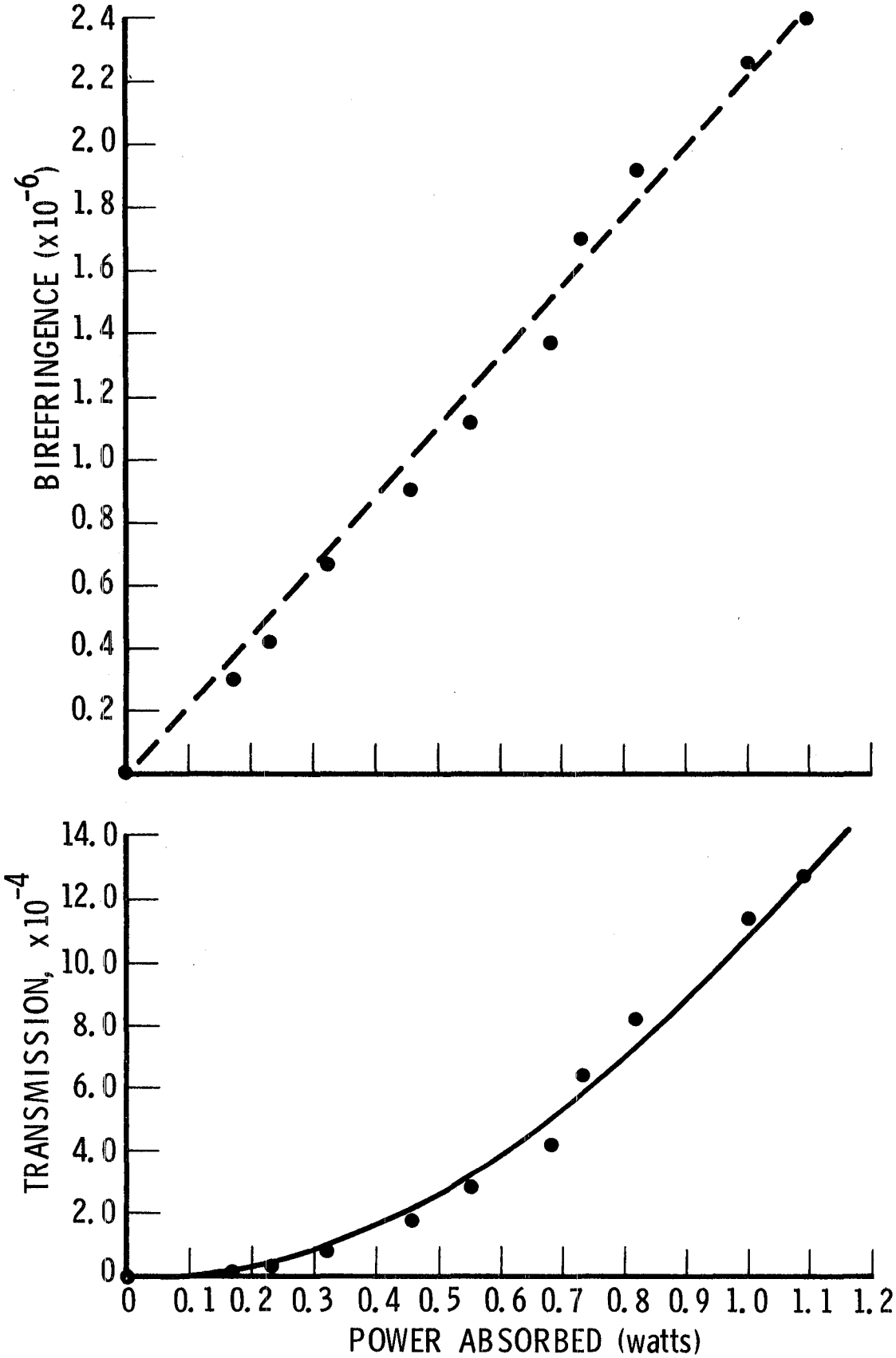

Fig. 34 Transmission and birefringence vs. power absorbed at 5145 Å for Nd:YAG

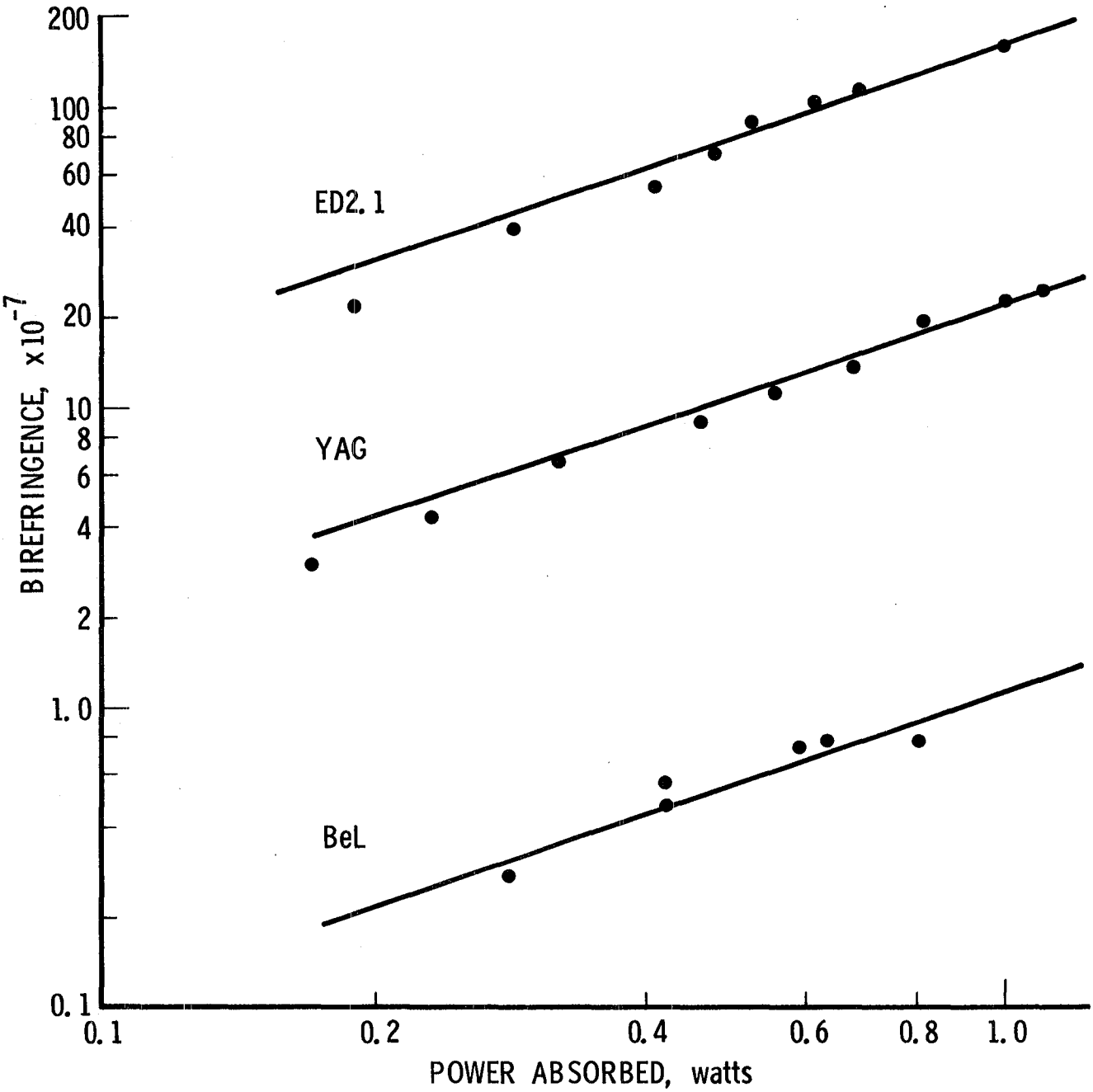

Fig. 35 Birefringence vs. power absorbed at 5145 Å for ED2, YAG and BeL

Sample	B/P (10^{-6}/watt)	Relative to YAG
ED2.1	11.63 ± 0.16	3.1
YAG:Nd	3.78 ± 0.02	1
BeL:Nd	0.08 ± 0.02	0.02

Table 11. Induced birefringence per power absorbed (B/P) for neodymium samples.

where P is heat power producing by pumping, K is thermal conductivity, A is rod cross-sectional area, C is stress-optic parameter, d is rod diameter and L is rod length. These thermal lensing parameters were evaluated for YAG, ED2 and BeL and are listed in Table 12. The stress-optic term $n^3\alpha C$ for YAG was set equal to the value calculated by Koechner[27] and then the values of the stress-optic terms for ED2 and BeL followed from Table 11 The other terms for YAG and BeL were calculated from the results of this report, while for ED2 glass these thermo-optic and thermal expansion terms were calculated from the values of S.D. Jacobs[28], University of Rochester. For a typical window size where $\gamma = 3$, all three materials exhibit a positive lens with with YAG having the shortest focal length due to its high thermo-optic term. However, for a typical laser rod where $\gamma = 0.1$, x-axis BeL exhibits a negative lens for the laser wavelength (1.079 μm) with polarization E||y. For $\gamma = 0.1$, YAG and ED2 laser rods show positive lensing. It is believed that the negative thermal lensing will be more detrimental to laser performance than positive lensing. An interesting possibility of compensation of thermal lensing is seen for Nd:BeL. When the geometric aspect ratio γ has a certain value, the positive thermal expansion term will cancel the negative thermo-optic term. For the values given in Table 12, this value is $\gamma = 0.625$ for BeL.

Material	Thermo-optic dn/dT	Stress-optic $n^3 \alpha C$	Thermal expansion $(n-1)\alpha\gamma$	$\frac{1}{f}(\frac{2KA}{P})$ Window ($\gamma = 3$)	Laser rod ($\gamma = 0.1$)
YAG	9.0	1.8	5.85 γ	28.4	11
ED2	3.1	5.6	4.27 γ	22	9
BeL	-7.6	0.04	11.85 γ	28	-6

Table 12. Thermal lensing parameters for YAG, ED2 glass and BeL laser materials. Lensing due to thermal expansion depends on the sample shape where the geometric aspect ratio $\gamma \equiv d/L$. All numbers are in units of $10^{-6}/°C$.

E. REFERENCES

1. J. D. Foster and L. M. Osterink, Appl. Opt. 7, 2428 (1968). Although the quoted refractive index is in error by -0.006, the reported measurements remain unchanged within the experimental accuracy.
2. P. H. Klein and W. J. Croft, J. Appl. Phys. 38, 1608 (1967). Coefficient of thermal expansion was determined from thermal change of x-ray density ($\alpha_\ell = -\frac{1}{3\rho}\frac{d\rho}{dT}$).
3. T. W. Houston, L. F. Johnson, P. Kisliuk and D. J. Walsh, J. Opt. Soc. Am. 53, 1286 (1963).
4. K. Nassau and A. M. Broyer, J. Appl. Phys. 33, 3064 (1962).
5. J. D. Feichtner and A. Mego, Appl. Opt. 11, 1433 (1972).
6. K. B. Steinbruegge et al., Appl. Opt. 11, 999 (1972).
7. G. D. Baldwin and E. P. Riedel, J. Appl. Phys. 38, 2726 (1967).
8. I. H. Malitson et al., J. Opt. Soc. Am. 48, 72 (1958); M. A. Jeppeson, J. Opt. Soc. Am. 48, 629 (1958).
9. H. L. Fizeau, Ann Physik u. Chem. 123, 515 (1864).
10. A. Y. Cabezas, L. G. Komai and R. P. Treat, Appl. Opt. 5, 647 (1966).
11. H. G. Lipson et al., Appl. Opt. 15, 2352 (1976).
12. R. Weil, J. Appl. Phys. 40, 2857 (1969).
13. H. L. Wang, PhD dissertation, University of Southern California (1975); H. L. Wang and L. G. DeShazer, J. Opt. Soc. Am. 64, 1383A (1974).
14. W. L. Bond, J. Appl. Phys. 36, 1674 (1965).
15. H. P. Jenssen, R. F. Begley, R. Webb and R. C. Morris, J. Appl. Phys. 47, 1496 (1976).
16. K. W. Martin and L. G. DeShazer, Appl. Opt. 12, 941 (1973).

17. International Critical Tables, editor E. W. Washburn (McGraw-Hill Book Co., New York, 1930), Vol. VII, p. 3, listed for neon 6334Å.

18. CRC Handbook of Chemistry and Physics, editor R. Weast (52nd edition, 1971-2), p.E-94.

19. G. N. Ramachandran, Proc. Indian Acad. Sci. A25, 266 (1947).

20. Y. Tsay, B. Bendow and S. S. Mitra, Phys. Rev. B8, 2688 (1973).

21. R. E. Joiner, J. Marburger and W. H. Steier, Appl. Phys. Letters 30, 485 (1977).

22. M. Born and E. Wolf, Principles of Optics, Third Edition (Pergamon Press, NY, 1964), p. 700.

23. P. Drude, Theory of Optics (Dover Press, NY, 1959), p. 344.

24. W.Koechner and D. K. Rice, J. Opt. Soc Am. 61, 758 (1971).

25. G. A. Massey, Appl. Phys. Letters 17, 213 (1970.

26. J. D. Foster and L. M. Osterink, J. Appl. Phys. 41, 3656 (1970).

27. W. Koechner, Appl. Opt. 9, 2548 (1970).

28. S. D. Jacobs, Proceedings of the Technical Program, Electro-Optics/Laser 78 Conference, Boston, Mass. Sept. 19-21, 1978. The values for ED2 glass given are α_{ℓ} = 7.7 x $10^{-6}/^{o}C$, dn/dT = 3.1 x $10^{-6}/^{o}C$ and n = 1.555 at 1.06 μm.

IV. LASER CROSS-SECTION DETERMINATIONS*

A. Introduction

In Q-switched operation an important parameter which determines the energy storage in the crystal and consequently the energy and peak power output of the laser is that of laser saturation. In essence, at high pumping levels, the inversion is lost by amplified stimulated emission. The energy storage (determined by the inversion density) is limited by the onset of prelasing.

If we denote the laser gain by G, then

$$\ln G = \sigma f_B N L \tag{1}$$

where σ is the peak gain cross section, f_B is the thermal population factor for the upper laser level, N is the population density of the $^4F_{3/2}$ levels, and L is the length of the rod. The onset of amplified stimulated emission, implies that the inversion density is approaching the maximum value and that a maximum gain value, G_{max}, is reached: The product of NL determines the energy storage capability. For example,

$$E_{max} = h\nu N_{max} L = \frac{h\nu \ell n G_{max}}{f_B \sigma} \ (J\ cm^{-2}) \tag{2}$$

where h = Planck's constants and ν the laser frequency. The maximum output intensity is, thus, according to Eq. (2) independent of rod length, doping and pumping energy. It is apparent from Eq. (2) that low σ favors high storage. Knowledge of σ is important in assessment of the laser crystal materials.

Determination of the cross-section for x-axis and y-axis Nd:BeL yielded 0.9×10^{-19} cm^2 and 1.4×10^{-19} cm^2 respectively. These values were obtained on the basis of a comparison to the cross-section of Nd:YAG ($\sigma = 4.6 \times 10^{-19}$ Ref. 1). However, considerable uncertainty exists with respect to the value obtained by Singh et al.[1] The results reported by different investigators based on spectroscopic measurements for the cross section have ranged from 2.7×10^{-19} to 8.8×10^{-19} cm^2.

*by M. Birnbaum, A. Tucker, C. Fincher

We plan to measure accurately the stimulated emission cross section for Nd:YAG by adapting our Argon ion laser pumping techniques.[2] This will, in turn, enable us to accurately state all those cross sections that we have measured relative to that of Nd:YAG at 1064 nm.

The Argon ion laser beam has a Guassian intensity profile. By apodization, a pump beam with a uniform intensity distribution should be obtained. Thus the volume of the pumped crystal that provides the laser output will be defined.

The stimulated emission cross section may be obtained from measurements of laser thresholds as a function of the output mirror reflectivities once the pumped volume is determined.

B. Theory of Operation

We will briefly restate the equations describing laser operation. These are required in order to correlate important characteristics of laser materials such as losses in the materials and the peak stimulated emission cross sections. Operation at threshold is described by

$$R_1 R_2 \exp [2 L(g-\Delta)] = 1 \qquad (3)$$

Since the Nd:YAG rod ends were AR coated, the Fresnel reflection of the rod ends may be neglected. Thus, R_1 and R_2 are the mirror reflectivities. L is the length of the laser crystal, g is the single-pass gain coefficient at threshold, and Δ is the total internal losses per cm (exclusive of transmission losses by the mirrors) which include, for example, diffraction losses, excited state absorption and scattering losses. Diffraction losses were negligible in view of the large Fresnel number associated with the resonator structure ($N \simeq 20$). The rod ends were plane parallel and carefully aligned with the plane-dielectric coated mirrors.

For a four-level material, such as Nd:YAG, when the population in the terminal level is negligible, the small-signal gain coefficient, g, is related to the population density of the upper laser level, N_u, by

$$g = \sigma N_u \qquad (4)$$

where σ is the peak stimulated emission cross section.

In pulsed or chopped CW operation, the upper level population density is related to the pump energy absorbed at threshold by

$$N_u = \frac{\eta_P E_T}{h\nu_P V} \tag{5}$$

and

$$E_T = f_B f(t_r, t, \tau)\, E_A \tag{6}$$

where η_P is the pump quantum efficiency, namely, the fractional number of Nd^{3+} ions in the $^4F_{3/2}$ state per absorbed photon, $h\nu_P$, is the energy per pump photon, V is the volume pumped, E_A is the energy absorbed by the crystal at threshold, f_B is the fractional number of Nd^{3+} ions in the appropriate laser sublevel of the $^4F_{3/2}$ state, and $f(t_r, t, \tau)$ is a correction factor to account for spontaneous decay from the upper laser level prior to threshold.

Much careful work has been directed towards the measurement of η_P. When pumping neodymium-doped crystals with flashlamps and other light sources, excitations occur predominantly to higher-lying levels than the $^4F_{3/2}$ state. The $^4F_{3/2}$ level is populated by nonradiative relaxation from these higher-lying levels. This process is so rapid that fluorescence from the higher lying levels has never been observed.[1] It is concluded that each absorbed pump photon leads to a Nd^{3+} ion in the $^4F_{3/2}$ state, and therefore, to a close approximation, $\eta_P = 1$. The same result follows for all neodyminum-doped crystals commonly encountered. These experimental results agree with theoretical predictions of very rapid nonradiative relaxation of the higher-lying levels to the $^4F_{3/2}$ level. In all subsequent equations, η_P has been taken to be unity and does not appear in the equations.

In spectroscopic determinations of σ, a quantity of crucial importance is η_F - the fluorescence quantum efficiency. This is the fractional number of Nd^{3+} ions in the $^4F_{3/2}$ level that decay by fluorescence. The $^4F_{3/2}$ state is relaxed by radiative and non-radiative processes.[3] We stress this point to avoid confusion between η_P and η_F. In the laser method for determination

of σ, a knowledge of η_F is not required.

In Nd:YAG, the laser transition originates from the upper sublevel of the $^4F_{3/2}$ state so that f_B for YAG is

$$f_B = \frac{1}{1 + \exp(h\, c\Delta\bar{\nu} / KT)} \tag{7}$$

where h is Planck's constant, c is the velocity of light, K is Boltzmann's constant, T is the Kelvin temperature and $\Delta\bar{\nu}$ is the level splitting in wavenumbers between the upper and lower sublevels of the $^4F_{3/2}$ state. For YAG, $\Delta\bar{\nu} = 88\ cm^{-1}$ so that $f_B = 0.40$.

When measurements are made using a pulsed or chopped CW excitation source, the 514.5 nm input pump pulse is monitored on a photodiode and displayed on the upper trace of a dual trace oscilloscope and the 1064 nm output is monitored on the lower trace. The scope is triggered at the start of the pump pulse (t = 0) and the 1064 nm output is monitored simultaneously with the 514.5 nm input on the oscilloscope. The area under the pump pulse up to the threshold time, t, is a direct measure of the threshold energy absorbed, E_A. This is illustrated in Figure IV-1. However, spontaneous decay from the upper laser level occurs prior to threshold and the measured threshold energy absorbed, E_A, must be corrected to account for this. If the pump pulse is approximated by a flat-topped pulse with a rise time, $t_r = 0$, the corrected threshold energy absorbed is

$$f(t, \tau)\, E_A = P_A \tau \left[1 - \exp\left(-\frac{t}{\tau}\right)\right] \tag{8}$$

where P_A is the peak power absorbed (flat portion of pump pulse), t is the time required for threshold and τ is the measured fluorescent lifetime (τ = 230 μsec for Nd:YAG).

However, our chopped, CW pulse had a linear rise time of approximately 60 μsec. The correction in this case is

$$f(t_r, t, \tau)\, E_A = P_A \tau \left\{1 - \frac{\tau}{t_r}\left[1 - \exp\left(-\frac{t_r}{\tau}\right)\right] \exp\left(\frac{t_r - t}{\tau}\right)\right\} \tag{9}$$

where t_r is the measured pump pulse rise time from zero to peak power, P_A.

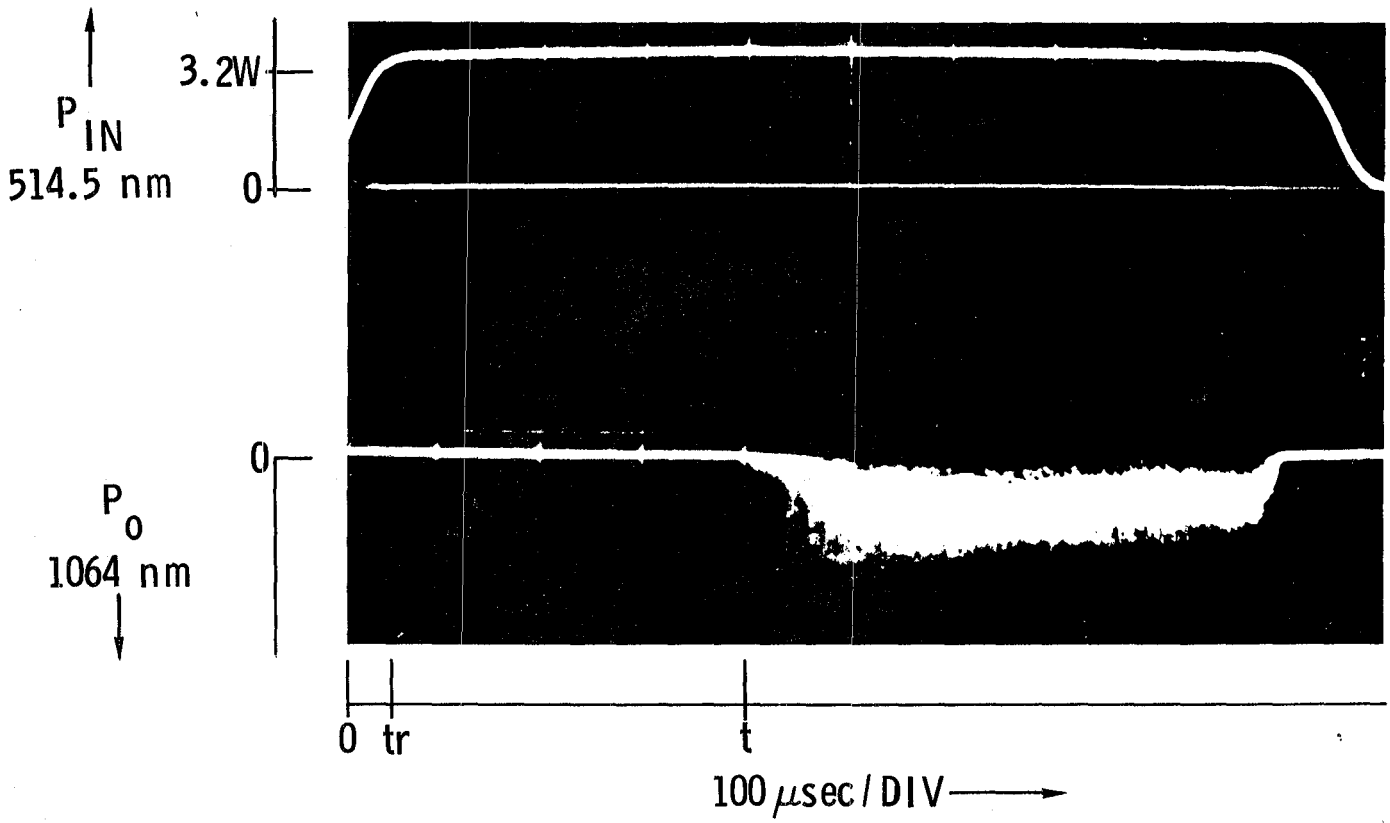

UPPER TRACE: 514.5 nm PUMP PULSE
VERT 2.5 W / DIV
HORIZ 100 μsec / DIV

LOWER TRACE: 1064 nm OUTPUT
VERT 50 mV / DIV
HORIZ 100 μsec / DIV

IV-1 Method of Obtaining Energy Absorbed at Threshold. Oscilloscope Trace of 1064 nm Output Relative to 514.5 nm Input Pulse. Threshold Energy Absorbed is Proportional to Area Under Upper Trace Up to 1064 nm Threshold Time, t.

A discussion of the volume factor, V, in Eq. (5) is given below. If a long focal length lens is used and furthermore, if the pump beam cross section has a uniform intensity distribution, the pump volume will approximate a solid cylinder of length, L, and diameter, d, and V is just

$$V = \frac{\pi d^2 L}{4} \tag{10}$$

where d is the diameter of the pump beam.

Substitituting (4), (5) and (10) into (3) and taking the natural logarithm we obtain,

$$- \ell n\, R_1 R_2 = \left(\frac{8\sigma}{\pi h \nu_P d^2}\right) E_T - 2L\Delta \tag{11}$$

We see that a plot of $- \ell n\, R_1 R_2$ vs. E_T is linear. The intercept of the line, $- 2L\Delta$, determines the losses and the slope of the line, M, will determine the cross section.

$$\sigma = M\left(\frac{\pi h \nu_P d^2}{8}\right) \tag{12}$$

C. Experimental Procedure

The experimental arrangement for measuring the threshold energy absorbed as a function of output mirror reflectivity is shown in Figure IV-2. Initial experiments were carried out with a CW pump beam but at the power levels required with the longer focal length lenses, thermal effects were encountered which manifested themselves as variations of 1064 nm threshold and output power with time. Pumping of the Nd:YAG crystal was accomplished with a chopped CW argon ion laser operating at 514.5 nm with a peak power of 3.2 Watts. The chopping frequency was 50 Hz and the period of the pulse was 1 msec. Stable operation was achieved at this chopping frequency and pulse width. The Nd:YAG crystal was 1.275 cm long with approximately 1% Nd concentration. The rod ends were parallel to within 10 arc secs, polished to a flatness of $\frac{1}{10}\lambda$, and anti-reflection coated at 1064 nm. The resonator consisted of two plane-parallel dielectric coated mirrors; one a total (100% R) reflector at 1064 nm, M1, and the other a partial reflector at 1064 nm, M2. The output mirror reflectivities used were

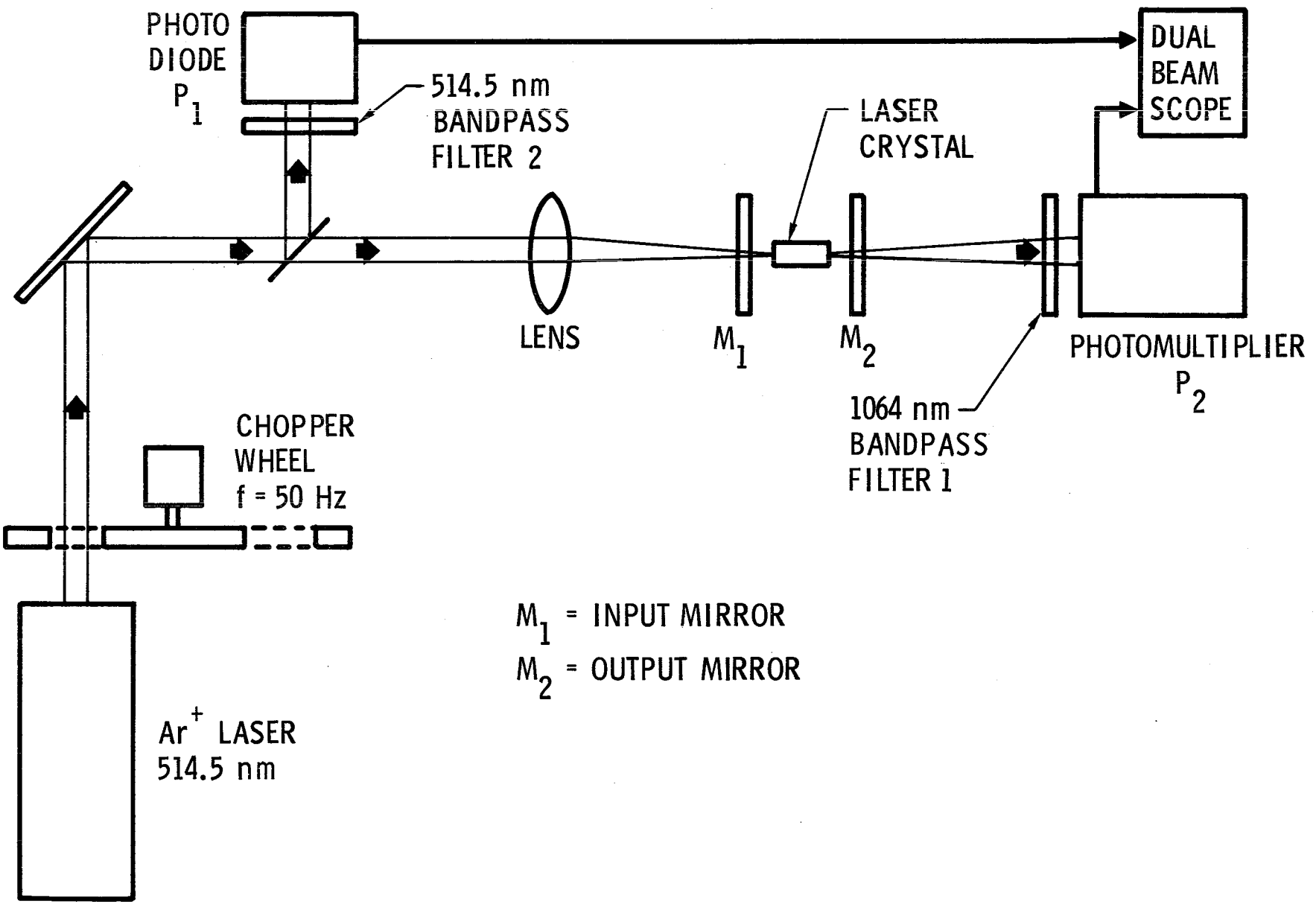

IV-2 Experimental Arrangement for Measurement of Laser Thresholds

99, 94, 91, 85, 78, and 71% at 1064 nm. The input beam was focused into the crystal with several different focal length lenses ranging from 1 meter to 2.7 meters.

The 1064 nm output was monitored with an RCA 7102 S-1 photomultiplier through a 1064 nm narrow-band filter (which was used to block the 514.5 nm pump beam) and displayed on the lower trace of a dual beam scope. The 514.5 nm pump input power was monitored on a calibrated ITT F4018 S-1 photodiode off a right angle beam splitter and displayed on the upper trace of the dual beam scope. The scope was triggered off the leading edge of this pulse. The photodiode was calibrated against a Laser Precision Corporation RK-3400 pyroelectric radiometer. For a given lens and input power, P_{IN}, the time, t, elapsed from the onset of the pump pulse to the start of the 1064 nm laser output, was measured for different output mirror reflectivities. The peak power absorbed at threshold, P_a, was obtained from

$$P_a = T_1 (1 - r_c) A k_m P_{IN} \tag{13}$$

where T_1 is the transmission of the input mirror, M_1, at 514.5 nm (approx. 91%), r_c is the crystal surface reflectivity at 514.5 nm(approx. 9%) and A is the 514.5 nm absorption factor (approx. 54%), k_m is a small correction factor (approx. 1.05) to account for multiple reflections of the 514.5 nm pump beam inside the resonator. The energy absorbed in reaching threshold, E_T, is then found by using Eq. (6) and (9).

The focused spot size can be determined in two ways: (1) by letting the focused beam impinge upon a piece of ground glass at the position of the YAG crystal and viewing this spot with a T.V. vidicon. The composite video signal is displayed on the scope and the scope time base calibrated in terms of spatial coordinates by placing an aperture of known size at the point which the beam strikes the ground glass. Or (2), by measuring the power transmitted through apertures of known diameter at the position of the YAG crystal. In the second case, the $1/e^2$ diameter, 2w, of a Gaussian pump beam can be determined from the Gaussian distribution function

$$T = \frac{P}{P_\infty} = 1 - \exp\left[-2\left(\frac{a}{w}\right)^2\right] \qquad (14)$$

where T is the aperture transmission and 2a is the aperture diameter.

For each lens, the focused spot size was measured using several apertures ranging from 200 μm to 800 μm in diameter. The average of the values obtained with each aperture was taken to be the focused $\frac{1}{e^2}$ diameter 2w.

D. Results

Plots of $(-\ell n R_1 R_2)$ as a function of energy absorbed at threshold is shown in Figure IV-3 for different focal length lenses. The losses, $-2L\Delta$ are obtained at the ordinate intercept according to Eq.(14) and are given in Table 1. The focused beam diameter for the different focal length lenses were measured according to method (2) and are also listed in Table 1. Note, the focal length of the lenses listed in the table are nominal values. In Table 1, we note that the measured spot size for the 1.49 meter focal length lens was smaller than the 1.33 meter focal length lens, not larger as one would expect.

Note that in Figure IV-3, the slopes of the lines decrease with increasing pumped volume or diameter in accordance with Eq. (12). The numerical value of these slopes, M, are given in Table 1.

In calculating the stimulated emission cross sections, σ, from the laser threshold data, the following assumptions were made: (1) the absorbed pump light is fully utilized at the Nd:YAG laser threshold and (2) the peak intensity of the pump light was necessary for laser threshold. A reasonable model for incorporating the above assumptions is to take the total energy in the Gaussian pump beam of peak intensity, I_o, and $1/e^2$ radius, w, ($E_g = \frac{\pi w^2}{2} I_o t$) and to approximate it with a rectangular pulse of the same peak intensity, I_o, and radius, r, which contains the same energy as the Gaussian beam ($E_r = \pi r^2 I_o t$). Thus $E_g = E_r$ or $\frac{\pi}{2} w^2 I_o t = \pi r^2 I_o t$. Consequently, $r^2 = w^2/2$ and the pump filament diameter, d, in Eq. (12) is taken to be, $d = \frac{2w}{\sqrt{2}}$. The stimulated emission cross section calculated on the

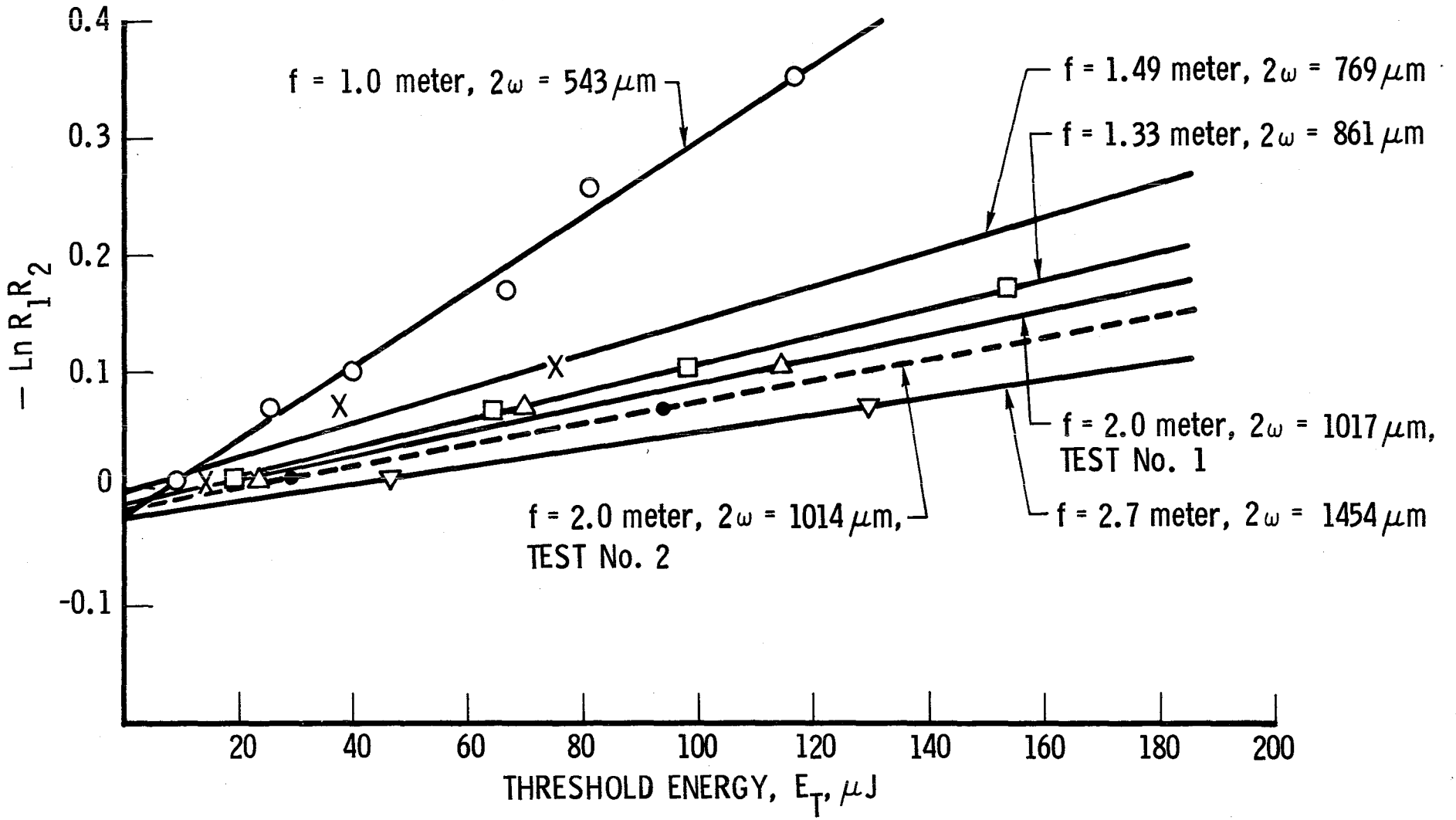

IV-3 Graphs of Energy Absorbed at Threshold vs. Output Mirror Reflectivity as a Function of Focused Pump Beam Diameter

TABLE IV-1

SUMMARY OF DATA FOR DETERMINATION OF
Nd:YAG STIMULATED EMISSION CROSS SECTION AT 1064 nm

Lens, Nominal Focal Length, f (meters)	Focused Beam $1/e^2$ Diameter, 2w (μm)	Sample Losses per cm, Δ (cm^{-1})	Slope, M $\times 10^{-3}$ (μJ^{-1})	Stimulated Emission Cross Section, σ $\times 10^{-19}$ (cm^2)
1.00	543	0.009	3.20	7.1
1.49	769	0.001	1.46	6.6
1.33	861	0.005	1.19	6.7
2.00 (Test 1)	1017	0.004	1.02	8.0
2.00 (Test 2)	1014	0.007	0.92	7.2
2.70	1454	0.009	0.72	11.5*

*Not included in average

Average 7.1×10^{-19} cm^2

basis of this model are given in Table 1 for each lens used in the experiment. The value determined from data taken with the 2.7 meter focal length lens may be attributed to an uncertainty associated with the slope of the mirror reflectivity vs. threshold energy plot for this lens, since only two data points could be obtained to define the slope of the line. All other values in Table 1 are within $\pm$12% of the mean value of 7.1×10^{-19} cm^2.

The principal difficulty in our method resides in the accurate determination of the Nd^{3+} population inversion at threshold. Measurement of the Gaussian beam profile of the pump beam does not provide an unambiguous determination since we do not know the fraction of the Gaussian beam that provides the inversion. In addition, the inversion density will also have a Gaussian profile and the determination of the appropriate average value appears difficult.

A solution to the problem posed by the pump beam Gaussian intensity profile might be an appropriate apodizer which converts the Gaussian into a rectangular (square-wave) intensity profile. In prior preliminary work, a simple apodization technique was developed utilizing photographic processes.

In order to make an apodizer, a photosensitive plate is exposed to the laser beam. The beam must be chopped to provide a low duty cycle in order to prevent overexposure. Chopper wheels and shutters cannot be used because Fresnel diffraction off the edges of the shutters and wheels produce interference lines running across the exposed area of the plate. Hence, a Pockel's cell is used instead of the chopper wheel shown in Figure IV-2. The exposure and development should provide a linear exposure curve for best results. After the apodizer has been made, the Pockel's cell is still required in order to prevent burning the apodizer at the power levels necessary to pump the crystal. Our Pockel's cell became damaged due to an internal high voltage arc during these experiments. This work will be resumed at a later date after a new Pockel's cell modulator is obtained.

A second technique is that of comparison to a sample with known cross section. In the case of Nd:glass, the $^4I_{11/2} \rightarrow {}^4F_{3/2}$ absorption has been measured directly in very long glass rods at 1.06 μm. This measurement, which does not involve any difficult spectroscopic determinations, is

considered accurate. A difficulty with Nd:glass in our application is its relatively high laser threshold. More powerful Argon ion lasers than are currently available in our laboratory would be required to pump small Nd:glass samples. Although this difficulty is not one of principle, the practical implementation could be difficult.

E. REFERENCES

1. S. Singh, R. G. Smith and L. G. Van Uitert, "Stimulated-emission cross section and fluorescent quantum efficiency of Nd^{3+} in yttrium aluminum garnet," Phys. Rev., Vol. 10, No. 6, 2566-2572, 15 Sept. 1974.

2. A. W. Tucker, M. Birnbaum, C. L. Fincher and J. W. Erler, Stimulated Emission Cross Section at 1064 nm and 1342 nm in Nd:YVO_4," J. Appl. Phys., Vol. 48, No. 12, 4907-11, December 1977.

3. G. E. Peterson and P. M. Bridenbaugh, "Study of Relaxation Proceses in Nd Using Pulsed Excitation," J. Opt. Soc. Am., 54, 644 (1964).

V. CONCLUSIONS AND RECOMMENDATIONS

The output of Nd:BeL was shown to exceed that of Nd:YAG by a factor of 2.7 at low Q-switched repetition rates (1 Hz). This result follows from the smaller stimulated emission cross section of x-axis Nd:BeL compared to that of NdYAG by the same factor. However, at high repetition rates (10 Hz) the output of Nd:BeL falls to a level of three-fifths of its low repetition rate value while under similar tests the output of Nd:YAG remains essentially constant.

A comparison of the measured values of the elasto-optic coefficients, the dn/dT values and the linear expansion coefficients for BeL and YAG failed to provide an explanation for the performance of BeL. In fact, a direct determination of the depolarization in Nd:BeL as a function of repetition rate showed essentially no change in depolarization over the range of 1-10 Hz. However, thermal lensing was observed in Nd:BeL. The focal length was measured as a function of the repetition rate and the values were used to calculate the laser beam waist diameter and the mode volume in the Nd:BeL. The decrease in mode volume at 10 Hz compared to 1 Hz was in good agreement with the decrease in output energy observed in Nd:BeL. These results imply that the output of a high repetition rate Q-switched Nd:BeL laser (high thermal loading) could be dramatically increased by utilization of a resonator design which compensates for the thermal lensing effects. It is, of course, desirable to pump with much shorter duration flashlamp pulses than used in these studies to reduce the loss of Nd^{3+} excited state population as a result of fluorescence and non-radiative decay processes. This would both reduce the thermal loading and improve the efficiency of operation.

It is proposed that the full potential of Nd:BeL at high repetition rates be experimentally demonstrated by utilization of appropriate resonator designs. The resonator modifications could consist of grinding compensating lenses on the rod ends. Compensating optical mirrors or lenses within the cavity can also be considered. In addition, optimization of the cavity length and the rod position within the cavity offer additional parameters for optimizing the laser output. This demonstration would provide the applications group with a laser which could outperform Nd:YAG in a variety of missions.

End of Document